PhD-FSTM-2023-088.
The Faculty of Science, Technology and Medicine

DISSERTATION

Defence held on 14/08/2023 in Luxembourg

to obtain the degree of

DOCTEUR DE L’UNIVERSITÉ DU LUXEMBOURG

EN *Physique*

by

Ricardo Arturo ROJAS AEDO

Born on 19 March 1992 in Angol, (Chile)

EFFECTS OF CHARGE INJECTION ON ULTRAFAST SEMICONDUCTOR DYNAMICS

Dissertation defence committee

Dr Daniele Brida, dissertation supervisor
Professor, Université du Luxembourg

Dr Mael Guennou, Chairman
Professor, Université du Luxembourg

Dr Nicolò Maccaferri
Professor, Umeå universitet

Dr Cristian Manzoni
CNR Resercher, Politecnico di Milano

Dr Denis Seletskiy
Professor, Polytechnique Montreal

"At the bottom is the treasure: the universe like a talisman
In the end, the talisman and the attachment of the body will be broken.
You will find the treasure when the talisman disappears.
When he disappears, the soul will appear
Then your soul will be another talisman
For the unseen another body is your soul. "

Farid al Din Attar

UNIVERSITÉ DU LUXEMBOURG

Abstract

Faculty of Science, Technology and Medicine (FSTM)
Department of Physics and Materials Science (DPhyMS)

Doctor of Philosophy

Effects of charge injection on ultrafast semiconductor dynamics

by Ricardo ROJAS-AEDO

Charge injection into a junction of a semiconductor with another material is a resource widely used in electronics, but little explored for applications in optics despite the great potential it offers. Ultrafast spectroscopy techniques provide useful information to understand the nature of a phenomenon in materials, and thus their potential applicability in new technologies. In this work, two ultrafast spectroscopy experimental setups are proposed to study, firstly, the effect of charge injection on the formation of collective excitations in matter and, secondly, to understand how charge injection affects dynamical parameters such as electron mobility. In the first setup, which consists of a pump-push-probe scheme inducing an independent charge injection and excitation density in a medium, it is concluded that in a WS_2(bulk)-Au junction, charge injection affects the exciton formation dynamics as a function of the ratio between the injected and the excited charge density. In the second experiment, two complementary measurements via Pump-Probe experiments are proposed: The first one measuring for transient conductivity, via a probe in the few THz range, and the second one for transient white light reflection, in order to draw solid conclusions on the effect of the extracted charges on the electronic dynamics in junctions of a CIGS (photovoltaic cells)-buffer layers.

Acknowledgements

It is difficult for me to separate my stay in Luxembourg with my PhD. It is difficult for me to say thank you without feeling like a goodbye. Chronologically: I thank Daniele for giving me the opportunity to work in his lab. I would certainly have liked to have talked more with him, but I hope that this will be possible in the following years, in collaborations or in conferences. I thank Nicolo for all the motivation and support he gave us as a postdoc and then as a visiting researcher. I thank Pirmin for his conversations, although not very common, very entertaining. I thank Kilian both professionally and personally: many hours working and discussing physics, two papers published together, many deep conversations we had and for which I consider him as a younger brother. I am grateful to Thomas with whom I feel I share in a very pleasant way almost at the end of my PhD, and with whom I really feel a great professional and personal respect. I thank Andrea who between games I felt like a cousin, someone to really trust and share affection with. I thank Markus, who always came smiling to chat with a joke. I thank Jonas who always tried to bring the group together and transmit good energy. I thank Alba for all the affection she has given to each person in the group and who helped me a lot to feel more comfortable and confident in the group. I thank Tlek for his sympathy and companionship during all the years he worked with us. I thank Sreyash who was an important part of making me realise personal weaknesses I had. I thank Aline with whom we worked together until a moment where she showed independence, and where she demonstrated her great scientific capabilities, especially in the generation of THz radiation in the final chapter of this thesis. I thank Majdi, with whom I have not shared much, but with whom I think he is very noble. I thank Neshat who with great affection helped me to improve my weaknesses and who gave me a basis to build on at the time of my defence. Also I thank Birger for all the motivation and discussions in physics we have had over the years.

In Luxembourg I made great friendships beyond the professional. I thank Sharadhi who helped me a lot in the process of recognising my weaknesses. I thank Katrin in whom I always saw a person I could trust. I thank Najiya, with whom I feel I have a very close connection on a spiritual level. I thank my Chilean and theatre friends who for so many years made me feel part of a community. I thank my friends in Chile with whom I constantly talk, Sergio, Virginia, Stefano, David, Ale Gallyas and Ale Polidori. I thank Juan Pablo who has guided me on my spiritual path for so many years. In particular I must also thank three friends who gave me shelter and light in the darkest moment of my doctorate: I thank Deniz who in a very short time I have felt her as a person capable of noticing the ups and downs of my emotions. I thank Fran who has given me so much love, affection and daily conversations. I thank Divya with whom in the last two years I have developed one of the most beautiful friendships I have ever had in my life, in constant conversations and sincere affection.

I thank my family, my grandmothers, who always want to talk to me. I love my mother deeply, and I feel that she has been one of the greatest supporters of my doctorate. I love my dad, my best friend, who has given me such great gifts and learning and who, as he could not be in two places at the same time, decided to be everywhere.

Best wishes to all of you.

“The bird fights its way out of the egg. The egg is the world. Who would be born must first destroy a world. The bird flies to God. That God’s name is Abraxas.” Hermann Hesse.

Luxembourg was the temple of my solitude, I embraced my shadow, I developed as a person, my system has guided me, and my heart thanks your forests. . .

Contents

List of Figures

List of Tables

List of Abbreviations

Ti:Sa	**Ti**tanium **Sa**pphire laser
PP	**P**ump **P**robe
GVD	**G**roup **V**elocity **D**ispersion
TEM	**T**ransverse **E**lectromagnetic **M**odes
YAG	**Y**ttrium **A**luminium **G**arnet
SC	**S**uper**C**ontinuum
BBO	β-**B**arium **BO**rate
OPA	**O**ptical **P**arametric **A**mplifier
VIS	**VIS**IBLE
SHG	**S**econd **H**armonic **G**eneration
SFG	**S**um **F**requency **G**eneration
DFG	**D**ifference **F**requency **G**eneration
HR	ultra-**H**igh **R**eflectivity mirrors
NIR	**N**ear **I**nfra**R**ed
EOS	**E**lectro-**O**ptic **S**ampling
CW	**C**ontinuous **W**ave
TMD	**T**ransition **M**etal **D**ichalcogenides
PPP	**P**ump-**P**ush-**P**robe
SBH	**S**chottky-**B**arrier **H**igh
CIGS	**C**opper **I**ndium **G**allium **S**elenide
MOVPE	**M**etal**O**rganic **V**apour-**P**hase **E**pitaxy
FWHM	**F**ull **W**idth at **H**alf **M**aximum
ASD	**A**mplitud **S**pectral **D**ensity
HWP	**H**alf **W**ave **P**late
QWP	**Q**uarter **W**ave **P**late

PBS	**P**olarizing **B**eam **S**plitter
BS	**B**eam **S**plitter
PV	**P**hoto**V**oltaics
RMS	**R**oot **M**ean **S**quare
GaSe	**Ga**llium (II) **Se**lenide
SEDP	**S**pectral **E**nergy **D**istribution per **P**ulse

Dedicada a mi mamá. En memoria de mi papá…

Chapter 1

Introduction

One of the pillars on which the technological revolution developed in the last hundred years, such as electronics, is based is the understanding and subsequent engineering of semiconductor-based devices. A particularly relevant group of semiconductor-based devices are those involving semiconductor junctions with other materials, for example transistors and diodes, which are indispensable ingredients for the development of computers. Today, semiconductor junctions with other materials continue to lead technological development; the most efficient solar cells in general are based on junction systems between semiconductors, while many platforms for quantum information protocols contemplate a junction of semiconductors with other materials. Whether for electronics, computing or new applications, semiconductor junction exploit as a main ingredient the exchange of electrons between materials, or in other words, the injection of charges from or into the semiconductor. Physical phenomena that take place in a semiconductor can be affected by charge injection, so understanding the nature of these effects is one of the keys to expanding the field of applications of this resource in semiconductors. One of the most revealing measurements of the physics of material phenomena is the femtosecond time evolution of the interaction between light and matter, which is of considerable value in understanding the effects of injected charges in semiconductor physics. This thesis presents measurements and analysis of the effects of charge injection on the ultrafast dynamics in photoexcited semiconductors. The second chapter explains how to measure effects on short time scales, and presents the experimental setups built during my PhD that serve as tools for this purpose. The third chapter explains the physics of junctions formed by semiconductors and other materials. The fourth and fifth chapters analyse the effect of injection on carrier dynamics in a photoexcited semiconductor at times of a few picoseconds and hundreds of picoseconds, respectively. This separation into different chapters is based on the different nature of the interactions in a photoexcited semiconductor; after short times, dominated by Coulombic interactions between particles, and for long times, dominated by interactions between quasiparticles and collective excitations, which are forms of collective behaviour of particles in the material with a fermionic or bosonic statistics respectively. For short times, the effect of charge injection on the dynamics of collective excitation formation in materials of high interest in quantum optics, such as TMDs, is analysed, while for long times, a robust way to extract dynamical variables is discussed, for example to analyse the dynamics of a photoexcited solar cell with buffer layers. Finally, general conclusions are drawn in the sixth chapter.

Chapter 2

Optical toolbox for studying ultrafast phenomena in condensed matters

The way a medium interacts with an electromagnetic wave of a particular wavelength reveals absorption or emission lines that are closely related to the structure and interactions between particles in a material. Examples that produce different absorption or emission lines are the excitation and decay of electrons, the vibrational modes of a material, the average time between collisions of free electrons in a medium, or the interaction between particles and quasiparticles of a material. After excitation of a medium, the absorption or emission rate of different wavelengths can be affected, at least until the system relaxes back to its pre-excitation state. This relaxation of the medium means that the absorption and emission rates will change as a function of time, from the time of excitation until the medium returns to its original state. Since optical transitions are affected by, for example, interactions between particles and quasiparticles in the material, the evolution of the absorption and emission rates as a function of wavelength will provide information about these interaction mechanisms. The knowledge of the interaction mechanisms in a material allows, as a next step, the use of these mechanisms in technological applications, e.g. by blocking or promoting the occurrence of effects in a medium.

The study of absorption or emission at different times and at different wavelengths requires electromagnetic radiation pulses that interact with a medium at a precise instant and are ideally spectrally broad in order to study a wide variety of possible transitions. This chapter begins by discussing in detail a technique called pump probe, which uses pulses to characterise optical transitions in time. In order to have spectrally broad pulses, in a second part the generation of pulsed white light will be discussed and an original scheme for the generation of stable pulsed white light in liquid media will be presented (section 2.2.2), which is in the process of being published. Finally, since the excitation wavelength has an impact on the interaction mechanisms of the medium, optical parametric amplification will be introduced, as a technique that allows to obtain intense pulses that can be tuned in different spectral ranges and different temporal durations. Based on this technique, different optical setups have been constructed to obtain pulses in the visible (section 2.3.2), near-infrared (section 2.3.3 and 2.3.4) and mid-infrared with high peak fields (section 2.3.6). In the context of the study of dynamic processes in semiconductors, the first two spectral regions chosen, visible and near-infrared, allow in general the interband excitation of electrons,while the latter due to its high peak field allows access to effects in non-perturbative regimes such as the generation of high harmonics in out-of-resonance conditions between the generated frequencies and transitions of the medium .

All experimental setups, unless explicitly stated otherwise, were based on a Titanium Sapphire (Ti:Sa) laser with pulses centred at 800 nm, a duration of 150 fs, an energy per pulse of 1 mJ and a repetition rate of 1 kHz.

2.1 Fundamentals of Pump-Probe experiments

A material can be considered as a quantum system composed of multiple energy levels for electronic states. A quantum system in equilibrium will have the electronic populations of its quantum levels constant over time or with periodic time oscillations. This behaviour can be studied by interacting the quantum system with infinitely long electromagnetic fields. The instantaneous interaction of ultrafast pulses, on the other hand, allows the study of quantum systems out of equilibrium, or in other words, with a non-periodic evolution of the populations of quantum states. The electronic dynamics from an excited non-equilibrium state to an equilibrium state can be studied using a two-pulse experimental procedure called Pump-Probe. The first pulse, called Pump, has sufficient energy to excite the quantum state of a material and thus marks the beginning of out-of-equilibrium electron dynamics. And the second pulse, called probe, allows to know the dipole moment of the system at a time τ after the excitation.

Schematically, and for simplicity, a material can be modelled as a two-level system, where at equilibrium the entire electron population is in the $|0\rangle$ state. With the arrival of the pump pulse, a part of the electron population is promoted to the excited level $|1\rangle$, in a time that will be defined as time $\tau = 0$. From the moment that the excited state has a non-zero electron population out of equilibrium, electrons from the excited state will undergo a spontaneous decay, causing the electron populations in the $|0\rangle$ and $|1\rangle$ state to change as a function of time. Thus, for a probe pulse interacting with the system at time $\tau = t$ after the pump, there will be a change in its photon number mediated by absorption and stimulated emission of photons in the transition from the $|1\rangle$ to the $|0\rangle$, which are dependent on the populations at time t. This change in the number of photons for a probe pulse at Pump time t at position z is directly proportional to the change in pulse intensity $I_p(z,t)$, and can be described mathematically by dividing the system into several steps of length dz given an equation such us

$$\left[I_p(z+dz,t) - I_p(z,t)\right] \propto \left[n_1(z,t)B_{10} - n_0(z,t)B_{01}\right] I_p(z,t)dz \tag{2.1}$$

with $n_1(z,t)$ and $n_0(z,t)$ being the populations in the position z at time t of the $|1\rangle$ and $|0\rangle$ states respectively, and B_{01} and B_{10} the Einstein coefficients for the absorption and for the stimulated emission.

The dependence of the time delay between pump and probe in $I_p(z,t)$ connects the change of the probe intensity as a function of t with the time evolution of the populations of the quantum system under study. From a practical point of view, for this type of analysis to show an appreciable change in probe intensity, it is necessary that the population n_1 is not negligible compared to n_0, which implies the need for a high pump pulse intensity. Equivalently, a low intensity of the probe pulse is also necessary to avoid self-induced effects due to changes in the populations stimulated by one part of the pulse and its effects on other parts of the pulse. In general, for an experimental measurement, the probe must have an interaction with the quantum system that is at least one order of magnitude lower than the pump pulse.

Experimentally, other considerations must also be taken into account. Since the excitation is induced by the pump pulse, there must be a spatial overlap between the pump beam and the probe beam in the region of the material under investigation. Furthermore, due to the normally Gaussian spatial mode of the beam intensities, the pump will have a different effect on different areas of the material, but only a portion of the area interacting with a sufficient photon density from the pump will be able to induce a change in the intensity of the probe. For this reason, the area covered by the pump must be much larger than the area covered by the probe, making the effect of the pump material interaction on the probe homogeneous. To achieve a controlled delay between the pump and the probe, the pump is aligned in a retro-type configuration in an electronic translation stage, as shown in 2.1, allowing the quantum state evolution of a material to be studied with a resolution of a few femtoseconds. Since the difference in intensity in the probe caused by the change in the populations of the quantum states of the material due to the pump effect is generally two orders of magnitude smaller than the total intensity of the probe, it is necessary to separate this signal from the noise. To do this, a chopper is commonly used in the pump line, as shown in 2.1, which generates a modulation of the pump pulse that will acquire a different repetition rate than the probe repetition. This modulation in pump repetition rate implies that the probe periodically interacts with a previously excited material and at other times with the non-previously excited material. This periodic interaction with excited and unexcited material involves a modulation in the probe intensity, and the difference between these two cases can be directly measured by using a photodetector connected to a lock in amplifier, see Fig.2.1. The use of a lock in amplifier under these conditions allows the signal to be cleaned of noise sources with repetition rates different from the modulation, allowing cleaner measurements with less uncertainty.

The maximum time resolution of a pump probe scheme is a function of the

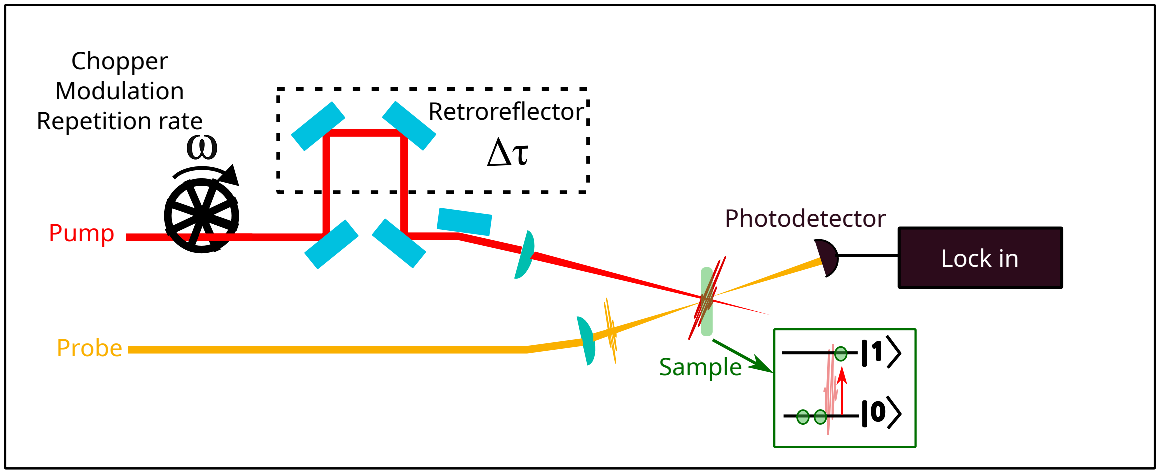

FIGURE 2.1: Pump-Probe scheme: A pump with a repetition frequency modulated by a chopper and with a path length regulated by a retroreflector excites a sample, which is then measured by a probe and a photodetector connected to a Lock in.

time length of the pump pulse and the spectrum and spectral phase of the probe pulse. In particular, if the probe pulse has a linear spectral phase and is in resonance with the system, the time resolution of the scheme is given by the time convolution between the pump pulse and the probe pulse. If the probe pulse has a non-linear spectral phase, photons of different energies have a distribution that differs with the temporal profile of the pulse, so that the distribution of photons that can resonate with the studied transition is generally shorter than the total temporal duration of the pulse. Given this temporal distribution of photons, the temporal resolution of the pump-probe scheme studying a particular transition is given by the temporal convolution of the pump pulse with the temporal distribution of photons resonating with the transition under study [Pol+10].

In general, the two-level model presented to explain the pump-probe experiment has depended on the number of pump and probe photons to generate electron transitions between quantum states. However, the present work presents some variations that depend on the electric field and not on the number of photons, so that they have a slightly different analysis, but keep the spirit of the pump-probe scheme.

2.1.1 Pump-Probe in solid-state systems

Although the two-level system presented above serves as a first approximation to a pump probe scheme, it does not take into account the interactions between particles and hence the physical meaning of the decay coefficients and time constants extracted in a pump probe experiment. In this section a more precise description of a Pump-Probe scheme in semiconductor systems will be presented in a formal way. The mathematical formalism that will be introduced, although it will not be used for a modelling of our experiments, will serve as a basis for a precise description of collective behaviours such as excitons in the following chapters, as well as explicitly showing some observables whose dynamics can be measured in a pump probe experiment. For a semiconductor, the two-level model can be generalised by interpreting them as the valence band level and the conduction band level. The energy of a semiconductor in this approximation is described by the eigenvalues of the Hamiltonian[KK06].

$$\hat{H}_{sol} = \left[\sum_{\lambda,\mathbf{k}} \epsilon^{\lambda}_{\mathbf{k}} \hat{a}^{\dagger}_{\mathbf{k},\lambda} \hat{a}_{\mathbf{k},\lambda} + \hbar \sum_{\mathbf{p}} \Omega_{\mathbf{p}} \left(\hat{D}^{\dagger}_{\mathbf{p}} \hat{D}_{\mathbf{p}} \right) \right] + \left[\sum_{\lambda,\mathbf{k},\mathbf{p}} G^{\lambda}_{\mathbf{p}} \left(D_{\mathbf{p}} + D^{\dagger}_{\mathbf{-p}} \right) \hat{a}^{\dagger}_{\mathbf{k},\lambda} \hat{a}_{\mathbf{k}\text{-}\mathbf{p},\lambda} \right]$$

$$+ \left[\frac{1}{2} \sum_{\lambda,\mathbf{k}} \sum_{\lambda',\mathbf{k}'} \sum_{\mathbf{q}\neq 0} \frac{ke^2}{\mathbf{q}^2} \hat{a}^{\dagger}_{\mathbf{k},\lambda} \hat{a}^{\dagger}_{\mathbf{k}',\lambda'} \hat{a}_{\mathbf{k}'+\mathbf{q},\lambda'} \hat{a}_{\mathbf{k}'-\mathbf{q},\lambda'} \right], \tag{2.2}$$

where $\epsilon^{\lambda}_{\mathbf{k}}$ is the energy of a free electron in the band λ and with a momentum $\mathbf{k}$, $\hat{a}_{\mathbf{k},\lambda}$ and $\hat{D}$ are electron and phonon destruction operators respectively in the specified band and momentum, the same operators with the superscript $\dagger$ are creation operators, $G^{\lambda}_{\mathbf{p}}$ and k are proportionality constants.Naturally, the operator $\hat{a}_{\mathbf{k},\lambda}$ ($\hat{a}^{\dagger}_{\mathbf{k},\lambda}$), besides being associated with the destruction of electrons, can also be associated with the creation (destruction) of holes if λ corresponds to the valence band. The λ and λ' notation distinguishes particles in different bands.The first term enclosed in square brackets refers to quantities associated with the free propagation of particles or quasiparticles. The second term refers to the interaction of the phononic and electronic field, and the last term is associated with the Coulomb-like interaction between electrons. To describe a system where a photonic field is interacting with a solid, two additional terms must be added to the already known Hamiltonian of the solid $(\hat{H}_{sol})$, the free photon propagation $(\hat{H}_{phot})$ and an interaction term $(\hat{H}_{sol-phot})$. The free fields do not play any role in the analysis, being relevant only the interaction hamiltonian given by [KK06]

$$\begin{aligned} &\hat{H}_{sol-phot} = \\ &\sum_{\mathbf{k},\lambda}\left[-\sum_{\mathbf{q}}\frac{Q\hbar\mathbf{k}}{m_\lambda}\cdot e_{\mathbf{q}}\hat{A}_{\mathbf{q}}\hat{a}^\dagger_{\mathbf{k}+\mathbf{q}/2,\lambda}\hat{a}_{\mathbf{k}-\mathbf{q}/2,\lambda}+\sum_{\mathbf{q},\mathbf{q}'}\frac{Q^2}{2m_0}\hat{A}_{\mathbf{q}}\hat{A}_{\mathbf{q}'}(e_{\mathbf{q}}\cdot e'_{\mathbf{q}})\hat{a}^\dagger_{\mathbf{k}-\mathbf{k}',\lambda}\hat{a}_{\mathbf{k}-\mathbf{q},\lambda}\right] \\ &-\sum_{\mathbf{q},\mathbf{k}}\sum_{\lambda\neq\lambda'}\frac{Q\mathbf{p}_{\lambda,\lambda'}}{m_0}\cdot\hat{A}_{\mathbf{q}}\hat{a}^\dagger_{\mathbf{k},\lambda}\hat{a}_{\mathbf{k}-\mathbf{q},\lambda'}, \end{aligned} \tag{2.3}$$

with $\hat{A}$ the operator for the potential vector of the photon field, $e_{\mathbf{q}}$ a normal vector in the direction of polarisation of the electromagnetic field, m_λ the effective mass of the λ band, m_0 is mass of the particle and $\mathbf{p}_{\lambda,\lambda'}$ the momentum operator: There are two contributions to be distinguished here. The terms within the square brackets are intraband processes that change the momentum of an electron, known as the ponderomotive energy. The term outside the brackets is an interband process associated with the absorption and emission of photons and the consequent transition of electrons from the valence band to the conduction band and vice versa. Other components of the Hamiltonian, such as the phonon-phonon interaction or the phonon-photon interaction for optical phonons, can be added to extend the model, but for the purposes of this introduction such terms do not add anything conceptually interesting to the discussion.

A particularly interesting operator to describe the system is

$$\hat{P}^{\lambda,\lambda'}_{\mathbf{k}} = \hat{a}^\dagger_{\mathbf{k},\lambda}\hat{a}_{\mathbf{k},\lambda'}. \tag{2.4}$$

In the operator $P^{\lambda,\lambda'}_{\mathbf{k}}$, when λ and λ' coincide, the probability of charge occupation at the associated energy level can be extracted. If the indices are different, this operator takes the place of the polarisation of the irradiated solid, and it can be shown by the evolution of the photon field that [KK06]

$$\left[\nabla^2 - \frac{n^2}{c^2}\frac{\partial^2}{\partial t^2}\right]\hat{A}_0(z,t) = -\mu_0 g(z)\frac{\partial}{\partial t}\left(\hat{P}_0^{v,c} + \hat{P}_0^{c,v}\right). \tag{2.5}$$

Recognising this operator as the polarisation of the medium allows us to extract the susceptibility . In particular, the linear susceptibility is related to the polarisation by

$$\chi^{(1)}(\omega) = \frac{P(\omega)}{\epsilon_0 E(\omega)}, \tag{2.6}$$

and from which the linear optical qualities can be extracted using the

$$n(\omega) = \sqrt{1 + 4\pi\chi^{(1)}(\omega)} \tag{2.7}$$

where the real part is related to the refractive index and the imaginary part to the absorption. Considering the set of interactions described by the Hamiltonian of the solid system interacting with photons, it is possible to extract the time evolution of $P_{\mathbf{k}}^{\lambda,\lambda\prime}$ composed of operators already explicitly present in the total Hamiltonian. In general, the study of the evolution of the Hamiltonian 2.2 shows for early times a greater relevance for single particle processes such as carrier carrier scattering, while for longer times the collective excitation processes involving more than one particle such as phonons dominate the dynamics of the process [KK06].

2.2 White light generation

To study the dynamics of a particular transition in a material, it is necessary to have a pulsed light source with photons of resonant energy with the transition under analysis. In this context, the availability of a technique that generates a continuum of frequencies is key to the study of condensed matter dynamics. A particularly interesting way to generate frequency continuums is the use of non-linear processes such as the generation of white light resulting from the interaction of an intense pulse with a material. In this section and in the two subsections that follow, dedicated to white light generation, we will show the progress made in stabilising white light signals in liquid media, which is an original work in this field. In particular, we will first give a summary description of the theory of the white light generation process, in order to motivate the various means that can be used to optimise this process. This line of exposition allows us to present in a clear way the methods used to generate stable white light in liquids.

The white light generation is a process mediated by diffraction, group velocity dispersion (GVD), self-focusing, self-phase modulation, multiphoton absorption and finally ionization. Ionization plays a fundamental role in white light generation, as it promotes the formation of a plasma filament in the material, which induces a region of high electric field density beyond what would be allowed by Gaussian optics. This high electric field density means higher efficiency in the nonlinear response and therefore in the generation of broad spectra.

The interaction of an electromagnetic wave with a medium will induce a dipole response or polarization in the material, consisting of the movement of the charges of the medium with the applied electromagnetic field. Strictly speaking, the movement of charges induced by the electromagnetic wave will be mediated by the symmetry of the medium, so that the polarization must be proportional to a tensor that reflects these symmetries. In general, if the electromagnetic wave is weak, the response of the medium will be linear with the field, so the polarization will also be linear. If the electromagnetic wave is larger, the polarization will have nonlinear components with the field, inducing a response that can be expressed as a Taylor type polynomial,

$$P(t) = \chi^{(1)} E(t) + \chi^{(2)} E^2(t) + \chi^{(3)} E^3(t).... \tag{2.8}$$

where the terms $\chi^{(n)}$ are tensors of the electromagnetic susceptibility of order n. A particular case that shows how the susceptibility tensors respond to the symmetry of the medium is assuming a centrosymmetric medium, which has no contributions from even-order susceptibility tensors.

When a high-intensity pulse propagates in a centrosymmetric medium, the third-order nolinear component of the dielectric polarisation density becomes relevant,

$$P(t) = \chi^{(1)}E(t) + \chi^{(3)}E^3(t) \tag{2.9}$$

The non-linear dielectric polarisation terms implies an intensity induced change in refractive index such that

$$n = n_0 + n_2 I \tag{2.10}$$

where

$$n_2 = \frac{3\chi^{(3)}}{4\epsilon_0 c n_0^2} \tag{2.11}$$

which is a positive quantity, in the transparent range in most dielectric media.

Due to the Gaussian distribution of the intensity profile of the light beams, the change in refractive index will decrease from the centre of the beam to the edges in a lens-like effect called Kerr lens, which induces self-focusing. This self-focusing effect changes as the pulse propagates through the material, as each step creates a new intensity profile with a higher photon density. This non-linear focusing effect of the propagating wave competes with diffraction, which is a natural limit to focusing, so that the beam is focused to the point where the defocusing tendency produced by diffraction is higher than the focusing due to self-focusing. This dynamic, in a propagation model that considers only self-focusing and diffraction, assumes three regimes in the spatial profile of the beam in the direction of propagation as a function of the power of the propagating pulse. One regime is the simple focusing and defocusing of the beam, another regime is a multiple cyclic focusing and defocusing of the beam and finally an intermediate regime implies a balance between diffraction and self-focusing, generating a spatial soliton or Townes mode. The power of the pulse that achieves the balance is called the critical power and is defined as

$$P_{cr} = \frac{3.72\lambda^2}{8\pi n_0 n_2}. \tag{2.12}$$

With a beam power above P_{cr}, the beam radius could theoretically become infinitely small due to self-focusing. However, due to the resulting high photon density and multiphoton absorption, it is possible to promote ionisation of the material, which implies a large loss of beam energy, limiting the effect of self-focusing. Due to the higher photon density available in the centre of the beam and lower at the edges, ionisation will affect the central region of the beam. The presence of a density of free electrons $(\rho(z,t))$ will in turn cause a change in the permittivity of the medium and consequently a change in the refractive index, given by

$$n = n_0 - \frac{\rho(z,t)}{2n_0\rho_c} \tag{2.13}$$

where ρ_c is the critical plasma density at which the plasma becomes opaque to electromagnetic radiation of frequency ω_0. The additional component to the refractive index of the material due to the electrons has a sign opposite to that of n_2 in 2.10, generating a competition between a focusing and a defocusing effect of the beam, and which can lead to a cyclic refocusing of the plasma channel, called plasma refocusing. The efficiency of the self-focusing will thus be a function of the order of the multiphoton absorption, defined as

$$K = (U_g/\hbar\omega_0) + 1, \tag{2.14}$$

where U_g is the band gap of the material and $\hbar\omega_0$ is the photon energy. Photons with energy much lower than the band gap will have a smaller beam radius than more energetic photons. The limit of this correlation is found when the energy of the photons is higher than half the energy of the band gap $(K < 3)$, which will not have self-focusing due to two-photon absorption.

The non-linear change in refractive index induces, in addition to self-focusing in the transverse spatial profile, a modulation of the temporal phase dependent on the pulse intensity, an effect called self-phase modulation. Thus, the instantaneous frequency $(\omega(t))$, defined as the time derivative of the temporal phase, will have an additional component to the optical oscillation frequency (ω_0),

$$\omega(t) = \omega_0 - \left(\frac{\omega_0 n_2}{c}\right) \frac{d}{dt} \left(\int_0^L I(z,t) dz\right), \tag{2.15}$$

where $I(z,t)$ is the time profile of the pulse at position z of propagation and L is the length of the non-linear medium. This modulation of the instantaneous frequency implies the generation of new optical frequencies and thus changes in the time profile of the pulse, so that at each step a new temporal profile must be considered due to the non-linear interaction of the previous step, in addition to the effect of the chromatic dispersion of the material.

If the power is sufficient for the ionisation of the material, the excitation rate of electrons in the valence band to the conduction band must be considered as another source of time-dependent modulation of the refractive index. The time dependence of the free electron density is given by the equation

$$\frac{\partial \rho(z,t)}{\partial t} = \frac{\beta_k}{K\hbar\omega_0} I(z,t)^K. \tag{2.16}$$

with β_k the multiphoton absorption coefficient.

This temporal modulation implies an additional component in the instantaneous frequency which, consistent with the analysis of self-focusing, also has an opposite effect to the self-phase modulation. It has been postulated in recent work [Liu+02] that the trade-off between these two sources of modulation limits the generation of broader spectra even at higher initial propagating pulse strengths, although the overall spectral intensity may still increase. In fact, even with these counteracting effects, the presence of the plasma channel strongly increases the spectral width of the signal, given the high photon density and the consequent high probability of non-linear mixing. For this reason, the generation of new wavelengths by filamentation is called white light generation.

Experiments show that the shortest and longest wavelengths that can be obtained by white light generation depend in different ways on the properties of the medium and the focusing geometry or the maximum power of the electric field of the pulse in the material [BBR09]. Shorter wavelengths have a fundamental limit that depends primarily on the bandgap energy of the material, whereas shorter wavelengths are much more dependent on the power and focusing geometry in the medium. This different dependence on physical parameters can be understood by noting that when a pulse, such as a Gaussian pulse, interacts with a region of material, an increase in intensity will begin as the pulse propagates, reach a maximum point, and then begin a decrease until the pulse has completely crossed the region. This initial increase in intensity in time gives rise to a phase modulation in the equation 2.15, which contributes to the generation of long wavelengths and is the only contribution to the generation of new wavelengths until the photon density is sufficient to start the ionisation of the medium and consequent generation of plasma. The plasma generated in the medium once the critical photon density is reached, which is a function of the bandgap of the material, imposes an equilibrium condition for signal maximisation and will primarily affect the generation of short wavelengths.

While it is generally desirable to increase the pulse power to the range that promotes filamentation or beyond, there is an upper limit to the pulse power due to self-induced geometric effects in the plasma channel that interfere with the generation of broad, intense and coherent white light spectra. One effect of excess power is due to focusing and defocusing of the plasma channel in the direction of propagation [DC19]. This effect, known as plasma refocusing, creates discrete regions with different refractive indices in the direction of propagation, resulting in a double or multiple pulse in the temporal structure of the white light pulse, which is manifested spectrally by the appearance of fringes. These temporal structures are generally undesirable for ultrafast spectroscopy experiments, as these new pulses in the time profile produce multiple signals with different times between pump and probe. These multiple pump and probe signals add spurious signals to the desired signal, which can lead to misinterpretation of results. These temporal structures are generally undesirable for ultrafast spectroscopy experiments, as these new pulses in the time profile produce multiple signals with different times between pump and probe beyond the desired signal, and can lead to misinterpretation of results. Another effect is the creation of zones with different refractive indices in the transverse profile of the wave due to diffraction, each of which is capable of generating an independent plasma filament in an effect called multi-filamentation [DC19]. The total mixing of white light from different regions produces incoherent and only partially polarised light, which can appear much broader in spectrum than the filamentation allows. Due to the incoherence of this white light source, the field does not have a short temporal structure, so this regime should generally be avoided. This effect can also be produced at lower intensities by a spatial mode that is very different from a TEM00, with multiple spatial structures and several separate zones of high intensity.

The defocusing and refocusing of the plasma channel in a material is a consequence of the loss of energy density due to ionisation of the material at the centre and the subsequent flow of energy from adjacent regions towards the centre of the beam. If the loss and radial flow of electromagnetic energy is compensated for, long plasma filaments can be obtained, inducing high non-linear responses. This condition requires an energy reservoir along the beam propagation to supply energy to the field in the region where filamentation occurs. A reservoir with these characteristics can be achieved by propagating a beam with a Bessel [SN10] or Airy [Pol+09] spatial mode in a material, where concentric lobes inject energy into the central lobe that induces the plasma. Bessel-like spatial modes can be achieved by transmitting the beam through an axicon lens and Ayri-like modes can be achieved by diffraction in a very tight iris. Although a Bessel mode is best for these purposes, similar effects can be achieved even with distributions with wider lateral regions, such as the Lorentzian [SN10]. This energy compensation effect in the central region of the beam not only works for ionisation energy loss, but scattering losses in defects can also be corrected in the same way, resulting in more robust plasma channels.

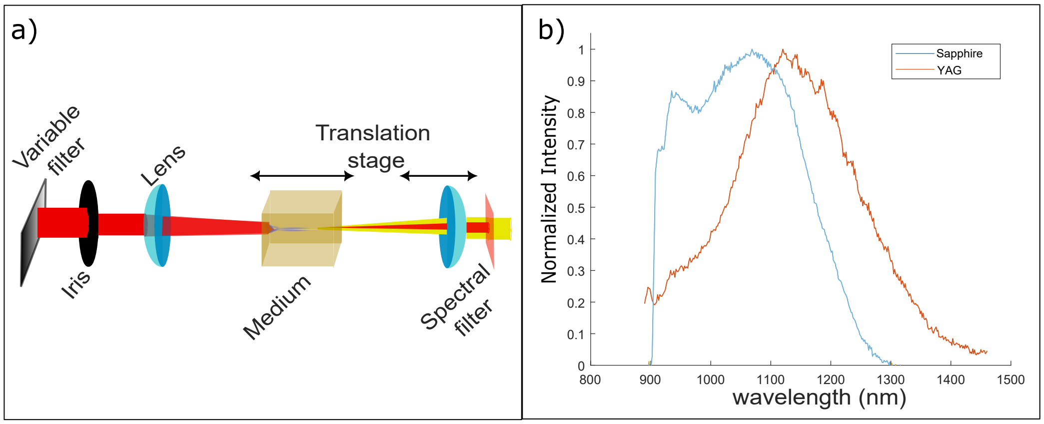

FIGURE 2.2: a) a setup for white light generation is shown schematically starting with beam attenuation and ending with spectral filtering that removes the original pulse. b) infrared component of white light generated with 120 fs pulses centered at 800 nm interacting with sapphire (blue curve) and YAG (red curve)

2.2.1 White light generation in a bulk solid-state medium

In this subsection the generation of white light in well-established solid media will be shown. This will allow to show a canonical setup for white light generation and some experimental considerations in this process.

For the generation of white light a pulse of light is focused by a lens on a material to concentrate a high density of photons and create conditions that favor self-phase modulation. The pulse energy can be varied by a variable attenuation filter, and the spatial mode of the focus can be modulated to a Bessel mode, which enhances the stability of the white light, by means of an iris in front of the lens. Due to the self focusing effect on the material, a beam recollimation requires a lens or a curved mirror mounted on a translation stage to optimize the relative distance to the focus, as shown schematically in Fig2.2 a). This beam is usually filtered in a final step to remove the spectral component that initiated the non-linear process, which is several orders of magnitude more intense than the generated white light component. This spectral filtering of the intense component of the beam is intended to eliminate possible future non-linear interactions between the beam and the material under spectroscopic study. The material serving as the medium for white light generation is mounted on a translation stage that allows its position relative to the focus to be changed, and thus optimized for different pulse energies. The medium must be transparent to the pulse wavelength, have a high damage threshold, allowing interaction with high electromagnetic radiation fluences, and have low chromatic dispersion. A high dispersion material can broaden the time profile of the interacting pulse over a short distance, reducing its peak power and minimizing the white light generation effect. The most commonly used media are solid media, being particularly interesting for the fundamental wavelengths of femtosecond titanium sapphire lasers centered at 800 nm, or for Ytterbium Femtosecond Fiber Lasers centered at 1030 nm, YAG and sapphire. As discussed in the previous section, white light generated in materials by interaction with pulses in the near-infrared and visible range will generally be restricted on the blue side by an ultraviolet cutoff dependent on the band gap of the material [BBR09]. The red side, on the other hand, offers greater freedom in spectral broadening, achieving for optimum conditions spectra such as those seen in Fig. 2.2 b). The spectra shown were obtained by interacting with pulses centered at 800 nm for YAG and Sapphire crystals, both 3 mm thick. Optimal conditions refer to conditions that maximize the spectral width of the white light signal for both crystals, these being: the interacting pulse power, iris aperture and crystal position. The aforementioned parameters are adjusted by measuring the white light spectrum while observing the spatial mode of the beam, looking for a clean and structureless mode in the white zone. A good indicator of good power and iris aperture in the spatial mode is in general the appearance of a red ring concentric to the conically emitted white light beam, which has been reported as a manifestation of filamentation [YM07]. For both crystals the signal optimization was achieved by closing the iris significantly, and with an intensity bounded at the upper part by the refocusing, being slightly lower than the intensity that starts to exhibit spectral fringes in the generated white light. The white light spectra in fig 2.2 show photons more in the infrared generated in the Yag compared to sapphire, even though sapphire has a slightly more homogeneous structure at different frequencies. The structure of white light can vary according to the wavelength at which it is pumped. Both the structure and qualities of white light will be further developed in the following discussion.

2.2.2 White light generation in liquids: water

This subsection shows an experimental setup that achieves stable white light generation in liquids under high repetition rate conditions. In particular, experiments have been performed in water, achieving a stability of the generated white light with a root mean square (RMS) of the signal intensity similar to that obtained with crystals, but with a higher intensity and spectral width when pumped with pulses centred at 1030 nm. This result defies discussions about the stability of white light generated in liquids, which is always considered to be lower than that generated in solids [BBR09].

The interaction of high fluences of pulsed electromagnetic radiation with materials, in addition to inducing non-linear responses in the medium, is accompanied by a thermal response that heats the material. The thermal responses depend on the conductivity and heat capacity of the medium and can range from reversible responses, such as a change in the refractive index as a function of the local temperature of the atoms, to irreversible damage to the structure of the material due to local lattice destruction. If the thermal relaxation time after a pulse-material interaction is longer than the time between pulses in a pulse train, the material will accumulate thermal charge left over from each interaction. As a result, each pulse will interact with a material with a different linear refractive index due to progressive heating of the material, causing high pulse-to-pulse instability in the white-light signal, rendering it useless for many types of experiments such as pump-probe. In addition, and more importantly, this accumulation of thermal energy can easily reach levels that cause irreversible damage to the material in a matter of seconds or a few minutes, with no further signal being generated. Thus, there is a fundamental limitation between materials used as non-linear media and the repetition rate of pulse trains for different wavelengths and hence with different thermal responses. In order to use crystals for white light generation with high pulse train repetition rates, ideas such as crystal rotation or translation have been successfully proposed in experimental setups such as Optical Parametric Amplifiers [TFB03]. Although these proposals allow the generation of spectrally broad white light in crystals with a low damage threshold such CaF_2 [Mid+02], they present intrinsic instabilities in their signals that are strongly dependent on the mechanical device that achieves the crystal motion, making them not ideal for certain applications in spectroscopy.

In liquid media, there is no risk of irreversible damage because there is no lattice, making it an ideal candidate for nonlinear interactions with strong fields. However, there are additional reversible responses that solids do not have, such as turbulence due to convection currents caused by a temperature gradient, or the generation of bubbles due to a local change of state of the liquid in the irradiated zone either by boiling or cavitation [Pod+21]. These effects generally make the signal non-linear response of liquids highly unstable. For this reason, liquids can generally only be used under conditions of very low pulse train repetition rates to prevent local heat build-up. In addition to these thermal responses, other effects such as currents in the fluid can affect the stability of the non-linear response by changing the density of interacting molecules with each pulse.

The strategy developed to optimise the stability of white light in a liquid medium consists of a constant volume substitution of the fluid interacting with the pulse train. This liquid volume substitution is accomplished by means of a fluid stream that must avoid heat build-up to a level that affects the stability of the white light generation, while minimising the turbulence effects of the stream. The thermal response of the liquid is directly related to the fluence of the pulse train with which it interacts. The fluence of the pulse train was established by maximising the spectral width and intensity without inducing effects such as plasma refocusing.

To define high repetition rates in this context, a white light generation experiment was performed in a liquid medium and the stability of the signal was analysed pulse by pulse for different repetition rates. Thus, high repetition rates are defined as rates at which the white light signal generated in the liquid medium

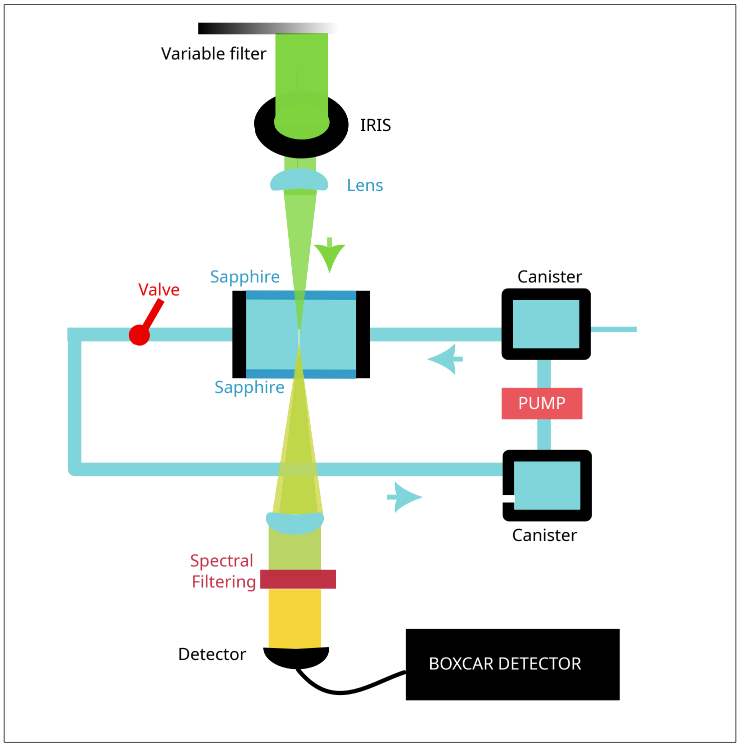

FIGURE 2.3: Experimental Setup:A water cell is connected to two canisters indirectly connected to a pump. To reduce vibrations, the canisters have openings that allow pressure regulation. In addition for a precise control of the velocity of the water particles in the cell a valve is placed in its outlet pipe. Optically this water cell is excited by pulses which are focused by a lens and an iris.

shows strong instabilities. Within the liquid media, water is a material with high potential for generating wide spectra of white light due to its high band gap [Fan+15] and low group velocity dispersion [DM07]. In order to have a pulsed source with a variable repetition rate, a Pharos laser from Light Conversion (Yb:KGW Laser) was used with pulses centred at a wavelength of 1030 nm with a duration of 220 fs and a second harmonic centred at 515 nm with a duration of 150 fs. The generation of white light with two different wavelengths implies a different thermal response in water as well as different plasma channel geometries. This versatility allows us to draw more general conclusions for the stabilisation of white light generation in liquid media. To generate white light in water, an iris to modulate the spatial structure of the light beam and a lens to generate a spot in a 5.6 mm water cell with sapphire windows were used. The focal length of the lens and the aperture of the iris were chosen to maximise the spectral width of the signal. The material of the windows was chosen for its high optical damage threshold, allowing intense pulses to enter. The signal is then recollimated by an output lens and the original pulse is removed by spectral filtering as shown in Fig. 2.3. Fig.2.4 shows the pulse-by-pulse intensity measurements measured with a boxcar detection scheme (UHFLI, Zurich Instrument) of the signal produced by pulses centred at 515 nm with a fluence of 90 mJ/cm^2 after filtering with a 540 nm long-pass filter as a function of the repetition frequency. These measurements show a stable signal for pulses with a repetition rate of 1 kHz, but a deterioration of the signal stability already at a repetition rate of 10 kHz.These signals show unstable regions where the signal tends to near zero intensity followed by sharp fluctuations in intensity, and other stable regions where the signal appears relatively constant with a maximum intensity. With increasing pulse repetition rate, shorter durations are observed for the stable and unstable regions, as shown in the inset of Fig. 2.4, showing a repetition rate-dependent signal decay and recovery dynamics. The latter observations may correspond to the expected effects of thermal charge accumulation due to the interaction of the liquid with the radiation, leading to convection currents in the water that displace the previously heated spot.

One way of stabilising white light in this context is to avoid the effects of thermal load accumulation which breaks the stability of the signal. In liquid media, the accumulation of thermal load can be solved by introducing a flow rate that renews the volume of water affected by the irradiation. This fluid movement can be introduced by means of a circulation system controlled by a liquid pump. However, introducing movement into the medium usually introduces new sources of instability, such as vibrations or turbulence caused by the pump mechanism or by a high flow rate in the water cell. In order to avoid external effects that could cause instability in the generation of white light in the water, we have proposed an indirect connection between the water cell and the pump. The indirect connection to the water pump consists in the use of an additional canister which accumulates pressure and allows the water to circulate in a closed

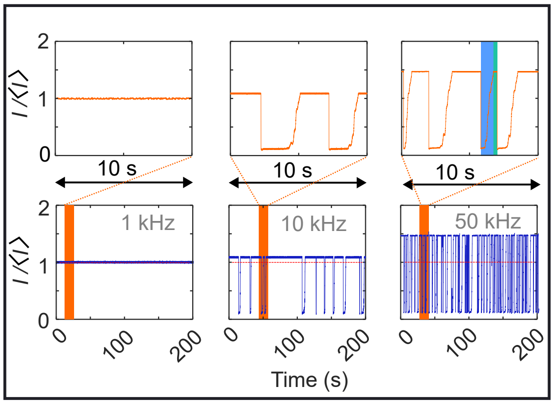

FIGURE 2.4: Measurement of pulse-to-pulse fluctuations of white light at different repetition rates. These measurements have insets with measurements of 10 seconds duration from where it is seen how the time between decays changes. In the 10 second inset for the 50 kHz case, two regions have been marked, a blue region where the intensity is close to zero or where there are strong instabilities and a green region, where the signal is stable and maximal.

circuit, thus attenuating mechanical vibration effects and irregular water flows. In addition, adjustable pressure valves are used to precisely control the flow rate, allowing an optimum flow rate to be found that maximises signal stability for different laser repetition rates under optimum pumping conditions. By optimal pumping conditions we mean the fluence that maximises both spectral intensity and spectral width.

Experimentally, it has been found that the optical conditions for pulses centred at 515 nm that optimise the signal are with a 50 mm lens and a numerical apperture of 0.01, regulated by the iris, and with a peak power at the focus of about $7.5MW$. This small numerical apperture implies a strong diffraction for the laser beam width of 2 mm, which produces an interference pattern in the form of concentric rings. This outer ring pattern acts as an energy reservoir, allowing a longer plasma filament and thus a wider spectral width of the signal, as well as optimising stability. In a medium where the local density of molecules changes due to the introduced flow, the use of a long filament makes the signal more robust to these local sources of instability. Similarly, for pulses centred at 1030 nm, an optimum was found using a 100 mm lens with a numerical aperture

TABLE 2.1: It shows the wavelength at which the white light signal generated in different media and different pumping pulses decays to 5% of the maximum on the blue and red sides of the spectrum. In addition, the spectral energy distribution per pulse for different wavelengths ($SEDP_{\lambda}$), defined by the spectral power in λ divided by the repetition frequency of the pulses, is shown for each case. $SEDP_{500nm}$* was extracted mathematically by comparing the number of counts with that of 671 nm and the $SEDP_{671nm}$ value.

Pump=515 nm				
material	$\lambda_{5\%,Red}$	$\lambda_{5\%,Blue}$	$SEDP_{700\text{ nm}}$	$SEDP_{450\text{ nm}}$
water	860 nm	415 nm	210 pJ	820 pJ
YAG	716 nm	442 nm	14 pJ	148 pJ
sapphire	747 nm	427 nm	76 pJ	124 pJ
Pump=1030 nm				
material	$\lambda_{5\%,Blue}$	$SEDP_{671\text{ nm}}$	$SEDP_{500\text{ nm}}$*	
water	415 nm	138 pJ	584 pJ	
YAG	492 nm	154 pJ	62 pJ	
sapphire	481 nm	162 pJ	266 pJ	

of 0.02, controlled by the iris, with a peak power at the focus of around $20MW$. In this case the iris does not produce a strong interference pattern, but since the order K factor of the equation 2.16 is higher than for the case with more energetic photons, its filament naturally becomes longer. In order to compare the characteristics of the white light generated under these two different pumping conditions in water with respect to widely used crystals such as YAG and sapphire, the spectra of these three signals have been plotted at the top of the fig. 2.5. This representation of the spectra for each pumping condition in the different media has been plotted to show the difference in spectral power for each situation, calibrated by measuring the power in a specific spectral range using a bandpass filter and a power meter. The power measured after using the bandpass filter allows us to extract the spectral energy distribution per pulse (SEDP) at different wavelengths dividing the power obtained by the pulse repetition rate. The values of the SEDP at different wavelengths are tabulated in the table 2.1, labelled as $SEDP_{\lambda}$, where the sub-index λ indicates the central wavelength

of the band pass used, which for all cases has a spectral width of 10 nm. Additionally in the table 2.1 is added the wavelength at which the spectral power of the white light in the different media is reduced to 5% of the maximum of the signal ($\lambda_{5\%,side}$) for the red and blue sides of the spectrum, thus allowing to quantify the spectral width of the signal in each case. From the data summarised in the table 2.1, it can be concluded that the white light produced in water tends to have a wider bandwidth and a higher SEDP than that produced in crystals, and this is more marked when pumped at 515 nm than when pumped at 1030 nm.

Optimising the stability by means of the water flow rate for a repetition rate of 50 kHz for these spectra, we observe a signal intensity stability as shown in Fig 2.5. The root mean square of the pulse-to-pulse signal of the white light generated in water for each spectrum is in each case comparable to the best case of white light generated in crystals. In order to understand how the RMS is affected by the flow rate, one experiment was carried out to measure this parameter for different flow rates at different repetition rates, the result of which can be seen in Fig. 2.6 a). For both repetition rates, a rapid decrease as $1/v^2$ of the RMS with the flow velocities (v) is observed up to a minimum point from which there is a linear growth. The existence of an optimum point can be understood as a trade-off between different sources of instabilities, one thermal and the other one turbulent. This assumption of different sources of instabilities can be strengthened by observing that in the spectral analysis of the noise for the same RMS but with a flow rate higher and lower than the optimum, they show different but consistent behaviour at both repetition frequencies. Looking at the spectral behaviour of the noise in Figures 2.6 a) and b), if we compare the curves with the same RMS value for a lower flow rate with a flow rate higher than the optimum, we see a similar behaviour, but with a slightly lower amplitud spectral density at low frequencies and a higher one at high frequencies. Considering the optimum flow velocity for the different repetition rates, and assuming a diameter of the water channel thermally affected by the irradiation in the tens of microns [Liu+16], an approximate time in which the water in the heated region is completely renewed can be extracted. The water exchange times extracted in this way are similar to

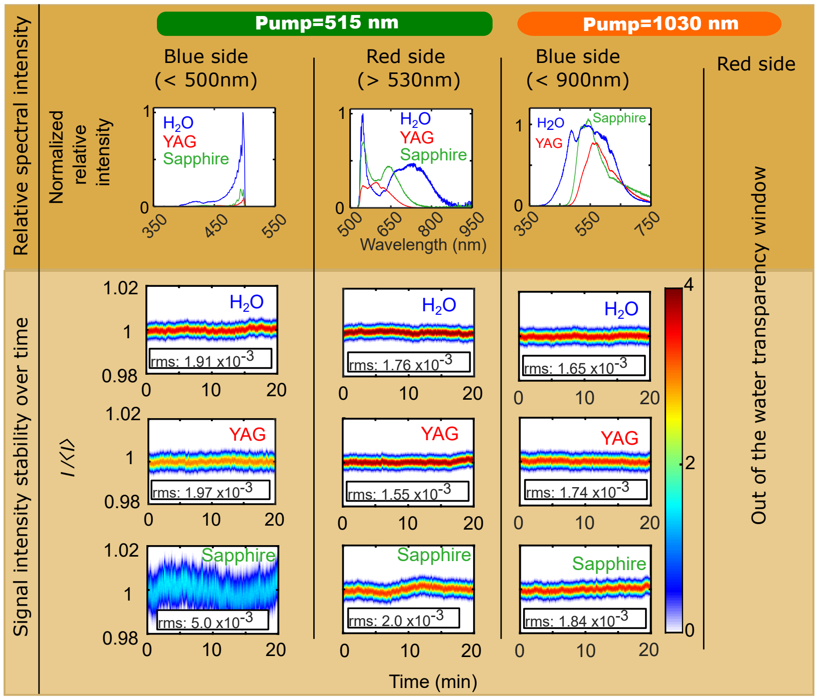

FIGURE 2.5: Different spectral components and pulse-to-pulse fluctuations of the white light generated under different pumping conditions and in different materials are observed. The upper part of the diagram shows the spectra normalised to the signal generated in the material at the maximum intensity in the specified range. The spectral curves plotted correspond to blue-water, red-YAG and green-sapphire. The pumping conditions are specified in the upper area in addition to the spectral filtering used. At the bottom is the noise analysis of the signals in the different materials for the spectra shown at the top of the column. Here a distribution of the signal is taken every second, allowing visualisation of the stability in the short and long time. For each spectrum generated, the root mean square (rms) for the 20 minutes of pulse-by-pulse signal measurement is shown in the signal fluctuation box.

the times between decays observed for different repetition rates in Fig 2.4. This fact strongly suggests that if water is exchanged just before the system has these signal interruptions, the white light obtained can have RMS levels similar to those of the laser that generates the nonlinear interaction[RA+23].

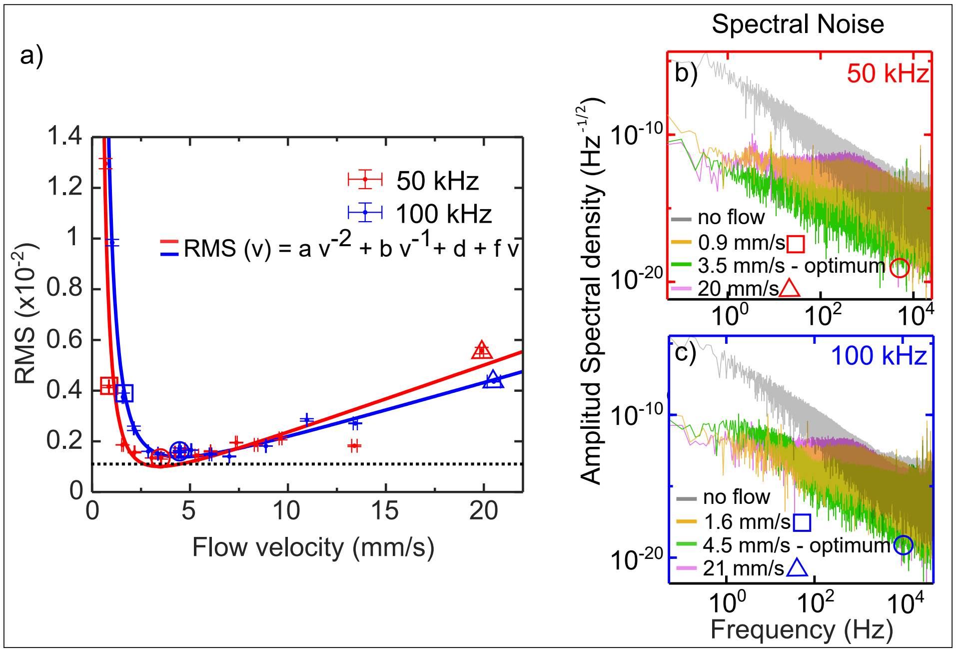

FIGURE 2.6: a) shows the pulse-by-pulse RMS fluctuation of the white light signal intensity as a function of water flow rate with pulse repetition rates of 50 kHz in red and 100 kHz in blue. Both sets of measurements were fitted by equations of the type $av^{-2} + bv^{-1} + d + fv$ with v flow velocity and the same colour code, allowing to recognise different possible origins of the instabilities. In addition, for each case, 3 points are marked with circle for the flow rate with the lowest fluctuation in each case, and a square and a triangle wich have similar RMS values at higher and lower flow rates than the case marked with a circle. The noise of these three marked cases plus the no-flux case are compared in b) and c) where the amplitud spectral density (ASD) is plotted as a function of frequency for 50 kHz and 100 kHz respectively. In both plots the no-flux case is grey, the lower flow case is yellow, the higher flow case is violet and the optimum case is green.

In this subsection, a new approach has been proposed that allows the generation of stable white light using water as a medium at repetition rates of hundreds of kHz, making it possible to exploit its superior spectral qualities compared to YAG and sapphire in a wider range of applications. To this end, a fluid velocity control system has been proposed that achieves maximum stability with velocities that allow the water to be completely renewed just before thermal effects appear that cause an abrupt braking of the white light generation. This velocity optimisation is necessary because, in addition to avoiding thermal effects, it is also necessary to avoid effects such as turbulence due to high fluid velocities, which reduce the stability of the white light signal. The same approach may be attractive in other liquid media which, for example, have a wider transparency window than water, allowing easy access to interesting wavelengths for studying the dynamics in different materials.

2.3 Optical Parametric Amplification (OPA) pumped by Ti:Sa Laser

2.3.1 OPA fundamentals

As mentioned in the section 2.1, a pump-probe experiment requires a probe pulse that is in resonance with a particular transition in a material, and a pump pulse that is more intense than the probe to excite the system under study. The requirement to excite a material with an intense pulse, and in many cases the need to centre it at a wavelength of particular interest, requires methods beyond white light generation, such as Optical Parametric Amplification (OPA). An OPA is based on the use of non-linear optical resources allowing to amplify the intensity of a specific spectral range of a white light pulse in a tunable way. In particular, the nonlinear resources used in an OPA are related to the second order tensor of the polarisation vector described in the equation 2.8, so that the use of a non-centrosymmetric material is required for this type of interaction. This subsection introduces the key theoretical concepts needed to understand how an OPA works, which will then be used to describe how the various OPAs available in the laboratory were constructed. The ultimate aim of this section is to motivate and show how the constructed OPAs work, so that it can be used to its full flexibility or even reconstructed by future students of the group. Although the description of second-order processes here is intended to explain how an OPA works, it can be easily adapted to explain other resources used, such as Second Harmonic Generation (SHG), Difference Frequency Generation (DFG) or Sum Frequency Generation (SFG).

Considering the equation 2.8, the second-order nonlinear polarisation response involves the product of the second-order susceptibility tensor with two oscillatory electric fields, which may or may not be the same. If these two oscillatory fields have different frequencies ω_i and ω_j, the phase of the total nonlinear polarisation response will be modulated in time by a frequency ω_k given by the sum or difference of the frequencies of the oscillatory fields involved. This time-phase modulation of the non-linear polarisation response involves the emission of new oscillatory fields with frequencies that mix the frequencies of the original fields, thereby generating either higher energy or lower energy radiation. While both frequency addition and subtraction are possible processes in non-linear interactions, the intensity of the wave generated for each case after the interaction will depend on the interference between the waves generated at each point of the interaction, allowing an exponential increase of the signal with the length of interaction, or a complete annihilation of the signal for certain lengths, depending on the difference of the wave vectors of the participating waves. This dependence on the frequency as well as on the wave vector can be understood in addition to the explanation presented here by means of the language of quantum field theory, from which, in analogy to classical mechanics, two conservation laws can be formulated: conservation of energy and conservation of momentum. The first conservation law states that if two photons are destroyed to create a new photon, the energy of this new photon will be equal to the sum of the previously destroyed photons. This conservation law is expressed by the equation

$$\hbar\omega_3 = \hbar\omega_2 + \hbar\omega_1. \tag{2.17}$$

The second law assumes conservation of momentum in the process of destroying two photons to create a third, defining momentum by the product $\hbar \cdot \vec{k}$, where $\vec{k}$ is the wave vector of each photon. This law is expressed mathematically as

$$\hbar\vec{k}_3 = \hbar\vec{k}_2 + \hbar\vec{k}_1. \tag{2.18}$$

These conservation laws can be further represented schematically as shown in Fig 2.7 a) and b), being conservation of energy and momentum, respectively. From equations and it can be seen that both, the generation of the sum and the difference of the frequencies, are described in a common way, the only difference between them being the role played by the generated frequency. Since in the language of quantum field theory, as in other descriptions, three different types of photons must be used, processes arising from second-order nonlinearity are generally referred to as three-wave mixing.

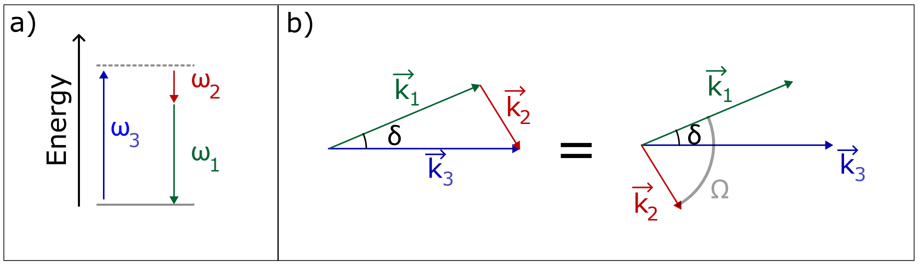

FIGURE 2.7: Conservation law: a) Pictorial representation of the conservation of energy in a three wave mixing process. In b) the conservation of momentum between the 3 waves is represented, in addition to the geometrical relation that exists between the angles of the wave 3 -1 and 1-2.

A linearly polarised wave propagating in a birefringent crystal () is subject to an index of refraction which depends on the direction of propagation of its wave vector with respect to the crystal axes and its polarisation. The refractive index of the material as a function of the polarisation and the direction of propagation of a wave depends directly on the geometry of the second order susceptibility tensor. By diagonalising the second order susceptibility tensor in a crystal, it is possible to extract the direction of 3 orthogonal axes, whose orientation is directly related to the crystallographic axes of symmetry of the crystal, and 3 principal values, each associated with the different axis.The principal values calculated by this procedure are the values of the refractive index associated with the direction of the determined axis. If the symmetry of the crystal has three different refractive indices, it has three fixed axes and is referred to in the literature as a biaxial crystal. If on the other hand only one of its indices is different, which is called extraordinary refractive index in contrast to the same ones which are called ordinary refractive index, it has only one fixed axis and is called a uniaxial crystal.Since the axes are perpendicular to each other and are associated with different refractive indices, it is usual to represent this information on a polarization ellipsoid where the length of the orthogonal semi-axes is given by the refractive index values. In the particular case of a uniaxial crystal, if the electric field vector of a wave lies in the plane formed by one of the axes associated with the extraordinary refractive index and another ordinary one, the refractive index to which the radiation is subjected depend on the angle θ formed between the wave vector of the electromagnetic wave and the axis associated with the extraordinary refractive index. This angular dependent extraordinary refractive index is $n_e(\theta)$ is described similarly to the equation describing the ellipse of polarization in polar coordinates, given by

$$\frac{1}{n_e(\theta)^2} = \frac{cos^2(\theta)}{n_o^2} + \frac{sin^2(\theta)}{n_e^2}, \tag{2.19}$$

where n_e is the extraordinary refractive index and n_o is the ordinary refractive index extracted from the diagonalization. In a uniaxial crystal, if a wave travels with a wave vector in the direction of the fixed axis, the refractive index does not depend on the polarisation, so this axis can be identified as the optical axis of the system. Since the OPAs constructed in the course of this PhD were based purely on nonlinear pulse interactions in uniaxial crystals, this crystal geometry will always be assumed in the following, unless otherwise stated. Given the relationship between the wave vector and the polarization with the refractive index, the equation 2.3.1 can be rewritten in a form that accounts for this fact, given by

$$n_{\vec{k}3,p3}\omega_3 = n_{\vec{k}1,p1}\omega_1 + n_{\vec{k}2,p2}\omega_2, \tag{2.20}$$

where the notation with two subindices in, $n_{\vec{k}1,p1}$ refer to the direction of the wave vector with respect to the optical axis and the polarization of the beam, in an equation called the phase matching equation.

The effect of three-wave mixing in a non-centrosymmetric material can be described by the evolution equations in the direction of propagation z of the fields involved assuming $E(z,t) = A(z)e^{i(xk-\omega z)}$ with $A(z)$ a phasor and ($|\partial^2 A/\partial z^2| \ll 2k|\partial A/\partial z|$) as [Boy03],

$$\frac{\partial A_1(z)}{\partial z} = -ikA_2^*(z)A_3(z)\cdot e^{-i\Delta kz}, \tag{2.21}$$

$$\frac{\partial A_2(z)}{\partial z} = -ikA_1^*(z)A_3(z)\cdot e^{-i\Delta kz}, \tag{2.22}$$

$$\frac{\partial A_1(z)}{\partial z} = -ikA_1(z)A_2(z)\cdot e^{i\Delta kz}, \tag{2.23}$$

where the sub-indices are consistent with those represented in the Fig. 2.7, $\Delta k = k_1 - k_2 - k_3$ and * is the complex conjugate. One effect described from these equations and involving only two waves with non-zero initial amplitude is the amplification of the intensity of one wave due to the transfer of energy from the other wave with the shortest wavelength and highest intensity. This process is known as optical parametric amplification, and in this context the shortest wavelength wave is called pump, the amplified wave is called signal and the wave that is created by the interaction of the two is called idler. For the amplification process to take place, the pump intensity must be orders of magnitude stronger than the signal and the efficiency of the amplification process depends on the value of Δk. In general, Δk depends on the direction of the participating waves, being possible to identify a case with collinear and a case with non-collinear waves, and in polarisation identifying 3 types of possible combinations called type 0, type 1 and type 2. Type 0 is understood as when the three waves have the same polarization, type 1 idler and signal have the same polarization and this is orthogonal to the pump, and type 2 when idler and signal are orthogonal to each other. Due to the freedom allowed by the extraordinary angle-dependent refractive index in a uniaxial crystal, OPA generally uses types 1 and 2, since type 0 is normally restricted to the chromatic dispersion of the medium.

The concepts presented so far allow the amplification of a signal by nonlinear interaction with a pump, assuming that both waves are monochromatic. However, in the context of this thesis, the amplification of pulsed signals with a wide bandwidth is desired, which implies an extension of the concepts previously introduced. Typically, the amplification of pulsed signals uses a narrow spectral width pump from commercial oscillators, and the signal comes from the generation of white light by the interaction of pulses with materials. The spectral width of the signal and the subsequent spectral width of the idler can be accounted for by Taylor series expansions of the wave vectors for both pulses, given by

$$k(\omega_{1c}+\Delta\omega)=k(\omega_{1c})+\Delta\omega\left.\frac{\partial k(\omega)}{\partial\omega}\right|_{\omega=\omega_{1c}}=k(\omega_{1c})+\frac{1}{vg1}\Delta\omega \tag{2.24}$$

for the signal whith ω_{1c} its central frequency,

$$k(\omega_{2c}+\Delta\omega)=k(\omega_{2c})+\Delta\omega\left.\frac{\partial k(\omega)}{\partial\omega}\right|_{\omega=\omega_{2c}}=k(\omega_{2c})+\frac{1}{vg2}\Delta\omega, \tag{2.25}$$

and for the idler whith ω_{2c} its central frequency, and where $vg1$ and $vg2$ are the group velocities for the signal and idler. Thus, if the wave vectors between the signal pulse and the idler have an angle Ω between them, as shown in Fig. 2.7 b), the conservation of momentum will imply that the bandwidth optimizing condition will be given by [MC16],

$$vg1=vg2cos(\Omega). \tag{2.26}$$

The implication of this condition is that if $vg2$ is greater than $vg1$ there is an Ω angle between the signal and the idler that maximises the amplified spectral range. To achieve an Ω angle between signal and idler a δ angle between signal and pump must be fixed. The relationship between the delta and Omega angle is given in Fig 2.7 b). The δ angle between the pump and the signal means to have an OPA with a non-collinear configuration, which as stated above is one of the degrees of freedom to optimise the amplification.

2.3.2 VIS OPA

The first challenge in constructing an OPA driven by a Ti:Sa laser in the visible range is to promote the generation of harmonics of the fundamental optical frequency of the laser in order to have a pump with a wavelength shorter than the amplified region. In our case, we have used the generation of the second harmonic (SHG) to obtain a pump with a wavelength of 400 nm, for which we have arranged a two millimetre uniaxial BBO crystal cut in such a way that a laser incident parallel to the normal vector of the crystal has a $\theta = 29.2^{\circ}$ with respect to the optical axis. This harmonic generation can be optimized by concentrating high photon densities either by focusing or by using a telescope to reduce the beam cross-sectional area. Given the possibility of using wide crystals, it is generally preferable to avoid non-flat wavefronts that may reduce the efficiency of the process due to angles in the wave vector, making the use of telescopes optimal. The telescope used was selected such that by setting the incoming beam intensity to 40 μJ, and extracting 10 percent of the power by means of a 90:10 beamsplitter for white light generation, the second harmonic signal is about 40% of the total incoming power of the fundamental pulse, as shown in fig 2.8.

After the non-linear crystal the beam has a signal that mixes waves with wavelengths centred at 400 nm and 800 nm. To remove the radiation with a wavelength centred at 800 nm the beam is reflected multiple times in mirrors (HR 400- Layertec) optimised for 400 nm signal reflection and very inefficient at 800 nm reflection. This pulse centered at 400 nm is mixed in a nonlinear crystal with the visible component of pulsed white light generated in sapphire for amplification of the latter. To optimize the spectral width of the amplification, a relatively similar time duration is sought between the white light that has a non-optimized spectral phase and the pump pulse of the amplification. The latter comes from the fact that if the white light has a spectral phase such that photons with different energies are inhomogeneously distributed along the pulse, and the pulse has a longer time duration than the pump, the pump can potentially only amplify in a nonlinear process the frequency range with which it has a temporal overlap. In order not to add too much spectral phase in the white

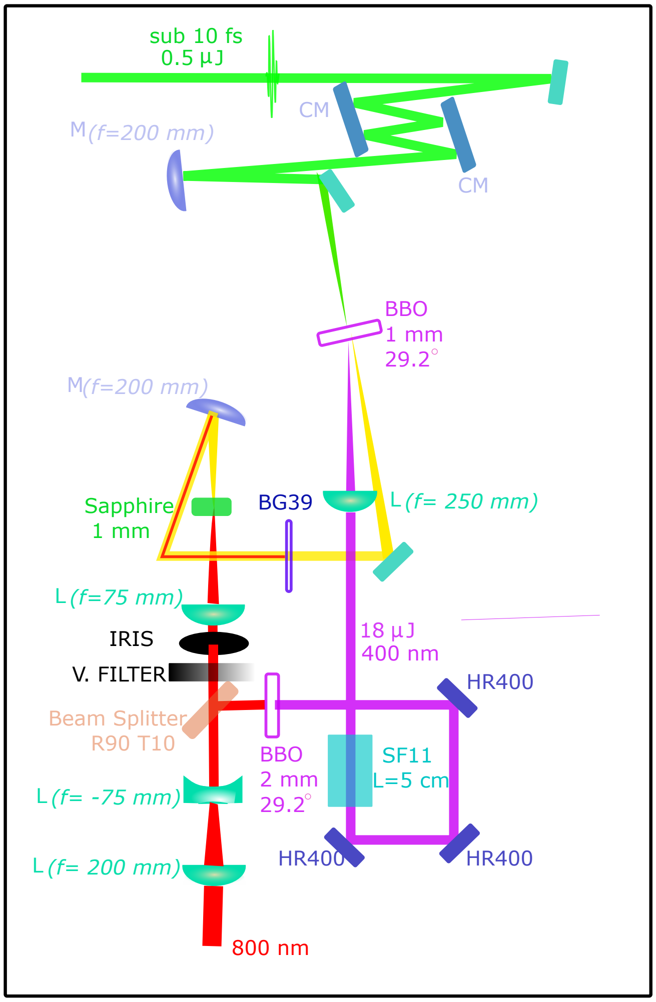

FIGURE 2.8: Experimental setup for a VIS OPA, with M spherical mirrors, L lenses, SF11 a SF11 glass block functioning as a dispersive medium, BG39 which is a glass with good transmission between 400 nm and 790 nm, CM Chirp mirrors and HR400 high quality mirrors for 400 nm and V filter a variable attenuation filter.

light pulse, the transmission by different materials must be reduced, including the glass where it is generated, being only 1 mm, not using lenses, being focused by a curved mirror, and being transmitted only by a glass that transmits only the part that is to be amplified. Additionally, to increase the temporal overlap between pulses, a block of a dispersive material with high transmission of 400 nm

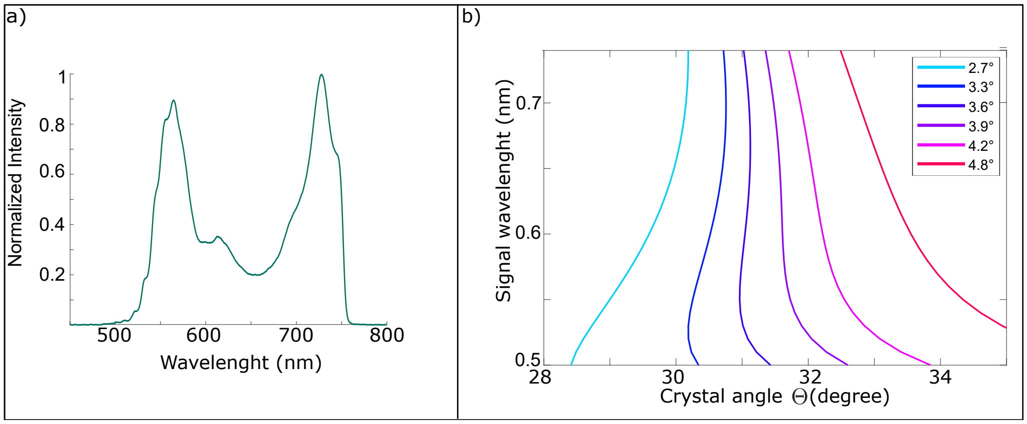

FIGURE 2.9: a) Normalized spectrum generated by VIS OPA. b)The plotted curves show the phase matching equal to zero for different angles between the pump centred at 400 nm and the signal as a function of signal wavelength and crystal angle θ.

wavelengths, such as SF11, is placed in the path of the pump, generating a temporal broadening of the pulse, optimizing the temporal overlap. This pump is focused with a 250 mm UVFS lens two centimeters in front of a 1 mm BBO crystal cut at an angle of $\theta = 29.2°$, and the amplified pulse is recollimated by means of a spherical mirror with a 200 mm focus. The optimum spectrum achieved is shown in Fig.2.9 a) spanning from 500 to 750 nm which was achieved with an angle $\theta = 31°$ with a phase matching type 1 and an angle $\delta \approx 3.5°$ between Pump and Signal inside the crystal as shown in Fig. 2.9 b), achieving a power of 0.5 mW. The amplified spectrum in an OPA VIS with a pump centred at 400 nm and a white light signal generated by the interaction of a sapphire crystal with the fundamental pulse of the laser centred at 800 nm, has limits on the blue side at wavelengths around 400 nm and on the red side at wavelengths shorter than 800 nm. The first limit, on the blue side, relates to a fundamental limit in white light generation, which states that the shortest possible wavelength that can be generated in this way is a function of the band gap of the medium used, and which was already discussed in the section 2.2. In the case of a sapphire crystal, the limit of the shortest wavelength that can be achieved is a little more than 400 nm, which limits the amplification to this range. The limit on the red side is also related to the spectrum of white light, which has a very high spectral intensity near the wavelength that initiated the generation of white light, which can be several orders of magnitude more intense than wavelengths generated in more distant spectral regions. The presence of a very intense spectral component relative to the rest can increase the probability of additional nonlinear effects that reduce the pump energy for amplification, and the amplified region will have a much narrower spectral FWHM compared to amplification over a more homogeneous spectral distribution. For this reason, in our case, the white light has passed through a filter that eliminates waves with wavelengths longer than 750 nm. The minimum time duration of the pulse with the obtained spectrum is 4.9 fs considering the FWHM of the time envelope of the amplitud of the electric field. In our case, for a particular alignment, the amplified signal was sent to a pair of Chirp Mirrors achieving pulses with a temporal duration of 9 fs FWHM in the field amplitude envelope after 6 reflections in each mirror.

2.3.3 NIR OPA around 1 μm

Parametric amplification is a process based on the interaction of three waves along a crystal. If one of the waves has a much higher or lower group velocity than the others in the crystal, the amplification stops when the temporal overlap of the three waves is lost. Similarly, if the absorption coefficient of one of these waves is very high, the interaction with the other waves quickly becomes negligible, making parametric amplification impossible. The amplification of a signal with wavelengths very close to the pump implies a very low energy idler, which in general is quickly absorbed in crystals in intraband processes. For the BBO, as a common crystal for parametric amplification, wavelength higher that 3 μm have a high absorption rate [Tam+18]. Amplification of pulses with wavelengths centred at 1 μm using a pump centred at 800 nm implies an idler with a wavelength of 4 μm, which is rapidly absorbed in the crystal. In order to use this crystal while amplifying the signal around this wavelength, a possible solution is to have a more energetic pump, making the idler less infrared. Using the second harmonic of pulses centered at 800 nm with a signal at 1 μm implies an idler centered at 670 nm, which can be transmitted in a BBO.

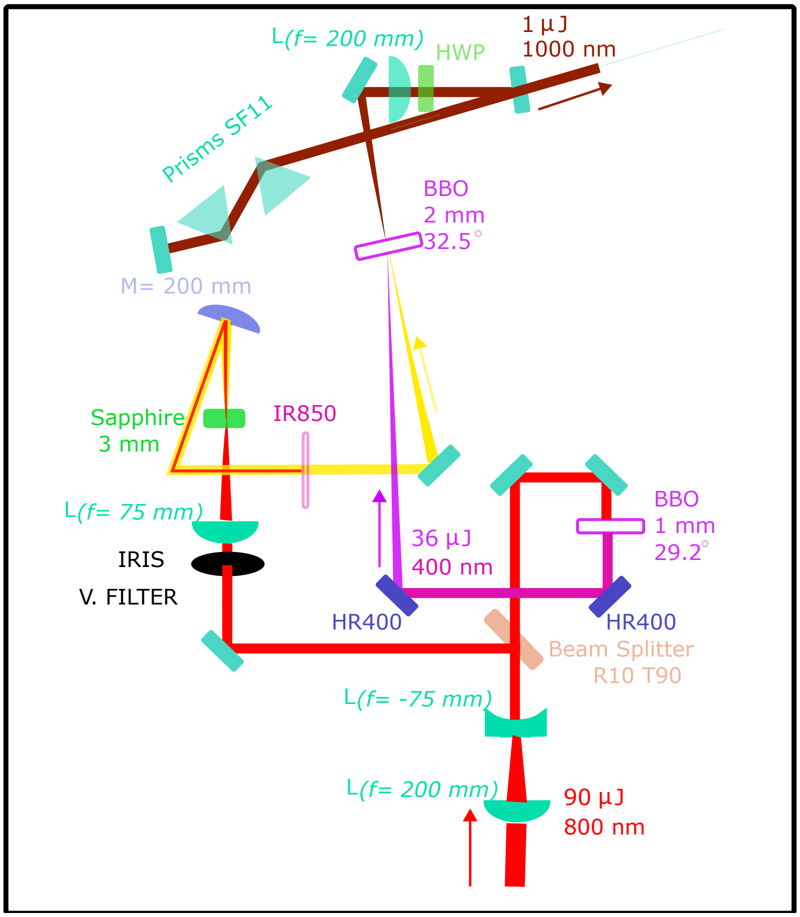

FIGURE 2.10: Experimental setup for a NIR OPA operating between 850 and 1080 nm, with the same notation as the previous OPA. Additionally, SF11 prisms have been added which are brewster prisms of the SF11 material and a IR850 Which is a glass that transmits high energies above 850 nm more efficiently.

The OPA constructed for amplification in this range, shown in Fig. 2.10, has several similarities with the OPA for the visible range. With the same idea as for the OPA in the visible range, a telescope has been arranged to maximize the second-harmonic generation efficiency for the Pump in a 1 mm BBO crystal cut with a $\theta = 29.2°$, producing pulses centered at 400 nm with an energy of 36μJ. This telescope is intentionally misaligned to achieve a focus near the nonlinear crystal that mediates amplification without the use of a lens, thereby reducing

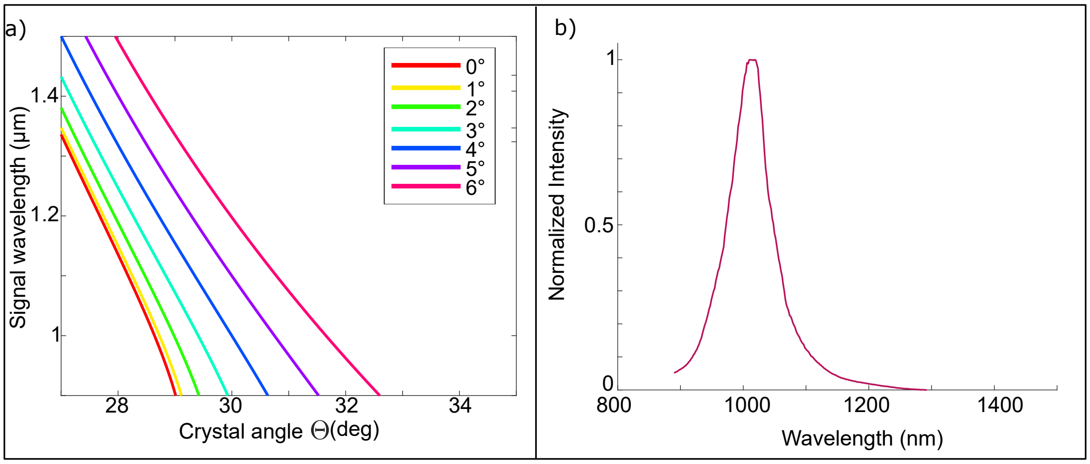

FIGURE 2.11: a) The plotted curves show the phase matching equal to zero for different angles between the pump centred at 400 nm and the signal as a function of signal wavelength and crystal angle θ. b) Normalized spectrum generated by NIR OPA.

the size of the experimental setup. The Fig. 2.11 (a), shows the phase matching curves as a function of the angle between the pump and the signal and the crystal angle. The curves show that the geometrical conditions of the crystal make it impossible to amplify a wide spectral range, only managing to amplify a short range of wavelengths, even in the collinearity situation between Pump and Signal. The impossibility to amplify a wide spectral range allows to relax the considerations about the time overlap between Pump and Signal in relation to an VIS OPA. Some differences in the set-up of a VIS OPA and a NIR OPA in this range are that the latter does not need to have a dispersive medium for the second harmonic as well as being able to use a longer sapphire crystal for the generation of white light, being in this case 3 mm, achieving higher intensities. Another difference between the OPAs is that in this case the red side of the white light spectrum is used, being filtered by the use of an IR850 glass. Using the smallest angle that the experimental setup allows, a spectrum like the one shown in Fig. 2.11 b) was achieved with an energy per pulse of 1μ J. The minimum time duration of the pulse with the obtained spectrum is 20 fs considering the FWHM electric field amplitude. In particular by compressing this pulse by means of a pair of SF10 prisms with the freedom to change the distance between them as well as the position where the beam penetrates the prisms, a pulse with a FWHM of 27 fs in its temporal duration was achieved from the OPA.

2.3.4 NIR OPA

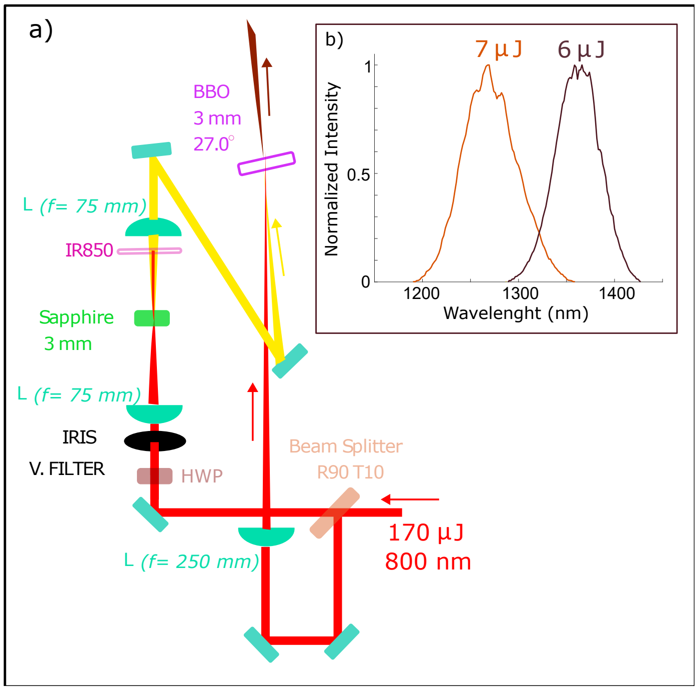

FIGURE 2.12: a)Experimental setup for a NIR OPA operating between 1200 and 1400 nm. In b) are added some spectra that are possible to generate using this OPA

A signal with a wavelength greater than 1050 nm and a pump centered at 800 nm produces an idler that can be transmitted in a BBO crystal, allowing the signal to be amplified. The experimental setup of this OPA is shown in Fig 2.12 a). For this configuration, 10% of an input pulse energy of 170 μJ is directed to a sapphire crystal for white light generation, while 90% can be used as a pump in a parametric amplifier. For the signal, a white light is generated by interacting an 800 nm pulse beam with a 3 mm sapphire crystal, in a configuration that maximises the generation of wavelengths longer than 1200 nm. The pump is focused by a 250 mm lens and its focus is formed approximately 3 centimeters before the nonlinear crystal. The nonlinear crystal is a BBO with $\theta = 27^{\circ}$, which favours amplification for type 2 processes with orthogonal polarisation between signal and pump. To establish orthogonal polarisations between the signal and the pump, a HWP for 808 nm is installed before the white light generation, which preserves the polarisation. Although phase matching type 2 for pump and signal pulses with orthogonal polarisations to each other and phase matching type 1 are similar in spectral width and efficiency, the former was chosen mainly to be able to filter the idler by polarisation. The signal focus is practically at the position of the BBO crystal, achieving pulse energies of ≈ 7 μJ for pulses centered at 1370 nm, and ≈ 6 μJ for pulses centered at 1260 nm with normalised spectra as shown in 2.12b). These spectra allow pulses with a FWHM of their temporal profile of 39 fs for the one centred at 1260 nm and 51 fs for the one centred at 1370 nm. This versatility of amplified wavelengths can be achieved by rotating the non-linear crystal in such a way that the angle between the pump wave vector with respect to the optical axis of the BBO is slightly adjusted.

2.3.5 Double Amplification NIR OPA

The generation of waves in different spectral ranges depends on nonlinear effects in materials, which can be very inefficient. The higher the energy per pulse, the easier it is to promote nonlinear responses in materials. This is a resource that can be used to generate frequencies in spectral ranges far from the fundamental laser frequency by non-linear effects using one or two intense pulsed beams. The efficiency of the non-linear processes depends strongly on the material used and the wavelength of the beam promoting them, in some cases requiring multiple amplification at a given wavelength before a sufficiently strong non-linear interaction is obtained. A multiple amplification scheme is the use of the previously amplified signal from an OPA as the initial value in a subsequent amplification process, the important one in our case being double amplification. Examples of the generation of new frequencies requiring intense, wavelength-tunable pulses, as achieved by double amplification, are the generation of intense pulses at frequencies of a few terahertz or in the MIR, using 1 or 2 pulses respectively. Both processes are discussed in this thesis, the first one being discussed in section

5.5.1 and taken to very high intensities at frequencies accessible by the OPA systems presented here in [VMH14], and the second one discussed in section 2.3.6

A requirement for the second amplification to take place is that the pump of the second process is at least one order of magnitude higher than the pump of the first OPA. The intensities required for a second amplification cannot generally be focused on a crystal due to possible damage to the crystal structure. For this type of OPA the size of the pump is reduced by means of a telescope to a radius similar to the 6 mm radius of the crystal used, concentrating the photon density driving the amplification. The mirrors used for this intense beam are HR 800 from Layertec which are high reflectivity mirrors for 800 nm. In order to optimize the amplification a scheme is used where the pump and the signal are collinear, for which a Layertec 1200/800 combiner is used which transmits the wavelengths of 860-1600 nm and reflects the range of 740-840 nm. To maximise process efficiency, the signal and pump must have an imperfection-free spatial mode and equal cross-sectional size. The cross-sectional area of the signal can be controlled by using a telescope, which collimates the signal to the desired radius. A possible source of imperfections in the cross-sectional mode of the pump may come from foci in its optical path, and eventual ionization of the molecules in the air, generating a diffraction pattern in the beam. For this reason the telescope used in the Pump avoids focusing by using a collecting lens with a negative focal length. The crystal used for amplification favors a type 2 configuration where signal and pump are orthogonal polarized, this being a 4 mm BBO with a $\theta = 27^{\circ}$. The amplified signal passes through a new 1200/800 combiner which removes the pump from the signal. Additionally the process generates the second harmonic of the pump which can be removed by means of a 400/1200 combiner from Layertec which transmits light in the range of 900-1800 nm and reflects 380-420 nm, as shown in the Fig. 2.13 a). Since the phase matching used in the second amplification is analogous to the first, the pulse spectra do not change much, with only a small reduction in spectral width, as can be seen in Fig. 2.13 b). The signal obtained has energies per pulse ranging from 270 μJ for a signal centred at 1260 nm to 390 μJ for a signal centred at 1370 nm.

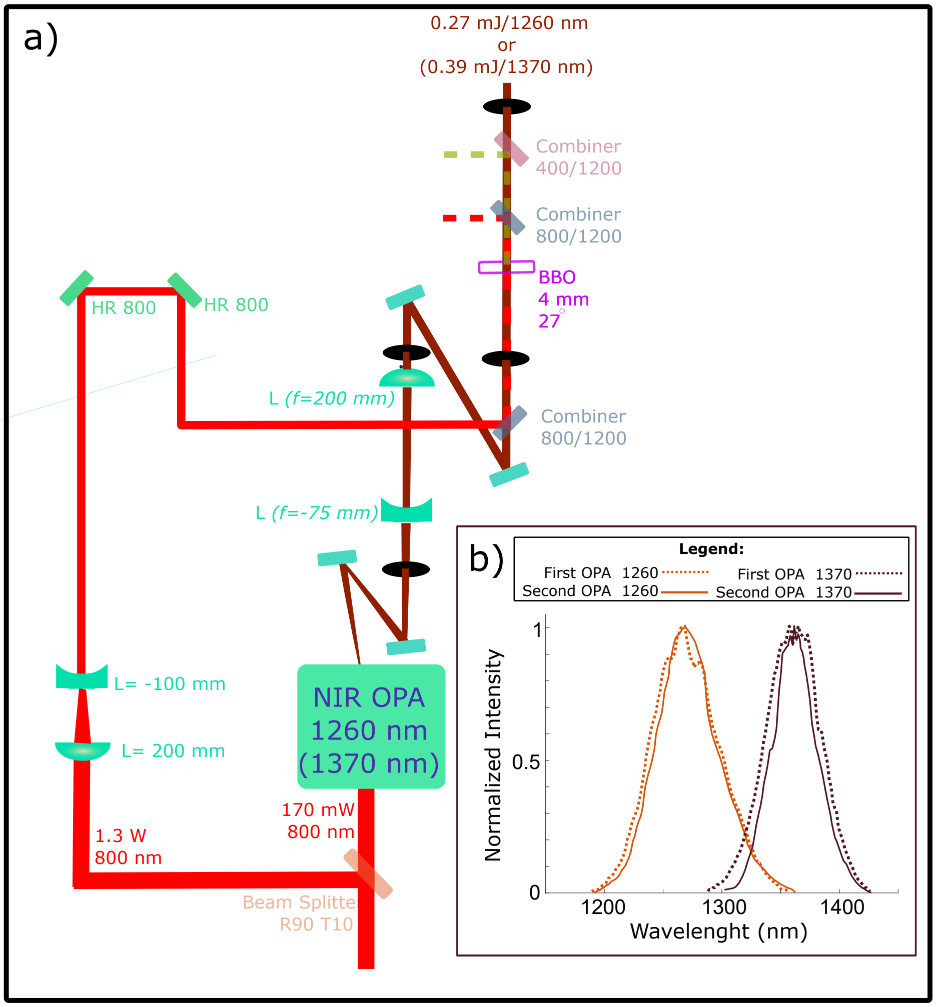

FIGURE 2.13: a)Experimental setup for double amplification NIR OPA. HR 800 high quality mirrors for 800 nm, NIR OPA refers to the experimental setup of the NIR OPA operating at the wavelength written below. Combiner 800/1200 are mirrors that allow the reflection of wavelengths in the vicinity of 1200 nm but reflect 800 nm. Similarly, Combiner 400/1200 nm mirrors reflect very well in the neighbourhood of 400 nm. The figure also shows the position of the irises that facilitate the daily alignment of the system. b) Normalized spectra of pulses before second amplification coming from a NIR OPA in dashed lines, and normalized spectra of amplified pulses in a second OPA in solid lines.

2.3.6 Generation of intense pulses in the MIR.

While in the section 2.1 which introduced the pump-probe experiments, both pulses were resonant at the interband transition of the two-level system, this condition is not strictly necessary in a condensed matter system, and subtleties need to be considered. Strictly speaking, the pump pulse should only be the precursor to a change in the dielectric response of a material, and the probe pulse should test at least part of the transient dielectric response promoted by the pump. Thus, if the conditions described above are met, both the pump and the probe can have energies that are far from the energy required for interband electron transitions. In the section 5.4 a case is presented where the probe is out of resonance with any interband transitions in the system and acts as an electric field allowing the mobility of charges previously excited by a pump. Similarly, the electric field of the pump pulse of amplitude E_0 and frequency ω, out of resonance with any transition in the solid, can generate a tilt in the band structure ($V_c(r)$), described by

$$V(r,t) = V_c(r) + rE_0 sin(\omega t), \tag{2.27}$$

to a point where tunneling between the valence and conduction bands is possible, as seen in Fig.2.14 a), promoting a change in the dielectric response of the material. This interband tunneling, which can also be described by the poweromotive energy U_p of the electrons interacting with the electric field, is a process that cannot be studied in a perturbative way, being fundamentally different from processes such as ionisation by multi-photon absorption (I_p) depicted in Fig. 2.14 b). In the literature, a parameter γ_k called keldish parameter, has been defined, to determine a ratio between the ionisation potential of a medium by multiphoton absorption and the ponderomotive energy, given by,

$$\gamma_k = \sqrt{\frac{Ip}{2U_p}}. \tag{2.28}$$

Therefore, if $\gamma_k \gg 1$ the system is ionised by multiphoton absorption, if

$\gamma_k \ll 1$ the change in the dielectric response is associated with tunneling processes, and if it has an intermediate value $\gamma_k \sim 1$, the combination of both processes allows the change in the dielectric response as shown in Fig.2.14 c). The amplitude of the electric fields that promote changes in the dielectric response of the medium in a non-perturbative way is a function of the lattice period of the material (D) and the band gap energy (E_g), with an amplitude of the order of $E_0 \approx Eg/De$ being e the fundamental electron charge. In general for semiconductors this amplitude of electric field is in the order of 10 MV/cm. In the context of the effect of injected charges in a heterojunction, mention must be made of the effects that charge tunneling between materials favoured by an electric field, see section 3.2, can cause.Of particular interest in this context is impact ionisation, where an electron in the valence band impacts with an injected charge of high kinetic energy due to the effect of the intense electric field, creating an electron-hole pair that alters the dielectric response of the material. This effect has been demonstrated experimentally using THz radiation in InAs/AlSb heterostructures [Met+03] and its theoretical relevance has been discussed in [Cao+02].

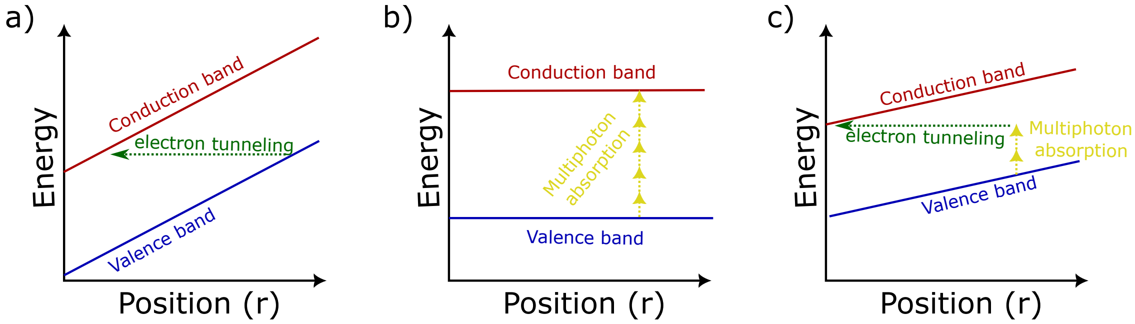

FIGURE 2.14: Scheme of possible mechanisms for the promotion of electrons from the valence band to the conduction band by means of an intense oscillating electric field out of resonance: a) via tunneling, b) via multiphoton absorption and c) combined effects of the two previous ones.

To obtain high peak field pulses in the MIR, two intense pulses were mixed in a DFG process in a nonlinear medium and with an energy difference corresponding to this spectral range. The intense pulses mixed in the DFG are obtained by double amplification as shown in 2.3.5 with centered spectra with a difference of about 100 nm between them, directed in the setup by dielectric mirrors (102077-Layertec) for this spectral range. Since the NIR pulses used in the mixture have a wavelength of about 1000 nm, they will have a wave vector about 10 times longer than the generated pulses. This difference in the length of the wave vectors means that a small angle between the beams in the NIR will make the emission angle of the radiation in the MIR almost orthogonal to the original pulses, making them difficult to collect and align. To avoid such difficulties, the pulses in the NIR have been aligned collinearly, making use of an achromatic half-wave plate operational for 1100-2000 nm wavelengths from Thorlabs (AHWP05M-1600), which rotates the polarization of one of the beams, and a PBS optimized for the range between 1100-1600 nm from B-Halle, as shown in Fig. 2.15 a). For the optimization of the time overlap between the pulses, one of the beams is reflected in a retro configuration on a translation stage demarcated as $\Delta\tau_1$. The two collinear beams are directed to a mirror on a magnetic mount, which allows a line to verify the alignment, i.e. collinearity and time overlap, or to continue to the crystal where the MIR pulses are generated. For the collinearity verification, the alignment line can be reflected several times to verify that over a long distance the two beams are not spatially separated. To verify the temporal overlap, the alignment line is directed to a HWP and then a PBS, projecting part of the oscillation of the two pulsed fields on the same axis and with equal intensity, thus allowing interference and the appearance of fringes in the common spectral region for the two pulses. The spectral width of the interference fringes is inversely proportional to the temporal separation between the pulses. Thus, optimization of the temporal overlap can be achieved directly by maximizing the width of the fringes measured on a spectrometer. Once the collinearity and temporal overlap are verified, the beam is reflected by two mirrors allowing to align the system by making use of a pair of irises, and entering a new retro configuration $\Delta\tau_2$. This new retro configuration does not play any role in the generation of MIR radiation, however it is relevant to find a possible temporal overlap between the pulse generated here and an external pulse. This retro configuration is constructed before the nonlinear mixing and generation of pulses in the MIR, because in general it is recommended to minimize the optical path at these wavelengths in order to decrease its absorption due to molecules such as CO_2 and H_2O present in the air. After retro-configuration, the pulses are directed onto a 1 mm Gallium Selenide (GaSe) crystal which, by pulse mixing, where the pulse centred at 1260 nm is subjected to an angle dependent extraordinary refractive index and 1370 nm is subject to an ordinary refractive index allows the generation of pulses centred at 15692 nm with equal polarisation to the pulse centred at 1370 with a $\theta = 11,9^\circ$, or with equal polarisation to the other pulse with a $\theta = 12.4^\circ$. In general for materials with hexagonal structure such as GaSe the optical axis is oriented in the direction of the normal vector of the two-dimensional plane [Bor+99].This geometry implies that the optical index can be adjusted by an angle between the normal vector of the crystal plane and the angle of the incident beam wave vector, which we will call β as shown in the Fig. 2.15 b). Additionally, to optimize the signal, the crystal must be rotated by taking the normal vector of the crystal plane as the rotation axis. Since the angle θ refers to an internal angle of the crystal, so the relationship θ and β must be calculated using Snell's law. Considering the effects of refraction the rotation of the crystal with respect to the beam propagation direction is $\beta \approx 35.6^\circ$, which can be tuned by means of a high precision rotational stage, oriented in such a way as to rotate the crystal in a plane parallel to the plane of the optical table. The proximity of the angles for different types of phase matching suggests that both processes most likely occur in parallel, producing a linearly polarised pulse that must be separated from the pulses originally involved in the nonlinear mixing. For the separation of the MIR radiation we use a germanium wafer with low transmission for the NIR pulses (wavelenght below $\approx 1.78\mu m$) and with an inclination given by the Brewster polarisation angle when the polarisation of the MIR radiation is parallel to the plane of the optical table. This configuration, although not optimal for the transmission of the MIR radiation generated at a polarization of approximately 45° with respect to the table plane, was chosen for simplicity and low risk, being possible in the future to install a periscope that rotates the polarization in such a way as to optimize the brewster angle. Under this non-optimized configuration, pulses with energies up to 4.6

μJ of MIR radiation with a diameter of 6 mm were achieved. This energy can be easily decrease by rotating the HWP of the pulse before entering the PBS, given the reduction of signal reflection.

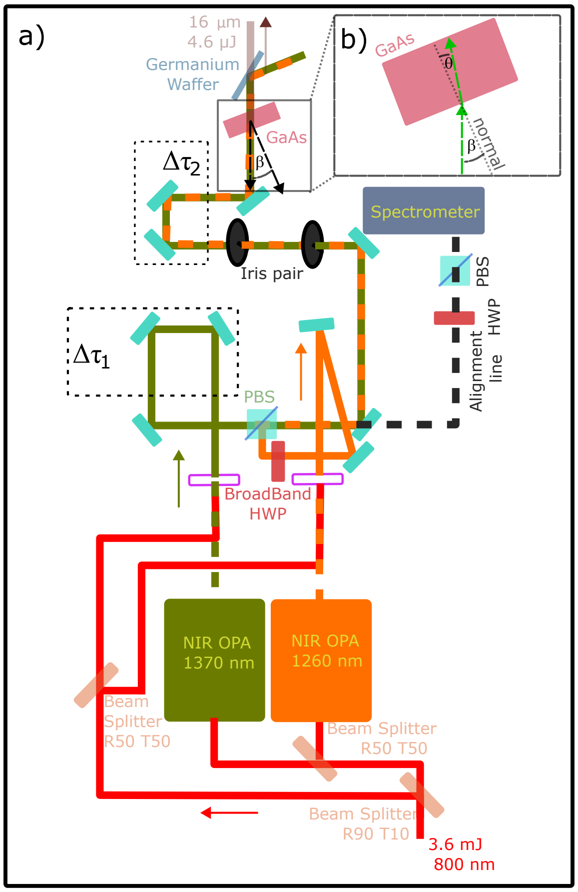

FIGURE 2.15: a) Intense MIR generation using two OPAs with double amplification. PBS is a Polarizer Beam Splitter, HWP is a Half Wave Plate and HWP is a retroreflective that allows to regulate the length of the optical path. The aligment line is a line which, by removing a mirror, allows the beam to be guided to a spectrometer. GaAs is Galium arsenide, and Germanium Waffer is arranged at a brewster angle. All mirrors are of high quality for wavelengths between 1200 and 1400 nm. b) Inset to show the angles involved in the refraction of the beam in the GaAs crystal, where β is the external angle and θ is the internal angle of the beam with respect to the normal.

Chapter 3

Charge injection in semiconductors

In recent decades, optics-based technology has taken over fields traditionally dominated by electronics, such as high-precision time measurement [Hin+13], information transmission [Ben93], or even the development of computer protocols such as quantum computing [NC12]. This remarkable progress in photonics is also opening up new areas of development for electronics, which is adapting and complementing the new technical resources offered by optics. One of the most exploited resources in electronic applications are material junctions and electronic transport, or charge injection from one material to another. In addition to electronic applications, the injection of charge from one material to another has direct consequences also on the optical response of the receiving material, for example by inducing changes in the interaction of optically excited electrons and holes or even by varying the decay time of the excited charges. Both cases mentioned are analysed in this thesis in different types of junctions that favour these effects; in a first instance a semiconductor-metal junction is analysed to study the effect of charge injection on the electron-hole interaction, and in a second instance a semiconductor-semiconductor interface is analysed that allows excited states with longer lifetimes. In this chapter, the theoretical basis of charge injection, semiconductor-metal junction and semiconductor-semiconductor junction is presented, which will allow a deeper understanding of the physical effects described in the following chapters.

3.1 Physics of semiconductors with a majority-carrier concentration

In general, in semiconductors the concentrations of electrons in the conduction band n and holes in the valence band p are equal, given their common origin in an excitation. However, there are strategies that allow conditions where one type of carrier locally has a higher concentration than the other, and which can be used as an additional degree of freedom in electronic devices. Some of these options are: doping of semiconductors with acceptor or donor impurities [SE84], excitation of an electron-hole pair and subsequent application of a voltage that spatially separates the populations [WCW15], or electronic contact between materials that allows transport of electrons and holes between them after optical excitation [Roc08]. Charge injection between different materials, which is dependent on the optical excitation rate, offers the freedom to control the densities of electrons or holes injected into a material without the need for external agents such as voltages, which can have unwanted effects on the physical phenomena under study. The absence of external agents such as voltages and the case-by-case control of the excess carrier density in the receptor material make charge injection preferable to other strategies for studying the effect of excess carriers on diverse physical phenomena in semiconductors. In general, charge injection as presented here is a transient effect that tends towards thermodynamic equilibrium. Therefore, the use of this strategy only makes sense when you want to study dynamic phenomena in short times on the order of a tens to hundreds of picoseconds, depending on the probability of electron-phonon scattering in the system under study.

Under conditions of equal carrier concentration, the rate of recombination of optically excited electron-hole pairs is proportional to the product of the populations of excited electrons and excited holes minus the product of the populations at thermodynamic equilibrium of electrons in the conduction band (n_0) and holes in the valence band (p_0).

$$R = s\left(np - n_0 p_0\right). \tag{3.1}$$

The proportionality coefficient s is inverse to the carriers population lifetime out-of-equilibrium and is a function of the recombination physical mechanisms. These recombination mechanisms include photoluminescence, trap-assisted recombination or Auger recombination, each with different lifetimes and a probability of occurrence given by the geometry of the band structure and the density of excited states.

If after an excitation of the medium one of the carrier concentrations in thermodynamic equilibrium is much higher than the excitation of the other, e.g. $n_0 \gg p$, the effective decay rate is approximated by the expression [GP14],

$$R = sn_0\left(p - p_0\right). \tag{3.2}$$

This approximation has two conceptual consequences: first, the inverse of the excitation lifetime has been scaled by n_0 ($s \rightarrow sn_0$), and second, the excitation density depends only on the minority carrier concentration. Similarly, the absorption probability will be affected in a similar way to the recombination process in the presence of a carrier concentration much larger than a minority carrier concentration. This change in absorption or recombination probability is a consequence of a change in the interaction probability between charge types in the presence of a majority carrier concentration. The probability of interaction is higher between majority carriers, lower between carriers of different classes and much lower between minority carriers. Therefore, effects that depend on the interaction probability between charges may behave differently in situations with an excess of one type of charge compared to a situation with an equal density of charge types. In general, variations in the probability of interaction between charges of the same or different types can lead to variations in the excitation and decay probabilities of certain quantum states, which can modify the absorption spectrum and/or the dynamical constants extracted, for example, by a pump-probe experiment. Examples of quantum states strongly affected by the majority presence of a particular type of charge are collective excitations mediated by Coulomb-type interactions, such as excitons or plasmons. In general, these effects can be widely exploited in various technologies, such as in the design of electronic devices to modulate decay rates [Tom+20], to improve the efficiency of photovoltaic cells [Ava+11] [Roc+94], in the design of optoelectronic devices like transistors [DR55] or in various optical applications whose effects can be modulated by charge injection [EA21].

3.2 Electrical junction

The contact between solids at the electronic level, called electrical junction, involves balancing the electronic chemical potential of the materials. This implies a balance in the Fermi energy between the solids, which can be achieved for materials with different Fermi energies by intra- and inter-material electronic transport. In particular, if the materials have free charges, their electronic transport of charges to balance the chemical potential is called diffusion current. In general, the origin of these free charges can come from dopants, optical excitations or thermally excited charges in equilibrium with the environment. The diffusion current in semiconductors can create a zone of inhomogeneous charge accumulation in the contact zone to achieve chemical equilibrium. This zone of inhomogeneous charge accumulation leads to a difference in electric potential and thus to a spatial deformation of the energy bands. This region with its affected bands is called the depletion region. The electric field generated by the electric potential gradient in the depletion region opposes the diffusion current, thus allowing a state of equilibrium in the electronic transport. Thus the current density is given by [Roc08]

$$J = \mu_n k_b T \frac{dn}{dx} + e\mu_n n E = 0, \tag{3.3}$$

where μ_n is the electro-mobility, k_b is the Boltzman constant, T is the temperature, n is the electron concentration, e is the fundamental electron charge and E is the induced electric field. In general, the equation 3.3 is rewritten by defining a diffusion coefficient $D = d_m u_n k_b T/e$, which takes the form

$$J = eD\frac{dn}{dx} + e\mu_n n E = 0. \tag{3.4}$$

The deformation of the bands involves a potential barrier that inhibits the transit of charges in both directions. The potential barrier ϕ_{bh} has a defined height given by the difference in the Fermi energies of the materials,

$$\phi_{bh} = E_{F1} - E_{F2} \tag{3.5}$$

where E_{F1} and E_{F2} are the Fermi energies of the first and second materials. This deformation, in turn, has a width w, which defines the length of the depletion region, being defined in a simple way only with a high density of free charges, as offered by doped semiconductors and metals. For a contact between two doped semiconductors one n-doped with a donor doping level N_d and the other p-doped with an acceptor doping level N_a, W is given by

$$w = \left[\left(\frac{1}{N_a} + \frac{1}{N_d}\right)\frac{2\epsilon\phi_{bh}}{e}\right]^{1/2}. \tag{3.6}$$

Equivalent for the case of contact of an n-doped semiconductor with a metal

$$w = \left[\left(\frac{1}{N_d}\right)\frac{2\epsilon\phi_{bh}}{e}\right]^{1/2}, \tag{3.7}$$

where ϵ is the permittivity of the semiconductor and which, in the case of two semiconductors, is assumed to be the same for both. Since the depletion region arises due to charge redistribution and the consequent presence of an electric field, for the metal-semiconductor case the deformation of the bands will naturally take place only in the semiconductor, as shown in Fig. 3.1 a). For the two-semiconductor case, the part of the distance W in the p-doped (d_p) and n-doped (d_n) semiconductor is given by $d_p/d_n = N_d/N_a$, as shown in Fig 3.1 b).

Outside the depletion region, the thermodynamic equilibrium of the Fermi energy implies a homogeneous density of free electrons and holes in both constituent materials of the junction which is a function of the barrier height n_{p0}. For example, in a p-n junction, the density of free electrons and holes on the p-semiconductor side is given by

$$n_{p0} = n_{no}e^{-e\phi_{bh}/k_B T} \tag{3.8}$$

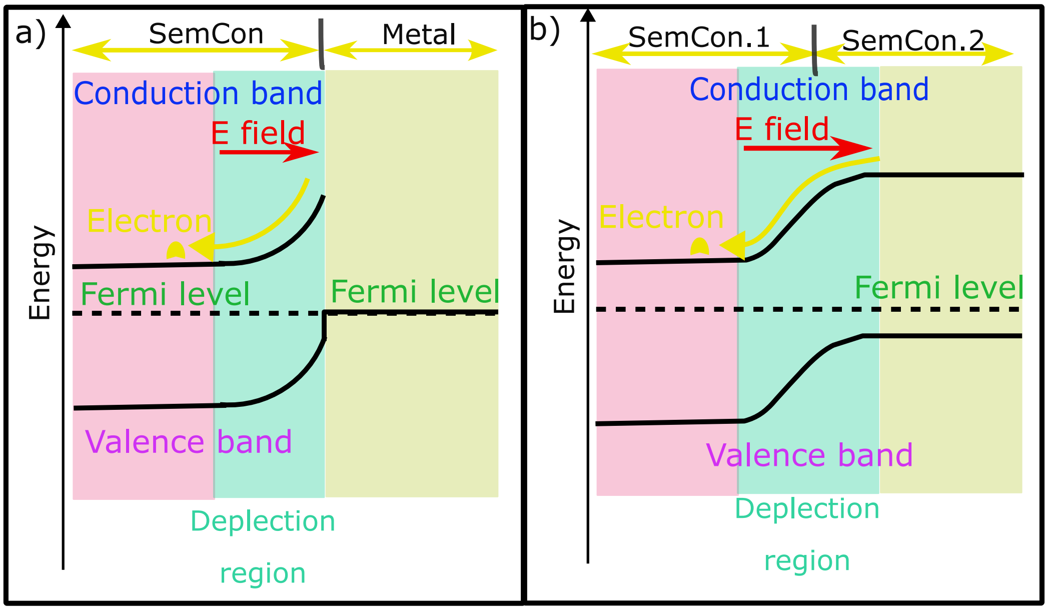

FIGURE 3.1: Deformation of the bands due to electrical contact between materials. The pink and green areas are the unchanged material while the light blue area is the depletion region, which has an associated electric field, which can induce electron movement. In a) shows the semiconductor-metal contact, and where the depletion region takes place only in the semiconductor. For contact between semiconductors the depletion region takes part in both materials, as seen in b).

and

$$p_{p0} = p_{no} e^{e\phi_{bh}/k_B T}, \tag{3.9}$$

where n_{no} and p_{no} are the initial density of free electrons and holes in the n-type semiconductor.

If these contacting materials are subjected to a potential difference V, the potential barrier height will have an additional component, so,

$$\phi_{bh'} = \phi_{bh} - V, \tag{3.10}$$

whith the convention of adjusting the sign of V such that a potential difference is considered positive if the barrier decreases has been followed. Under a potential difference, parameters such as the barrier width ω or the free electron density can be recalculated by replacing ϕ_{bh} by the new effective potential of height $\phi_{bh}\prime$.For instance, given the change in the equilibrium density of electrons resulting from the voltage V,

$$n_p(V) - n_{p0} = \Delta n_p(V) = n_{p0}\left(e^{eV/k_BT} - 1\right), \tag{3.11}$$

suggesting a diffusion-mediated electron current such that

$$J_n(V) = \frac{eD_e n_{p0}}{L_e}\left(e^{eV/k_BT} - 1\right), \tag{3.12}$$

where L_e is the electron diffusion length. The total current must also include a current associated with the holes of the same nature as the 3.12 equation. This voltage dependent current V is called drift current.

3.2.1 p-n Junction

A particularly interesting case in the framework of this thesis is the p-n junction as the basic composition of photovoltaic cells. Thus, our focus will be on photon-illuminated p-n junctions that can generate an electronic excitation in semiconductors, and thus a population of free charges independent of injections or dopants.

In general, a reasonable approximation of the band alignment of two semiconductors is obtained using the Anderson rule [Roc08]. Anderson rules are a simplified model of a junction, neglecting the formation of surface states or surface defects, as well as assuming high electroaffinities in both materials involved in the junction. Under the above conditions, there are some properties that are not affected by the junction, such as the difference in the minimum values of the conduction band energies between the participating materials, and the difference in the maximum values of the valence bands at the contact point. The first property is described mathematically by $\Delta E_c = \chi_2 - \chi_1$, where χ_2 and χ_1 are the electrical affinities of the semiconductors involved. The second property is described as $\Delta E_v = (\chi_2 + E_{g2}) - (\chi_1 + E_{g1})$, where E_{g2} and E_{g1} are the band gaps of the materials. Both properties in the alignment of the bands are shown in Fig. 3.2 a). The shape of the alignment can result in a barrier and an accumulation of free electrons, or a shape similar to the application of a voltage bias, which hinders or facilitates electronic transport between materials. . These forms of alignment are referred to in the literature as "spike-like discontinuity" and "cliff-like discontinuity" and are illustrated in Fig. 3.2 b).

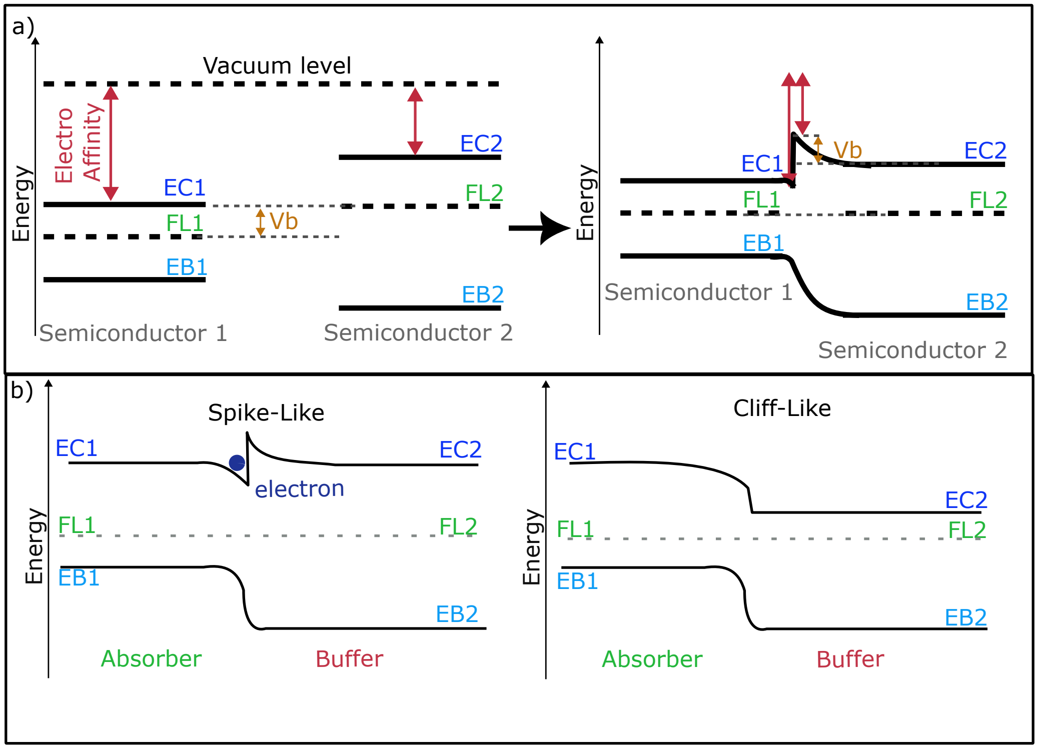

FIGURE 3.2: In a) shows the role of the difference in electroaffinity and the difference between the fermi energies (Vb) in a junction following the Anderson rules. EC is the conduction band energy, FL is the fermi level energy and EB is the valence band energy for materials 1 or 2 as specified. In b) the two possible geometries of junctions between semiconductors are shown, denoting a possible accumulation of electrons for the Spike like case.

The total current in a p-n junction must take into account the sum of the currents in each of its regions, i.e. the doped semiconductors p (J_p), n (J_n) and the depletion region $(J_{p/n})$, plus components that take into account the rate of generation J_G and the recombination of free charges in the semiconductors. In particular, the recombination rate is affected by the junction due to the penetration of free charges into the neighbouring semiconductor. Thus the maximum recombination rate in the depletion region (sub-index D) is given when $n_D = p_D$, so it can be written taking into account 3.1 and 3.11,

$$R_D = \frac{n_D - n_{p0}}{(\tau_n + \tau_p)} = \frac{n_{p0}\left(e^{qV/2k_BT} - 1\right)}{\tau_D}, \tag{3.13}$$

with τ_D is the lifetime of the charges in the depletion region. Assuming this rate over the entire depletion region, the contribution to the total current is given by

$$J_R = -\frac{qwn_{p0}\left(e^{qV/2k_BT} - 1\right)}{\tau_D}, \tag{3.14}$$

where the dependence on voltage is given by an exponential function, and w is the depletion region width. Considering each of the above contributions, and assuming a system excited only once at an initial instant, the system current as a function of voltage is given by

$$J_{tot}(V) = J_p + J_n + J_{p/n} + J_G - \frac{eD_en_{p0}}{L_e}\left(e^{eV/k_BT} - 1\right) - \frac{qwn_{p0}\left(e^{qV/2k_BT} - 1\right)}{\tau_D}. \tag{3.15}$$

The microscopic currents J can be related to the macroscopic currents of the system (I) by integrating over the total contact area (A), assuming that both materials are the same size and that the total area is in contact, thus $I = AJ$. Therefore, in 3.15 the first four terms can be grouped into a general current called the short-circuit current I_{SC} [Gra05], defined as the current at zero voltage. Similarly, given the negative contribution of the currents associated with the voltage, it is possible to find a voltage at which the total current is zero, called the open circuit voltage V_{OC} [Gra05]. In general, the contribution of J_R to J_{tot} can be neglected, unlike the other voltage dependent component. Thus, by grouping $A(eD_en_{p0}/L_e) = I_1$, an expression for V_{OC} is given by

$$V_{OC} = \frac{k_BT}{q} ln\left(\frac{I_{SC} + I_1}{I_1}\right). \tag{3.16}$$

The maximum power of the system will be given by the condition for the voltage

$$\frac{\partial P}{\partial V} = \frac{\partial A J_{tot}(V) V}{\partial V} = 0, \tag{3.17}$$

from which it is possible to extract a $V = V_{mp}$ and $I = I_{mp}$ which marks the limits of the rectangle with the largest possible area within the curve of $I(V)$ v/s V. The degree of proximity of the curve $J_{tot}(V)$ v/s V to the ideal rectangle given by V_{OC} and I_{MP} is given by a coefficient of areas called fill factor FF defined by,

$$FF = \frac{V_{mp} I_{mp}}{V_{OC} I_{SC}}. \tag{3.18}$$

Thus the maximum power can be rewritten as

$$P_{max} = FF V_{OC} I_{SC} \tag{3.19}$$

In fig 3.3 there is a typical curve of $J_{tot}(V)$ v/s V which also illustrates the two rectangles mentioned above, one given by the maximum power and the other the ideal rectangle.

3.2.2 Metal-Semiconductor Junction

One way to describe band alignment for the metal-semiconductor case is by means of the Schottky-Mott rules, which, like the Anderson rules for the p-n junction case, assume the absence of surface states that can induce a Fermi level pinning [Mon90]. The band alignment in semiconductor preserves the difference between the Fermi energy and the lowest conduction band energy, as well as with the highest valence band of the semiconductor, as shown in Fig. 3.4.

The electronic transport of a metal-semiconductor junction differs from that of a p-n junction because the metal is approximated as a free electron gas without the need to be excited. If the metal electrons have enough kinetic energy to cross the potential barrier by tunneling, they are injected into the semiconductor. An approximation which neglects the current due to the tunnel effect is given

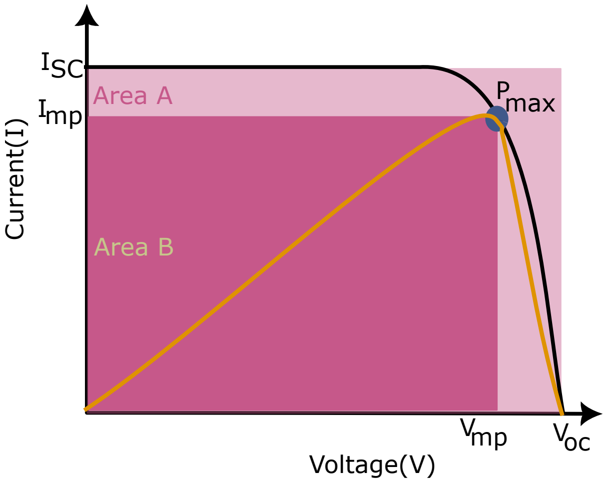

FIGURE 3.3: Current versus voltage graph on a black curve, where the short circuit current (I_{SC}), peak power current (I_{mp}), peak power voltage (I_{mp}) and open circuit voltage (V_{oc}) are marked. In addition, the power curve has been drawn in yellow with the maximum point and the two areas to be compared in order to simplify the interpretation.

by a modified Richardson-Dushman equation [Dus23] for thermoelectric emission or thermal emission of electrons, based on the thermal distribution of electron velocities in metal by means of the Fermi-Dirac distribution. The modified Richardson-Dushman equation in the case of the metal-semiconductor junction assumes the Schottky barrier as the potential barrier to be overcome, giving for the current

$$J_{m/s} = \frac{-em_e k_B T^2}{2\pi^2\hbar^3} e^{(-\phi_{bh}/k_B T)}, \tag{3.20}$$

where m_e is the effective masses of the electrons in the semiconductor and T is the temperature in kelvins.

3.3 Homojunction and heterojunction: Terminology

Band alignment at the contact between two semiconductors can be discontinuous, as in the case of the "spike discontinuity" and the "cliff discontinuity", or perfectly continuous. In the former case, the presence of discontinuities can have

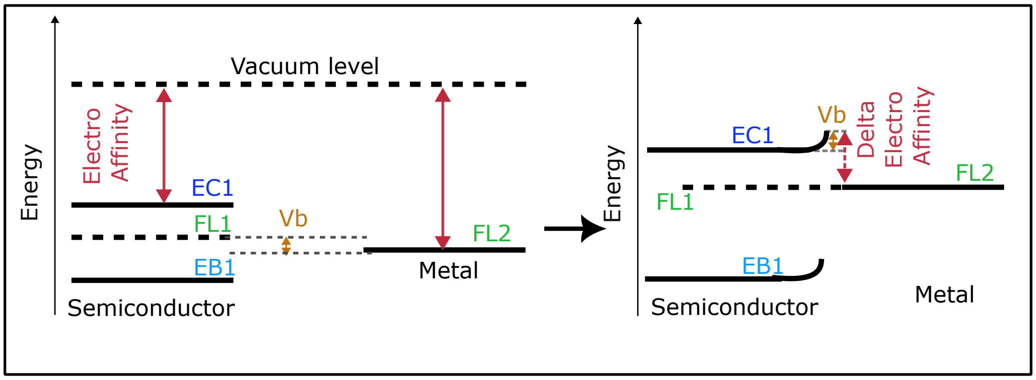

FIGURE 3.4: Shows the role of the difference in electroaffinity and the difference between the fermi energies (Vb) in a metal-semiconductor junction following the Schottky-Mott rules. EC1 is the conduction band energy, FL1 is the fermi level energy and EB1 is the valence band energy for the semiconductor, FL2 is the fermi level energy for the metal and Vb is the potential barrier.

desirable effects by making electron-hole recombination more or less probable at different interfaces, giving rise to the engineering of band alignment. This freedom of band alignment is only possible between materials with different band gaps, so it is natural to distinguish the case of a junction between materials with different or equal band gaps, called heterojunction, which additionally considers the junction of metals with semiconductors, and homojunction. In particular, one type of homojunction is that of a material with itself, but with different doping levels that do not modify the band gap, but where the Fermi energy balance favours the physics of junctions already explained.

Chapter 4

Effects of charge injection in collective excitations in semiconductors

The remarkable success of quantum information protocols in recent years goes hand in hand with increasingly complex and expensive experiments in this field [KN21]. Essential components for quantum information such as single-photon emission and detection, for example, involve in some cases complex and huge experimental schemes to isolate and trap atoms [Col+18]. With a view to mass applications of quantum technologies, one of the avenues the scientific community has explored to reduce costs is the replacement of isolated atoms by collective excitations in condensed matter systems that can play the role of isolated atoms. One of the natural candidates for this role are collective excitations called excitons, which correspond to a particular quantum state of collective behaviour in a condensed matter system with properties similar to a hydrogen atom. In particular, excitonic states have shown considerable robustness in two-dimensional materials such as transition metal dichalcogenides (TMD) semiconductors, making them a platform of great scientific and technological interest. While the replacement of isolated atoms by collective excitations in materials poses a number of challenges in terms of the complexity of solid-state physics, it also opens up the possibility of conveniently exploiting the effects of materials physics, as new degrees of freedom are introduced that are absent in the case of isolated atoms. An example of this degree of freedom is provided by the contact of semiconductors with other materials, making electronic transport between different media possible. Of particular relevance is the contact between TMDs and metals, as established materials of quantum optics and electronics platform. In this chapter, we show how thermionic electronic transport from a metal to the TMD changes the dynamics of exciton formation using a three pulse technique called pump-push-probe. This work, which is one of the pioneering time-resolved studies of the effect of electronic transport on exciton dynamics, shows early temporal effects on the so-called exciton formation dynamics due to the injected charges. In particular, it is shown that these early temporal effects depend on the ratio between the injected electron density and the excited electron density.

4.1 Excitons

The interaction of a semiconductor with electromagnetic radiation with photon energy higher than the band gap of the material causes the excitation of electrons from the valence band to the conduction band and the creation of holes in the valence band. These populations of opposite charges in different bands interact via Coulomb scattering, producing effects such as band gap renormalisation. Other effects of excitation can be derived by resolving the polarisation evolution equation of the medium, given by 2.2, when the λ indices are different. In particular, solving the homogeneous part of the differential equation results in a eigen-state equation given by [KK06]

$$\left[\frac{\hbar^2\mathbf{k}^2}{2\mu} - \sum_{\mathbf{k\prime}} \frac{\mathbf{k}e^2}{(\mathbf{k}-\mathbf{k\prime})^2}\left(n^e_{\mathbf{k\prime}} + n^h_{\mathbf{k\prime}}\right)\right] P_n(\mathbf{k}) \\ - \sum_{\mathbf{k\prime}} \left(1 - n^e_{\mathbf{k\prime}} + -n^h_{\mathbf{k\prime}}\right) \frac{\mathbf{k}e^2}{(\mathbf{k}-\mathbf{k\prime})^2} P_n(\mathbf{k\prime}) = E_n P_n(\mathbf{k}) \quad (4.1)$$

where n^i_k is the population of the particle of type i with a momentum k and μ is the effective mass considering electron and hole. This equation for polarisation, which mixes both electron and hole states, has a form equivalent to a Schrodinger equation in the momentum space of a particle with a Coulomb-like central potential. In this context, this equation is commonly referred to as the Wannier-Mott equation or Wannier equation and, similar to the Schrodinger equation for the Coulomb-like central potential, the solution corresponds to the coupling of $P(\mathbf{k})$ to form a hydrogen atom-like structure called the Wannier exciton. The absence of the second Coulombic interaction term in the equation 4.1, leaving on the left-hand side only the component enclosed in brackets, can be interpreted as the energy equation of free charges, electrons and holes, where the difference is equal to the renormalised band gap of the semiconductor. The Coulomb interaction, by creating a bond, reduces the energy of the system, so the eigenvalues of 4.1 must be less than the energy of the electronic band gap. Mathematically this idea is expressed by equating the eigenvalues of the energy coming from the 4.1 to the difference of the renormalised electronic band gap energy ($E_{g,ren}$) minus the binding energy ($E_{n,b}$) like $E_n = E_{g,ren} - E_{n,b}$. Similar to solving the Schrodinger equation for the hydrogen atom, where one has to take into account the directions in which the wave function can be spread, the Wannier-Mott equation will also depend on the dimensionality of the problem. The values of the binding energy of 4.1 depend on whether the semiconductor is two-dimensional or three-dimensional, with eigenvalues of $E_{n,b} = -E_{g,ren}/n^2$ where $n = 1, 2, ...\infty$ for the three-dimensional case and $E_{n,b} = -4E_{g,ren}/(1 + 2n)^2$ with $n = 0, 1, ...\infty$ for the two-dimensional case, where n plays the role of the principal quantum number. Comparing the two cases, the highest binding energies are obtained in the two-dimensional case for low n. In both cases these energy levels are well discretised for low n, but cluster for high n, obtaining at the edge with the conduction band a continuum of eigenvalues associated with the excitons. Extending the analogy with the Schrodinger equation, other states are possible, such as a trion consisting of two equally charged particles and one of opposite charge, or a biexciton as an attractive interaction between two excitons. Each of these states has different eigenvalues, which are reflected in different lines in the absorption spectrum of a material due to different binding energies. In particular, due to these bound states, a direct bandgap material will show absorption lines with energies below the optical bandgap and can be identified as collective excitations due to the Coulombic interaction.

Since the terms behind renormalisation and the electron-hole interaction are coulombic in nature, the strict separation of these effects, as proposed, is only valid for very low electron and hole densities. As the charge densities increase, screening effects must be taken into account, which weaken the electron-hole interaction reducing the binding energy of an exciton. This reduction in binding energy due to charge density goes so far as to reduce this energy to zero, eliminating the possibility of forming excitons [Che+15]. A material with a charge density level such that it does not allow exciton formation will be referred to by us as a "no exciton phase". In the literature, this effect of no exciton formation can be referred to as Mott transition, in analogy to the metal-non-metal transition effect described by Mott [MOT68], which in our case involves an evolution from a system with bound states to a system with all free electronic states. However, the use of this term neglects the nature of the long-range ordering of the electronic states, which is fundamental to the theory described by Mott [Kho14], and is therefore generally a misleading and incorrect use of terminology in this context. Experimentally the excitation of the system to a density where the "no exciton phase" takes place can be identified by the disappearance of the exciton-associated absorption line in the absorption spectrum of the semiconductor [Bec14]. Therefore, any optical study of excitons must demonstrate that the exciton-associated absorption line is present not reaching the "no exciton phase".

Although the electron-hole interaction can potentially be solved by forming excitons, excitons can be unstable due to state-perturbing interactions. Strictly speaking, the condition for an exciton is that there is a strong correlation in the population density of excited electrons and holes in real space. In general, during the excitation and driving of charges by an electromagnetic field, and the resulting scattering of charges, the spatial correlation of the populations is not very high. This correlation becomes relevant when the polarisation dynamics decays to equilibrium some time after excitation. In this way it is possible to distinguish two dynamic processes of different nature with respect to the excitonic states. The first period is governed by the polarisation evolution in the density matrix of the medium and is called the exciton formation process, with a maximum duration of a few picoseconds for a pulse excitation of hundreds of femtoseconds [KK06]. The second period is determined by the evolution of the correlation function between the two particles, electron and hole, affected by the environment and the photoemission, called exciton dynamics, whose duration is the lifetime of this state, which is usually in the range of hundreds of femtoseconds to nanoseconds. These dynamics depend on the recombination mechanism and the temperature of the system [ATB91].

As mentioned in the derivation of 2.2, the spin component was not considered for simplicity. By correcting this fact, new components appear in 4.1, adding a spin dependent component which can be worked out by perturbations and which slightly changes the calculated energy eigenvalues describing exciton transitions with circularly polarised light. This spin-dependent term can be used by spintronics in technological applications of excitons and the interaction of semiconductors with photons.

4.2 Transition Metal Dichalcogenides

The use of excitons as a platform for quantum optical protocols depends on the robustness of these quantum states, and it is also desirable to be able to excite these states optically at wavelengths that are easy to obtain and work like the visible range. A bound state immersed in a thermal bath is said to be robust if its binding energy is higher than the average energy of the bath. Due to the wavefunction confinement offered by two-dimensional semiconductor media, semiconductor layers often achieve higher binding energies than three-dimensional semiconductor media, and thus exhibit greater robustness. Excitons formed in a layered semiconductor TMD have been shown to be robust at room temperature, with lifetimes of hundreds of picoseconds under these conditions [Rob+16]. Particularly high binding energies are achieved in conditions of a few TMD layers, each of which is one atom thick [CLZ15], allowing even in multi-layer systems a thickness less than the Bohr radius of an exciton, which is significant as a two-dimensional material. This fact theoretically justifies the observation that in absorption spectra measurements of these materials, the amplitudes of absorption lines associated with excitons are comparable to the amplitudes of absorption lines of unbound states. A particularly interesting group of two-dimensional materials, due to their weak van der Waals bonding between layers, which makes it easy to isolate a few layers by exfoliation [DR19], and a general band gap in the visible to near-infrared range, are the transition metal dichalcogenides (TMDs) [DR19]. TMDs have a chemical composition of a transition metal, Mo or W, and two equal elements of the chalcogen group, S, Se and Te. The excitons in these materials have a binding energy that is generally quite high compared to the average energy of the thermal distribution of phonons at room temperature, typically in the hundreds of meV up to about 1 eV [Sar20]. These binding energies are superior to other widely studied media such as GaSe with a binding energy of about 30 meV [Wei+16] or ZnO with about 60 meV [Yı22]. The strong spin-orbit coupling offered by TMDs generates a non-negligible valence band splitting effect at the K-point of the Brillouin zone.This gives rise to excitonic states with different energy gaps and binding energies, with the lowest gap state called the A exciton and the highest called B exciton [Mak+10]. This coexistence of spin-state sensitive excitons has attracted much research in the field of inter-valley spintronics, called valleytronics, which uses spin as a degree of freedom in its quantum information protocols [Sch+16]. With different binding energies associated, other collective excitations and quasiparticles have also been observed in these materials, such as charged excitons, biexcitons and, in the case of multilayers, excitons composed of charges in different layers called interlayer exciton [Sar20].In addition to the latter effect, adding new layers changes the macroscopic properties of the system, such as increased photon absorption or changes in conductivity, making these media attractive for different applications. A system that increases its thickness by adding new layers can no longer be considered fully two-dimensional, and a few-layer system must be distinguished from a bulk system. A few-layer system is defined as a system whose maximum thickness is comparable to the excitonic Bohr radius, meaning that the electronic wave function must still be considered as confined. WS_2 for example can be considered as a few-layer system if it has less than 5 layers , otherwise the system must be considered as a bulk system [Che+14]. In particular this material has an excitonic binding energy higher than that associated with room temperature even in its bulk form [Che+14].

4.3 WS_2/gold system

In an interface system between materials, it is possible to induce charge carrier transport between them. This injection of charged particles or quasiparticles into a material can, with sufficient density, affect the interaction between electrons and holes, thereby changing the recombination time of charged particles and the formation mechanisms and dynamics of collective excitations. To simplify the analysis of the effects of charge injection on a material and to allow external control of the injected carrier density, it is advisable to use simple injection mechanisms that do not depend on many physical parameters. One of the simplest mechanisms to understand and model for charge injection between materials comes from Schottky barrier theory, which assumes the absence of Fermi level pinning. In particular, the interface of TMDs with metals has shown a good approximation to the ideal Schottky barrier case, especially when the TMD is directly exfoliated on the metal [LCF87].

For the study of how the dynamics of exciton formation is affected by the injection of charged particles, a sample with a multilayered WS2 interface directly exfoliated in gold was prepared. Measuring the absorption spectrum of the sample shows an absorption line with a wavelength of 618 nm, marked by a red arrow in Fig. 4.1 a), which is attributable to the exciton at the K-point of the Brillouin zone. At such conductor-semiconductor interfaces, the excitation and subsequent dynamics of the electron-hole pair in the semiconductor can be affected by the electrostatic response of the metal, modelled, for example, by the formation of image charges, which are less sensitive the bigger the distance between the electron-hole pair and the metal. In particular, the disappearance of absorption lines attributable to excitons has been observed in monolayers of insulators, but they reappear as more layers are added [Dut+05]. This implies that, in general, for the study of two-dimensional semiconductors in contact with metals, at least a minimum number of layers is required to neglect this effect. The thickness of the semiconductor in the sample used was determined from the resonance of the etalon formed with the metal layer,which shows a prominent reduction of the reflection around 720 nm, marked with a brown arrow in Fig. 4.1 a), so that its width can be estimated to be around 20 nm according to the model presented in [Zha+20]. This model shows different behaviours in the exciton resonance profile for semiconductor widths smaller and larger than 15 nm, showing a width-dependent binding energy for widths smaller than 15 nm, and width-independent for larger widths. The independence of the wavelength of the exciton resonance with respect to the width of the TMD is evidence that the redistribution of the electric field in the semiconductor due to the presence of the metal is negligible, and therefore a width larger than 15 nm is desirable for our sample. The sample under consideration has a width of 20 nm, being considered as a bulk with an A exciton binding energy of 50 meV [Che+14], allowing the formation of excitons at room temperature.

For the metallic substrate, gold was used due to its high work function of 5.1 eV, which is higher than the WS_2 electroaffinity of about 4 eV [Dur+18], favouring the electronic injection from the gold into the semiconductor and generating a Schottky barrier height of about 1 eV, as schematically shown in Fig. 4.1 b).

4.3.1 Reference sample WS_2/SiO_2

To distinguish effects caused by charge injection from the effects of WS_2, a sample with negligible probability of charge injection from or into WS_2 is prepared. For this purpose, a WS_2 bulk sample with an estimated width of hundreds of nanometres is deposited on a SiO_2 substrate. The WS_2/SiO_2 sample has a strong dip in the transmission spectrum at the 630 nm wavelength associated with the exciton absorption, which is marked with a light red arrow in Fig. 4.1 a). The excitonic absorption line of the WS_2/Au sample is slightly blue-shifted with respect to the exciton absorption line of the WS_2/SiO_2 sample. This shift can be attributed to the screening induced by the gold, which is consistent with the results shown in [Par+18] . The SiO_2 has an electroaffinity of 0.75 eV and a band gap of 8.95 eV [Fuj+16], which results in a spatial band bending in the valence and conduction bands close to the interfase that favours the transport of excited electrons and holes respectively from the insulator to the semiconductor, as seen in Fig. 4.1 c).

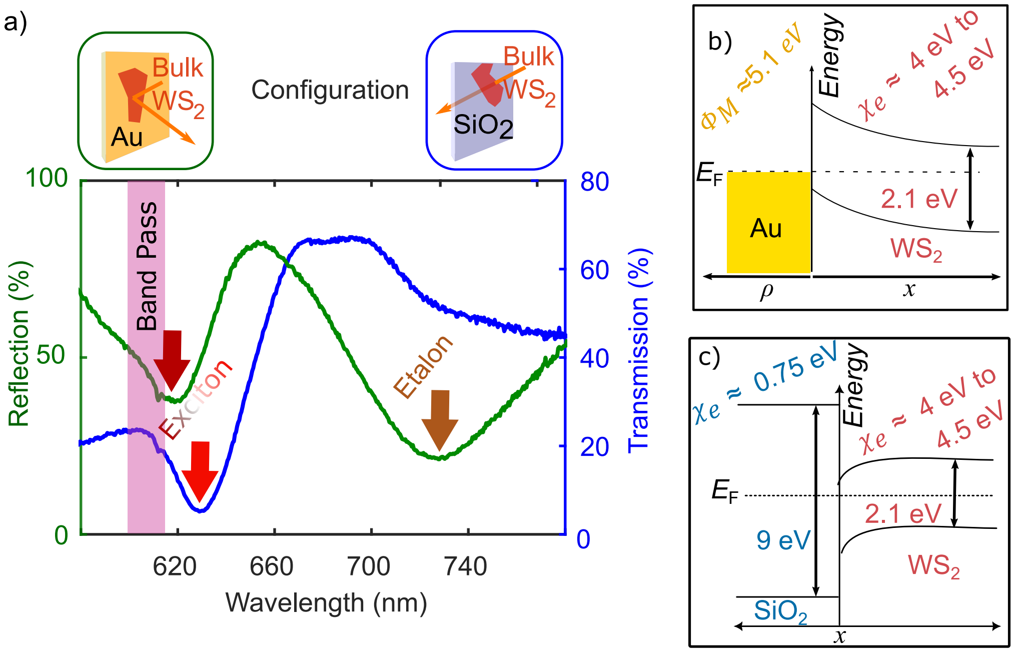

FIGURE 4.1: a) Reflection and transmission spectra for the WS_2 sample exfoliated in gold (green) and in SiO_2 (blue) respectively. The figure shows with arrows the components with higher absorption associated to the exciton in both cases, as well as the case of the etalon for the reflection measurement. b) Thermal Fermi-Dirac distribution (ρ) of gold and band alignment in WS_2 at WS_2/gold interface with approximate values for the work function in gold (ϕ_M) and the electron affinity (χ_e) in WS2. c) Band alignment in WS_2 at WS_2/SiO_2 interface with approximate value for the electron affinities in both materials.

4.4 Experimental setup and results

To study the effect of charge injection on the dynamics of exciton formation in WS_2, two requirements must be met. First, it is necessary to control charge injection and excitation in the semiconductor independently and in a manner that is compatible with a pump probe scheme. Secondly, to maximise the interaction of the excited electrons and holes with the injected electrons, a high density of each of these species is required. Regarding the first point, and considering the theory of thermionic electron injection between a metal layer and a semiconductor, electron injection can be thermally enhanced if a portion of the Fermi-Dirac thermal distribution of the electrons has an energy higher than the SBH. Increasing the electronic temperature of a medium can be done optically, with ultrashort pulses being ideal for high temperatures. Since the origin of the change in electronic temperature is based on the conversion of the energy density of a pulse into thermal energy associated with the random collision of electrons driven by the electric field of the pulse, this effect depends only on the fluence of the photons and is independent of their wavelength. Consequently, the interaction of the WS_2/gold system with a pulse coming from the semiconductor face will have different effects depending on the wavelength of the pulse photons: If the pulse consists of photons with an energy lower than that of any optical excitation in the TMD, it will ideally only raise the temperature of the electrons in the metal, allowing the injection of electrons into WS_2 for sufficiently high pulse fluences. On the other hand, if the pulse is composed of photons with energy greater than or equal to that required to excite the conduction band electrons in the TMD, part of the pulse energy will be absorbed, initiating the exciton formation process, while the remaining energy will thermally excite the electrons in the metal. In this way, by using two pulses, one with sufficient energy to excite electrons in the conduction band of the TMD and another with energy below band gap, it is possible to excite the system by controlling the density of excited and injected electrons in WS_2 with some independence as shown in the Fig. 4.2. For the sake of simplicity, in order to refer separately to each of these two pulses involved in the excitation of the system, we will call the pulse with the lowest energy Pump and the pulse with the highest energy Push. With regard to the second point of the proposed two-pulse system, the electron-hole pair density depends only on the fluence of the push, which in general must be high, taking care not to reach the above-mentioned "no exciton phase" or other non-linear effects. Similarly, since the pump is transmitted by WS_2, the contribution of two-photon absorption in the material, which favours electron excitations, must be negligible to preserve the independence of the origin of the excited and injected electrons. This condition sets a maximum fluence limit for the pump, as in the previous case.

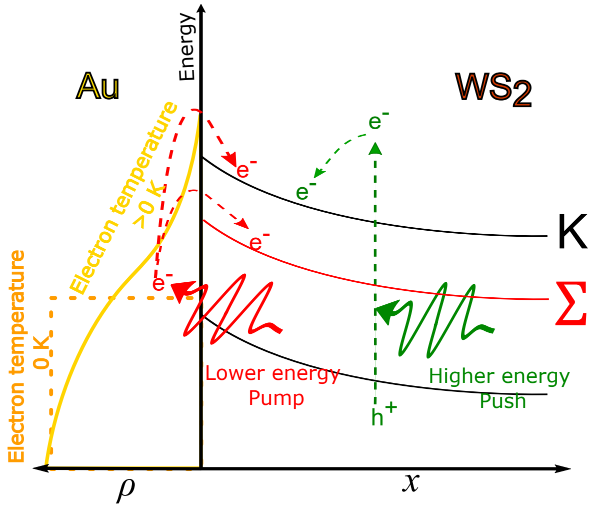

FIGURE 4.2: Schematic representing the thermionic injection of electrons from gold into WS_2 due to a lower energy pulse called Pump and the excitation of the electron-hole pair in the semiconductor due to the action of the higher energy pulse called Push. ρ is the fermi dirac distribution for different electron temperatures in gold due to the action of pump. Additionally, the Σ and K levels where the injection can take place have been plotted.

This experiment was performed using a Yb:KGW Laser (PHAROS laser-Light Conversion) with a fundamental pulse centred at 1030 nm, a duration of 220 fs and a repetition rate of 100 kHz. This choice was made for simplicity, given a second harmonic centred at 515 nm and 160 fs, which can directly excite electrons through the WS2 optical bandgap and thus act as a push pulse, while the photon energy of the fundamental is insufficient to directly excite carriers in the semiconductor and thus could serve as a pump pulse. To find the optimal values of the fluences for both pulses, two experiments are performed independently on the WS_2/gold sample. In the first experiment, the sample is excited using only pulses centred at 515 nm with different fluences, and the transient change in the reflection of a white light probe pulse over a range of wavelengths associated with A exciton is measured. Fig. 4.3a) shows the normalised curves of this pump-probe experiment of the transient reflection measured after a band-pass centered at 610 nm with a spectral width of 10 nm.For times longer than 1 ps, normalised curves with plateaus at different levels reveal a non-linear dependence with the fluence, having a linear dependence with a fluence up to 230 $\mu J/cm^2$. In Fig. 4.3b) the transient reflection has been spectrally resolved using a spectrometer taking the difference of the reflection of the probe with an excited and unexcited sample, generated for the case of a fluence of 200 $\mu J/cm^2$. The possibility of using a spectrometer is only possible because the pump induced variation is close to the order of 1% and does not require such a high sensitivity. These measurements show that for a pumping fluence of 200 uJ there is no transient dissociation of exciton A [KI21], suggesting that the excited charge density is not high enough to reach a "no exciton phase".

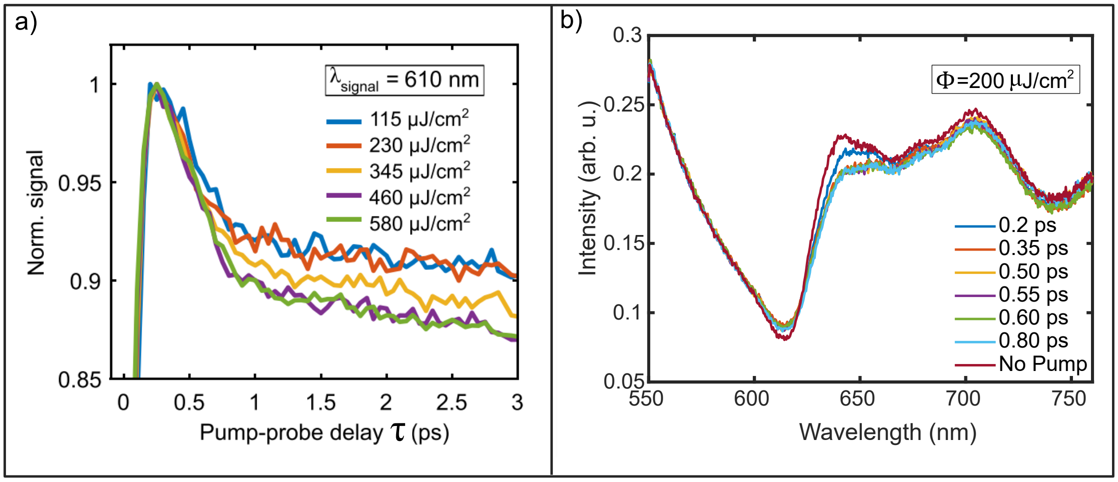

FIGURE 4.3: a) Normalised response of the transient reflection at 610 nm with different fluence in the Push on gold. b) Response of the spectral reflection with different delays between the Push and Probe with a Push fluence at $200\mu J/cm^2$.

In the second experiment, the sample is excited using only pulses centred at 1030 nm with different fluences, and the transient change in reflection of a probe pulse of white light over a range of wavelengths associated with exciton A is measured. Fig. 4.4 shows the .the transient reflection for different pump fluences. Each curve clearly shows a plateau at different levels for longer times, while for times shorter than 0.3 ps a linear growth up to the plateau is observed. The level of transient reflection at the plateau increases linearly with fluence, ruling out non-linear effects, and this change is therefore attributed to a linear thermal response of the system.

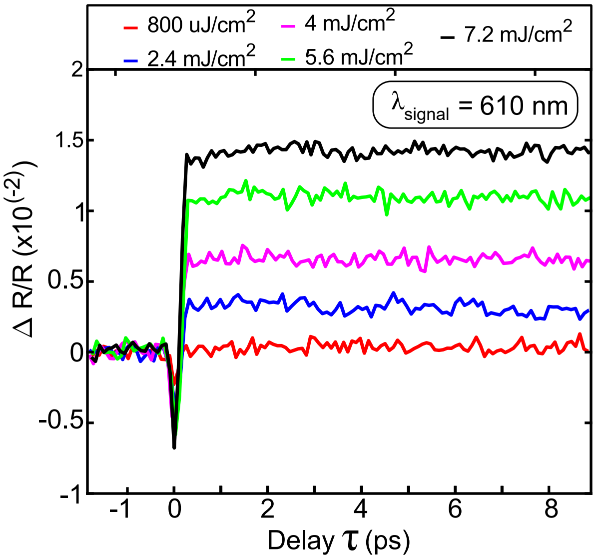

FIGURE 4.4: Response of the transient reflection in WS_2/Au at 610 nm with different fluence in the pump pulse centred at 1030 nm.

The Fig 4.5 shows the conceptual scheme for three pulses. The pump and push have a relative delay between them, called T, and cause an injection and excitation of charges respectively. A third white light pulse, delayed by τ with respect to the push, probes the transient changes in the optical properties of the material. Similar to the usual pump-probe scheme, the excitation must be modulated in order to exploit the increased sensitivity of lock-in detection. According to the theory [Bat89], a high density of injected and free charges in the conduction band of a semiconductor can cause metallisation of the optical response of the material, inducing an increase in the wavelength independent reflectivity. As can be seen in 4.3 b) the reflectance response compared to a case without pump, brown curve, is different only in certain spectral regions, ruling out the above effect. The latter also suggests that the linear effect measured in 4.4 is specific to the exciton-associated frequency band, reinforcing the hypothesis of an effect of the injected charges on exciton formation. To avoid mixing in the analysis of other possible responses due to the injection of charges not associated with an interaction between injected and excited charges, the pump pulse centred at 1030 nm must have the same repetition frequency as the probe, while the push pulse centred at 515 nm is the one that is modulated.

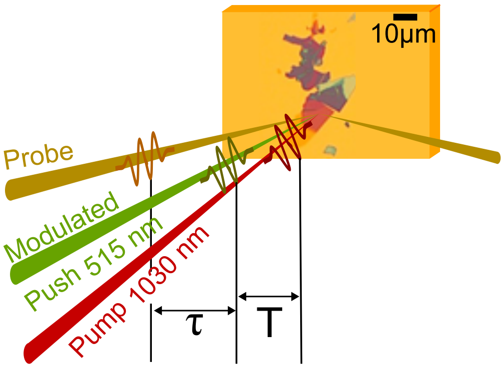

FIGURE 4.5: Scheme of the Pump-Push-Probe experiment (PPP). T is a static time delay between Push and Pump. τ is the delay time between Push and Probe and varies continuously throughout the experiment. Push is a signal modulated at half the repetition rate of the Probe and Pump.

Consistent with the use of a reference sample with no possibility of charge injection into WS_2, such as the WS_2/SiO_2 interface sample in a PPP experiment, to distinguish injection effects from other WS_2 phenomena, it is also necessary to confirm that the response of a pump-push excitation in the gold sample is distinguishable from the WS_2/gold injection effects. For this purpose, the transient reflection of a probe at a wavelength of 610 nm was measured on a pure gold sample and on a WS_2/gold sample in a PPP experiment with a relative delay between pump and push of 0 fs. The results of the transient reflection are shown in fig. 4.6, where the orange curve is the one measured on gold and the red one on the WS_2/gold interface. In order to have a scale that makes it possible to illustrate the importance of the effect of the transient reflection of gold in this type of experiment, we have added to the curves previously mentioned in Fig.4.6 the curve (green) of the transient reflection response of WS_2 without the pump pulse, i.e. without a significant contribution of charge injection. The difference in the normalised transient reflection $\Delta R/R$ between the green and red curves for times longer than 1 ps is about $1 \cdot 10^{-2}$, while in the same interval the gold response has a normalised transient reflection of $1 \cdot 10^{-4}$. The fact that the transient reflection response of gold is two orders of magnitude smaller than the difference between the transient reflection response curves for WS_2 with strong and negligible injection suggests that while there is a component in the transient reflection due to the response of the metal alone, the difference is primarily due to an interface effect such as electronic injection.

The degrees of freedom that the Pump-Push Probe experiment allows are the variation of the relative delay between Pump and Push, which is related to the time between injection and excitation, and the fluence of the pulses to change the density of injected and excited charges independently. Due to the thermal relaxation of the electronic state in the metal, varying the relative delay between Pump and Push is capable to induce the excitation of electron-hole pairs in the semiconductor under different conditions in the electron injection rate in WS_2 as well as with a different density of previously injected electrons. Fig.4.7 a) shows the transient transmission curve over WS_2/SiO_2 for different T, with a fluence of 1.7mJ$/cm^2$ for the pump, 200 μJ$/cm^2$ for the push and 20 μJ$/cm^2$ for the probe. Although these fluence values are relatively high for pump-probe experiments, they allow the signal-to-noise ratio to be increased without introducing higher order effects in the material. The maximum signal amplitudes of the PPP curves for different delays T exhibit a minor offset with respect to each other, which causes a variation of the extracted time constant for the decay of the transient reflection signal of $< 10\%$ between the the case T= 0 ps and T= 0.2 ps. For delays $\tau > 0.5$ ps the curves are identical with constant offset thermally induced by the pump equal to $0.4 \cdot 10^{-2}$ with respect to the measurement without pump (black). For the case with charge injection in the TMD, for the times $\tau > 0.5 ps$

plotted in Fig. 4.7, it shows a similar behaviour to the case without injection, except for a new offset equal to $0.5 \cdot 10^{-2}$. On the other hand the maximum of the transient curves is significantly higher for T = 0 ps and T = 0.1 ps then the maximum of the no pump case (black) curve. This difference in the peak amplitude of the transient signal can not be attributed to a coherent artifact as it is not observed with the WS2/SiO2 sample under the same conditions. Furthermore the extracted time constant of the fast decay varies by more than 80% between the case T = 0 ps and T = 0.2 ps.

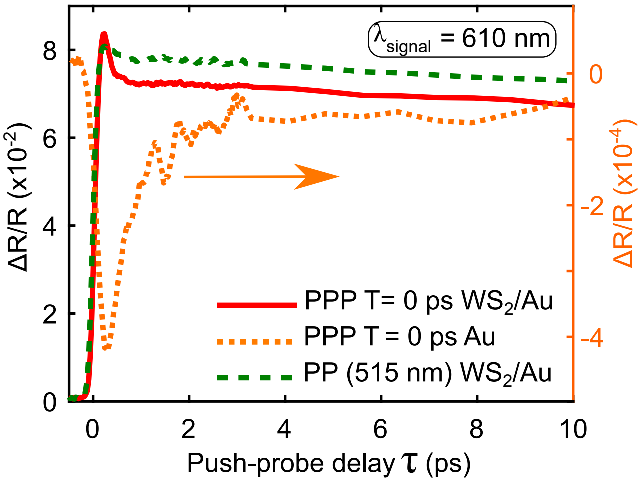

FIGURE 4.6: Result of the transient reflection in a PPP type experiment with T= 0 ps with a fluence for the Pump= 1.7 mJ/cm^2 and for the Push=200 μJ/cm^2 on a WS_2/Au system, red curve, and on the gold sample, orange dotted curve. The orange curve has its Y-axis on the right-hand side in order to scale the effects. Additionally, the case where the Pump at 1030 nm is blocked in the experiment is added, called PP(515 nm) with the green curve.

The fast attenuation of the effect of charge injection on the dynamics of exciton formation by increasing T in steps of hundreds of femtoseconds can be understood by the dynamics of the injected charges in the TMD. Due to the migration of the electron population from the minimum of the conduction band at the K point to the minimum at the Σ point of the Brilloiun zone in WS_2 in only tens of fs[Pup17], the electron population at the K point of momentum space is directly related to the instantaneous thermal state of the electrons in the metal.

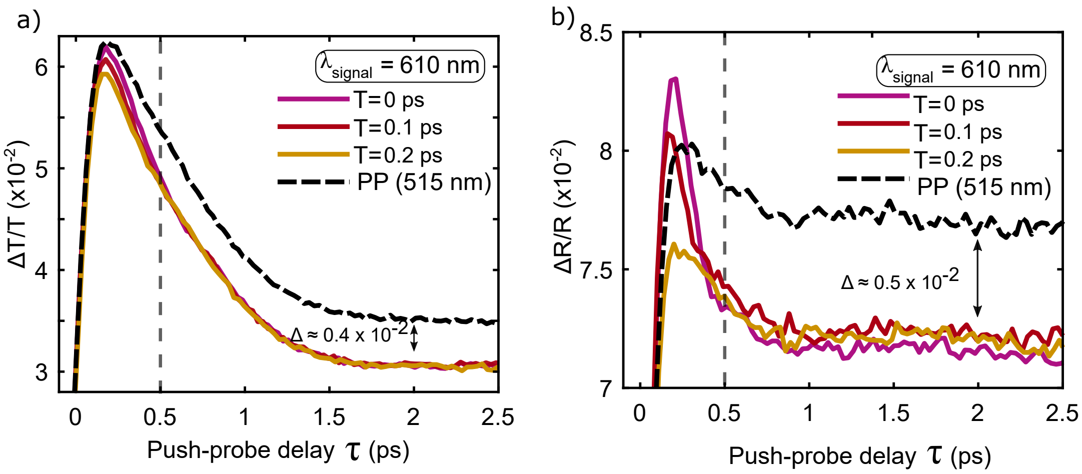

FIGURE 4.7: Result of the transient response in a PPP type experiment varying T with a fluence for the Pump= 1.2 mJ/cm^2 and for the Thrust=200 μ J/cm^2 in a) system WS_2/SiO_2, measured in transmissivity (T) and b) system WS_2/Au measured in reflection (R). In both cases, in addition, the black curve with dotted lines where the pump (1030 nm) is blocked, called PP(515 nm), was added.

This suggests that a strong effect of injection on the ultrafast dynamics in WS_2 results when injected and excited charges have similar momentum, which is for example the case when charges interact via Pauli exclusion.

In order to further investigate the effect of interaction between injected and excited charges, the density of the two populations is varied in the following measurements by changing the fluence of Pump and Push. Fig. 4.8 a) shows the transient reflection curves for different pump fluences and a fixed push fluence of 200 μJ/cm^2 for a relative delay T=0.1 ps. The maximum signal amplitude is independent of the Pump fluence, suggesting that the overall peak effect depends mainly on the excited electron-hole pair densities. The variation of the pump fluence modifies the plateau level and apparently also the decay time of the curves from maximum to plateau. To analyse the behaviour of the decay time of the curves with respect to the variation of the pump fluence, the curves were fitted with a simple exponential model given by

$$y(t) = A \cdot exp\left(-1 \cdot \frac{t-t_0}{\tau_c}\right) + B, \tag{4.2}$$

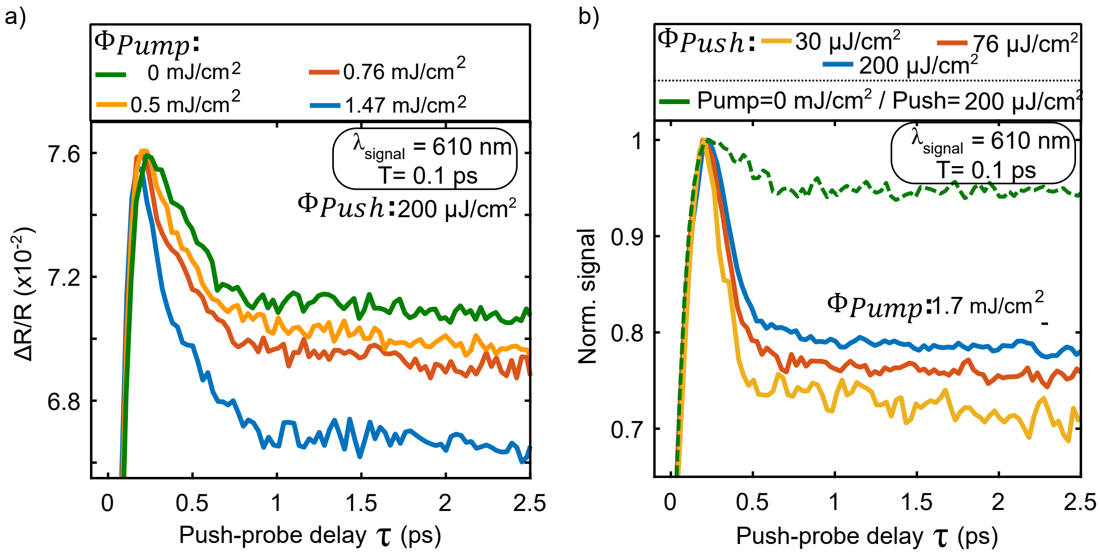

FIGURE 4.8: Result of the transient reflection in a PPP experiment with T=0.1 ps with a) varying fluence for the Pump and a constant Push fluence of 200 μ J/cm^2 ,and b) varying Push fluence and a fixed pump fluence of 1.7 mJ/cm^2, where additionally a curve (green) of a measurement without pump and with fluence push = 200μJ is added. Additionally in b) all curves were normalised with respect to their maximum.

between the times 0.2 and 2.5 ps, allowing to extract the time constant τ_c in each curve.

The variation of the extracted time constant as a function of the variation of the pump fluence is tabulated in the first row of Table 4.1, where the first value of the time constant ($\tau_c(1)$) is associated with the first value of the pump fluence, and similarly with the second time constant ($\tau_c(2)$). Defining the percentage change of the time constant with respect to the first extracted value as $(\tau_c(2) - \tau_c(1))/\tau_c(1) \cdot 100$, it is possible to quantify the reduction of the time constant, which in this case is 18%, as shown in the fourth column of the table. Considering the injected charges due to the pump as a perturbation to the simply excited case, it is natural to want to quantify the effect of these injected charges on the time constant of the no-pump case ($\tau_{c,noPump}$), whose specifications are shown in the third row in green. Comparing these quantities using

$(\tau_c(2) - \tau_c(1))/\tau_{c,noPump} \cdot 100$, we can see that the time constant $\tau_c(2)$ is 18 % further away than $\tau_c(1)$ with respect to $\tau_{c,noPump}$. By varying the push fluence at a constant pump fluence of 1.7 mJ$/cm^2$, a normalised transient reflection can be measured and plotted as shown in Fig. 4.8 b). Since the maximum amplitude of the signal depends on the strength of the push pulse, it is necessary to normalise it in order to better compare the dynamics. Qualitatively, it can be seen that the normalised curves show a lower plateau level as the push fluence decreases. For a quantitative analysis, the time constants of these curves can be analysed in a similar way to the previous case and these results are presented in Table 4.1. In this case, the time constant becomes larger as the push increases, while becoming 25% closer to the time constant of the no-pump situation. Defining a ratio of pump and push fluence, or in other words injected and excited charge density $R_n = n_{injected}/n_{excited}$, the results of both experiments, varying the pump and push fluence, are in agreement [RRA+22]. The greater the contribution of the injected charges relative to the excited ones, faster is the initial decay and lower the plateau level. It is therefore natural that if in Fig. 4.8 b) the curve without pump injection is added, it has its plateau at the highest level and with slow decay dynamics. This consistency for all measurements at different pump and push fluences, after excluding non-linear effects in the medium, proves that charge injection affects the exciton formation process, at least in TMDs, and that it should be tested in the future for other materials with different physical properties, such as dimensionality. The nature of this effect is most likely mediated by scattering between excited and injected carriers at the same point in momentum space, and it should be tested whether currently available theoretical models predict this behaviour. This effect induced by the injected charges on the transient reflection response at the resonance frequency with the energy levels associated with the excitonic state can most likely be analysed from a perturbative approach, where the perturbation should be a function of the proposed ratio $R_n = n_{injected}/n_{excited}$ [RRA+22].

TABLE 4.1: The time constants extracted by an exponential model given by equation 4.2 of the curves in Fig.4.8, varying the pump fluence, in the first row, and Fig.4.8 b), varying the push fluence, in the second row, are recorded. In addition, we have added the information of a case without pump in green colour in the third row, which serves as a parameter of comparison. All curves were measured on WS2/Au samples with a T=0.1 ps. Column 4 gives the percentage change in time constant as a function of the varied parameter relative to the first time constant value tabulated in column 3. Column 5 calculates how much closer or further away the change in time constant calculated in column 4 is from the time constant of the case without pump, as a percentage, being negative if the case is further away and positive if it is closer. The entries N.A. indicate that this comparison does not apply to this case.

Pump fluence (mJ/cm^2)	Push fluence ($\mu J/cm^2$)	Time constant (fs)	% Change time constant	% Comparison no Pump
0.5-1.47	200	309-252	-18	-17
1.7	30-200	147-184	25	11
0	200	324	N.A.	N.A.

Chapter 5

Effects of charge injection on the life-time of electrons and holes in a CIGS Solar Cell with buffer layers.

In the field of photovoltaic (PV) cells, a family of materials of great interest are thin films of $Cu(In,Ga)Se_2$ (CIGS), because their efficiencies are comparable to the most widely used commercially available cells based on silicon monocrystals [AEA22], while their production costs are lower. Although these cell families have lower efficiencies than the leading cells in the field, such as GaAs-based cells [Xia+21], they have certain advantages over them. GaAs cells have two critical downsides that need to be considered: Ga is not very abundant on Earth, so production costs are becoming increasingly high, and As is a very toxic compound. Although CIGS also contains Ga in its composition, other new Ga-free technologies have been developed based on the same principles, such as the thin-film alloy $CuIn(S,Se)_2$, which has achieved even higher efficiencies than CIGS [Kat+19].

To optimise the efficiency of a photovoltaic cell, a p-n heterojunction is often formed to extend the lifetime of the excited charges. The semiconductor in electronic contact with the photovoltaic cell is called the buffer layer, which, due to the junction geometry, receives charges excited from the absorber and thus inhibits early charge recombination. Although buffer layers are not part of the crystals and can therefore be easily replaced, the buffer layer used to achieve the highest efficiencies in CIGS is CdS, which, like As, is toxic and polluting. In this sense, the search for buffer layers free of toxic compounds but with high CIGS contact efficiency is crucial for the development of these and similar cells. Among the buffers that the community considers most successful in contact with CIGS are the aforementioned CdS, Zn(O,S) alloy and In_2S_3 [Sie04].

One of the most important characteristics for determining the efficiency of a thin-film solar cell is the electronic mobility of the excited charges. This characteristic depends on parameters such as the density of excited charges and the instantaneous conductivity, which is a function of the effective mass, being these parameters time-dependent. Many articles on the subject neglect the role of the time-dependent effective mass, and there is no exhaustive time-dependent analysis of this property in CIGS cells, let alone how it is affected by the presence of a buffer. In this chapter, we present two complementary experimental set-ups to independently determine the time-dependent conductivity of the medium and the recombination rate of the excited charges. These complementary measurements allow us to establish the physical origin of the measured mobility, and the role of the effective mass in the efficiency of the cells. In particular, this chapter proposes to determine the mobility for the systems CIGS-CdS, CIGS-Zn(O,S), CIGS-In_2S_3 and CIGS alone, the former being the most successful buffers in contact with a CIGS and the latter being a reference measurement allowing to discriminate junction-specific effects on the mobility and charge injection.

5.1 CIGS

Like most absorber layers, CIGS is a p-type semiconductor with a dopant density $p \approx 10^{16} cm^3$, whose Fermi energy is about 70 meV from the valence band [Roc08]. CIGS is a polycrystalline alloy with a direct band gap that varies with and local Ga concentration, from 1.67 eV for $CuGaSe_2$, where there is no In, to 1.06 eV for $CuInSe_2$, where there is no Ga [Roc08]. In general, the Ga concentration forms a gradient of band gap and Fermi energy that is larger at the back side than at the front side, so that the excited electrons in the back layers are driven towards the front part of the alloy. This latter fact favours electronic and hole exchange with a buffer layer.

5.2 Buffer Layers

Buffer layers are n-type semiconductors with a high bandgap, making them transparent to visible light, which are deposited on top of CIGS semiconductors to improve cell efficiency and prevent oxidation or degradation of the semiconductors. To avoid charge recombination, the doping level must be high enough to ensure that currents flow in only one direction. The highest charge injection efficiency from the absorber to the buffer is achieved when the absorber conducting bands and the buffer conducting band have a spike conformation (see 3.2.1) with a difference between 0 and 0.4 eV[Min+01]. The inhibition of charge recombination in surface states of the absorber due to a buffer is referred to in the literature as surface passivation. In general, the efficiency of the solar cell composed of CIGS and buffer layer decreases with buffer length, so that in general as thin a layer as possible is required, although the rate of decrease with length is highly dependent on the buffer material[OA17].

5.2.1 CdS

The highest efficiencies of CIGS have been achieved in combination with CdS buffer layers. The reasons for their high efficiency are based on a natural band alignment with an optimal offset to slow down charge recombination [NBV95] and a near perfect match with the CIGS lattice at the interface [Can+00]. In addition, CdS has demonstrated diffusion within the absorber during chemical bath deposition on a CIGS, resulting in high junction quality [NK99].

5.2.2 Zn(O,S)

Given the toxicity of Cd in the CdS buffer, a natural substitute with similar physical characteristics is an element of the same group but with a different period in the periodic table. The ZnS buffer system deposited in a CIGS has an observed band alignment offset of over 1 eV, resulting in a highly inefficient system. To reduce the offset in the band alignment of the system, oxygen can be added to form a Zn(O,S) alloy with an offset dependent on the ratio of oxygen or sulfur, in addition to the growth conditions of the alloy. Optimizing parameters that play a role in band alignment have been shown to offset the band alignment by 0.2 eV, which is in the optimal range for a buffer in a CIGS [PB+06].

5.2.3 In_2S_3

The band gap of In_2S_3 was estimated to be 2.82 eV [AA20], which is larger than the band gap of CdS or Zn(O,S) in the CIGS contact zone. As its overall electroaffinity is lower than that of CdS, the band alignment of the CIGS In_2S_3 system is in the optimal range for its use as a buffer. Physical properties such as its good transparency in the visible range make it an interesting semiconductor to replace CdS as a buffer in contact with the CIGS [TKD21]. Numerical studies have estimated the efficiency of the In_2S_3 photovoltaic cell in contact with a CIGS to be in the order of 20%, which is comparable to the efficiency obtained with a CdS buffer.

5.3 Samples

The $CuIn_{1-x}Ga_xSe_2$ samples used have a Ga concentration with x=0.3 on which different buffer layers were deposited. The CIGS growth method was performed in two steps, which allows to have a higher control on the level of Ga contraction by metalorganic vapor phase epitaxy (MOVPE) on a substrate of 500 μm thick (100)-oriented GaAs wafers at 520°C and 90 mbar, as is presented in the supplementary material of [Ram+22]. The buffers used were deposited using a Fujifilm Dimatix DMP 2850 inkjet printing, and whose parameters for In_2S_3 deposition are described in [Deb+22], and for Zn(O,S) in [Chu+21].The Ga concentration as well as the widths of each buffer layer were chosen to optimise the efficiency of the cell, being approximately the size shown in Fig. 5.1 where the band alignment is also depicted.

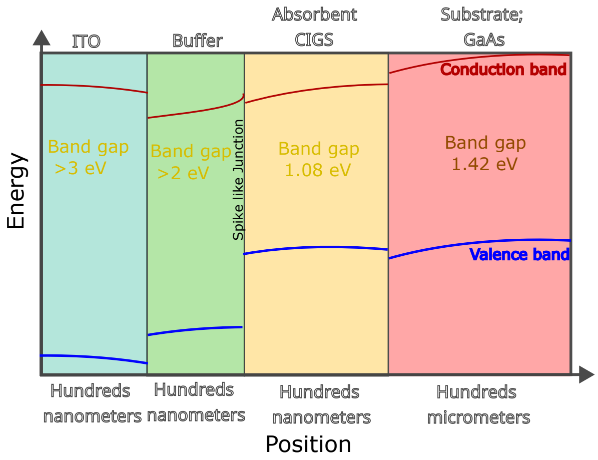

FIGURE 5.1: Schematic of Solar Cell sample conformation with buffer layers. The figure shows the approximate thickness and type of each component, as well as the band alignment formed for each junction.

5.4 Measuring electro-mobility in CIGS

The efficiency of a photovoltaic cell depends directly on the open circuit voltage parameter (V_{OC}) defined in 3.2.1. Maximising V_{OC} depends on maximising the decay time of the excitations while maximising the mobility of the excited charges. The mobility (μ) is a parameter that quantifies the static conductivity (σ_0) per free charge in a material. For the case of a semi-conductor with optically excited charges, the static conductivity is given by

$$\sigma_0 = ne\mu \tag{5.1}$$

where n is the excited charge density and e is the fundamental electron charge. Mobility is therefore an effective interaction factor that includes all interactions of the medium with the excited charges, and allows an excited charge carrier to be considered as a free charge carrier. The effective interaction of an excited charge carrier with the medium involves the effective mass (m), mean time between collisions (τ) of carrier and the probability that the charge is trapped by a defect or acts as a trapped charge due to a high electron-hole binding energy as in the case of excitons. Considering the trapping probability as (Φ_{trap}) the mobility is mathematically described by

$$\mu = (1 - \Phi_{trap}) \left(\frac{\tau e}{m} \right). \tag{5.2}$$

Where the quotient $(-m/\tau)$ plays the role of viscous damping in an equation of motion of charges as a forced harmonic oscillator. This factor depends on the electronic band structure of the material, the probability of collision with phonons and material defects [GP00].

The response of free electrons in a material to an oscillating electromagnetic field far from any resonance in the medium, implies a complex conductivity as a function of the mean time between collisions of the charges and the oscillation frequency of the field (ω). This complex conductivity in a material is given by the equation obtained with the Cole-Davidson model [DC50]

$$\sigma(\omega) = \frac{\sigma_0}{(1 - i\omega\tau)^{\beta}} \tag{5.3}$$

where β is an empirical parameter between zero and one that serves as a weighting function for the physical mechanisms of the system under study. When β is equal to 1, the model is equivalent to a gas of free charges, equivalent to the Drude model; on the other hand, when β is less than 1, the model deviates from the Drude model, being in many cases a better approximation to the response of a dielectric material. In general, the Drude model is a good approximation in dielectrics for excited charge densities higher than $10^{17} cm^{-3}$, lower densities require weighting β to values less than 1 [JG97]. In general, when determining the mobility of photovoltaic cells operating at low photon densities for electricity generation, it is necessary to study excitation levels not much higher than the dopant level, typically of the order of $10^{16} cm^{-3}$. The latter suggests modelling the conductivity of the cells using 5.3 with a β slightly less than one. Determination of the complex conductivity allows the dielectric function of the material in the measured spectral region to be expressed as,

$$\epsilon(\omega) = 1 + \frac{4\pi i \sigma(\omega)}{\omega}, \tag{5.4}$$

where it is normal to define a $\epsilon_1(\omega)$ and $\epsilon_2(\omega)$ as the real and imaginary part of it. Equivalently this allows us to determine the refractive index ($n(\omega)$) and absorption of the material ($k(\omega)$) as

$$n(\omega)^2 = \frac{1}{2}\left(\epsilon_1(\omega) + \sqrt{\epsilon_1(\omega)^2 + \epsilon_2(\omega)^2}\right), \tag{5.5}$$

and

$$k(\omega)^2 = \frac{1}{2}\left(-\epsilon_1(\omega) + \sqrt{\epsilon_1(\omega)^2 + \epsilon_2(\omega)^2}\right). \tag{5.6}$$

Due to the intrinsic electric field in the depletion region for optimal CIGS operation, the mobility of the excited charges allows a separation of electrons and holes and a consequent increase in V_{OC} [WCW15]. Just as the refractive index and absorption change with time after excitation, the mobility is also a time-dependent property. If the mobility is drastically reduced in a short period of time, the distribution of electrons and holes will have a bigger spatial overlap and a smaller average distance between the charges. The latter results in a lower V_{OC} compared to the case where the higher mobility is maintained for a longer period of time implying consequences on cell efficiency. The mobility of the free excited charges starts to interact with the lattice after the temperature has relaxed and the charges occupy real states, leading to a coupling with the phonons. This coupling with phonons can induce in many materials migrations through different valleys and peaks of the band structure for electron and hole populations respectively [Cal+16] in times even on the order of tens of femtoseconds [Pup17]. These migrations of the excited charges through the band structure result in a change in the geometry of the potential to which the charges are subjected and therefore a change in the effective mass, and therefore in the mobility. Other phenomena with similar origins, such as polarons, or other origins, for example trapping by bound states like excitons and defects, will also leave their mark in the time-dependent charge mobility.

Mobility has a direct effect on the probability of charge recombination and hence on lifetime. The main recombination mechanisms for photovoltaic cells are radiative recombination, Auger recombination and defect-mediated recombination, the latter being the most charge mobility dependent. Radiative recombination is the transit of an electron in the conduction band to occupy a free state in the valence band. The origin of this process is spontaneous decay and is more likely to occur in direct band gap semiconductors than in indirect band gap semiconductors [Evs22]. In particular for disordered media such as organic materials, including organic PV cells, the recombination rate is directly related to the mobility of electrons and holes according to the Langevin recombination rate [Van+09]. Auger recombination is a three-excited-charge decay mechanism in which an electron and a hole recombine, emitting a photon or phonon that is absorbed by another excited charge, inducing an interband transition of excited states. Defect-mediated recombination, or Shockley-Read-Hall recombination, is a non-radiative mechanism based on the trapping of free charges by vacancies in defects, absorbing the momentum of the charges and transferring this energy to the lattice in the form of phonons. The probability of occurrence of this mechanism (B_{SRH}) is the product of the effective trapping cross section (SRH_{SRH}) and the probability of encounter between the free charges and the defect. The latter is calculated as the product of the defect density (N_{def}) and the average velocity of the free charges ($v_t h$) with a thermal distribution taking into account an effective mass of the charges which is a function of the mobility μ [SR52]

$$B_{SRH} = \sigma_{SRH} N_{def} v_{th}(\mu). \tag{5.7}$$

The dependence of the decay and trapping mechanisms on the mobility of the charges means for some cases an optimal mobility that maximises the efficiency of the PV cell, being particularly important for organic solar cell [TLR12].

One way to measure conductivity in a time-dependent manner is to use time-resolved terahertz spectroscopy. Time-resolved THz spectroscopy is a pump-probe technique where the pump allows the creation of a hole-electron pair and the probe is a pulse in the few terahertz range [Dex17]. THz radiation does not have enough energy to excite electrons from a ground state to an excited state even in an intraband process, so it can only drive the oscillation of free charges, which is useful for determining conductivity. In line with the pump-probe technique, the probe field is indirectly modulated by the modulation of the pump field. Typically, the probe is simply detected by a photodetector after spectral filtering or not, thus extracting the modulation in the pulse intensity related to the absorption process in a material. For time-resolved terahertz spectroscopy with pulses of a few THz, spectral filtering is generally not performed and changes in absorption over time are assumed as if the pulse were a monochromatic source. This approach can be justified in most cases by the fact that if a pulse is composed of waves with frequencies below 6 THz, all these contributions will have energies lower than the thermal energy of the medium at room temperature. As a result, the effective response of a material being investigated at room temperature will have an energy uncertainty greater than the spectral width of the pulse. In general, for a probe pulse in the THz range, in addition to simple detection, it is also possible to study the total field reconstruction using the Electro Optical Sample (EOS) technique. With this approach it is possible to extract the modulation of the temporal intensity and temporal phase of the pulse, or equivalently the spectral intensity and spectral phase of the field, for each instant of the interaction. The modulation of spectral intensity and phase in the pulse translates into a change in absorption and refractive index as a function of frequency in the material due to the excitation of charges by the Pump. This spectrally resolved information makes it possible to distinguish physical processes in a material, such as conductivity or optical phonon absorption lines in the few THz range. Although another way of spectrally resolving a pulse in the THz regime, and similarly to a probe in other spectral ranges, is by spectral filtering or the use of monochromators, this only allows information to be extracted from the modulation of the time-dependent spectral intensity. In general, it is desirable to have information about the intensity and spectral phase of the probe pulse for each delay time with respect to a pump, as this enhances the quality of the information extracted by the use of the Kramer-Kronig relations [PS09]. Higher fidelity data allow more accurate discrimination of physical phenomena in materials such as conductivity and phonon absorption lines in the THz range.

Solving the equations for wave propagation in a medium and considering the change in susceptibility only due to the change in conductivity will imply a change in the transmission of the incident field ΔE_i which is related to the conductivity as

$$\Delta\sigma(\omega,\omega_p) = -\epsilon_0 c(n_1+n_2)\frac{\Delta E_i(\omega,\omega_p)}{E_i(\omega,\omega_p)}. \tag{5.8}$$

where n_1 is the refractive index of the medium under study, n_2 is the refractive index of the substrate, and the dependence ω refers to the spectral dependence of the functions, while ω_p is the inverse of the Fourier transform of the time delay between pump and probe.

5.5 Measuring excited charge mobility Experimental Setup

5.5.1 Generation and characterisation of few THz pulses

Due to the low energy of a 1-THz photon ($\approx$ 4m eV), the generation of photons in this range can be induced by a DFG between photons contained in the same femtosecond pulse centred in the NIR or visible range, in a process called optical rectification [Dex17]. This mixing of photons associated to the same pulse will imply, by conservation of momentum in the DFG associated to this process, the generation of THz radiation collinear with the seed pulse. In particular, non-linear media with a zinc-blende crystalline structure and orientation (110), such as ZnTe and GaP, have demonstrated high efficiency in THz radiation generation processes by simple propagation of a femtosecond pulse [Che+01]. Furthermore, if the pulse is linearly polarised and travels in the direction of the $\hat{z}$ axis of the crystal, the rate of THz radiation generation can only be optimised by varying the azimuthal angle of the crystal and thus the projection of the direction of field oscillation onto the optical axes of the medium [Che+01]. Due to the geometrical nature of the electrical susceptibility tensor of a crystal, the angle that optimises the signal is the same for all zinc-blende unblended crystalline structure (110), fixed at $\theta = 54.7°$ between the direction of oscillation of the original pulse field and the $\hat{x}$ axis of the crystal [Che+01]. This optimisation of the direction of the medium's susceptibility for the THz generation rate involves the mixing of photons with equal and orthogonal polarisations due to the projections of the oscillation on different optical axes of the crystal. In this way, the angle of polarisation of the THz radiation depends on the angle θ between the direction of oscillation of the original field and the crystal axis. In particular, for the case with the optimised direction of the susceptibility tensor, the angle between the THz radiation and the $\hat{x}$ axis of the crystal is given by $\phi = 0^\circ$ [SK19]. In addition to optimising the direction of the susceptibility tensor to maximise the desired non-linear response in the optical rectification, another parameter that can be optimised in the THz generation process is the crystal length. The crystal length that maximises the intensity of the THz radiation generated by optical rectification is called the coherence length (L_{coh}) and can be calculated as the limiting length so that there is constant constructive interference of the generated radiation [NWH96]. Since the generation of THz radiation results from the nonlinear mixing of photons of different energy in the same pulse, a natural parameter in this context will be the group index of the medium with respect to the pulse wavelength $n_g(\lambda)$. This group index compared to the refractive index of the THz radiation in the material $n(\omega)$ allows to determine the phase shift of the radiation generated at the beginning of the crystal with respect to the radiation generated at a point at a distance L from the crystal. In this way the L_{coh} can be expressed mathematically by equating the phase shift to $L_{coh} = \pi c / \left(\omega_{THZ} |n_g(\lambda) - n(\Omega)|\right)$. Lengths shorter than L_{coh} do not maximise intensity, but allow for larger spectral widths in the pulses, while lengths longer than L_{coh} allow for less than optimal intensities and increasingly smaller spectral widths.

In particular in our experimental scheme we use ZnTe crystals, which is a semiconductor with a direct Band Gap of 2.26 eV, or equivalently 548 nm in wavelength, allowing the transmission of a fundamental pulse of Astrella Ti:Sa laser centred at 800 nm, generating a few THz radiation in its path. For THz generation, a crystal with a width of 500 μm has been used, which is one-sixth the L_{coh} for 800 nm [NWH96]. Due to the relatively low thermal damage threshold of ZnTe [Vid+13], a pulse train with a repetition rate of 1 kHz was used in a collimated beam with a diameter of 10 mm and an incident power of 85 mW, which can be varied using a transmission system consisting of a half-wave plate and a PBS, and of which only 28% of the po is transmitted through the crystal due to the optical impedance, in order to ensure a low fluence as well as a high THz radiation generation rate.

Due to the relatively low thermal damage threshold of the ZnTe [Vid+13], a pulse train with a repetition frequency of 1 kHz in a collimated beam of 10 mm diameter and an incident power of 85 mW was used to ensure a low fluence as well as a high THz radiation generation rate. The use of relatively high powers, which are optimised using a transmission system consisting of a half-wave plate and a PBS, is necessary because only 28% of this is transmitted by the crystal due to the optical impedance. To control the polarisation of the THz radiation generated in the ZnTe, a HWP is arranged to modify the polarisation angle of the incoming pulse. The polarisation of the incoming pulse has been chosen at an angle $\theta_{pol,800} = 54.7^{\circ}$ with respect to a vector parallel to the plane of the optical table and perpendicular to the beam propagation direction, which we will define as $\hat{x}_{table}$ vector. This choice of polarisation angle obliges us to orient the $\hat{x}$ axis of the crystal parallel to $\hat{x}_{table}$ in order to optimise the generation of THz radiation in the crystal with a polarisation parallel to the optical table. To separate the THz radiation from the 800 nm pulse, a Si wafer with a width of 1 mm was used, so that it has a transmittance of $\approx 10^{-45}$ for 800 nm and of 0.45 for 1 THz, leaving a clean transmission of the NIR signal. This wafer was installed to minimise reflection losses in the generated signal, so it was placed at the Brewster angle for 1 THz of $\theta_B = 73^{\circ}$ between the oscillating field and the vector normal to the wafer surface, where has been assumed the refractive index of the Si for 1 THz determined in [Ro/+97] . Due to the polarisation of the THz radiation parallel to the optical table, the wafer is only rotated in the plane of the table. The setup for the generation of THz radiation is shown in the figure 5.2. The characterisation of long wavelength pulses can be performed by means of the Electro Optical Sampling (EOS) technique. The EOS principle for characterising ThZ

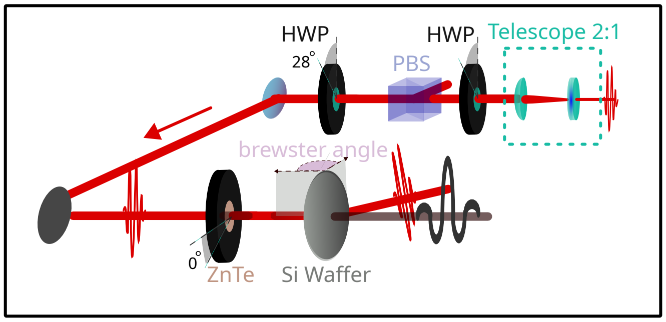

FIGURE 5.2: Experimental setup of THz radiation generation by optical rectification in ZnTe. Telescope 2:1 refers to a telescope which enlarges the beam cross-section by a factor of 2. The angles of the components are set for the optimum situation considering the polarisation filtering which the PBS generates.HWP is a half-wave plate, PBS is a polarizing beam splitter and Si waffer is a silicon waffer.

pulses is based on the Pockels effect in a non-centrosymmetric medium, which consists in the rotation of the polarisation of an electromagnetic wave due to the influence of an external electric field. Since the rotation of the wave is linear with the amplitude of the field, the polarisation state of a pulse several times shorter than the half of the wavelength of the THz radiation can be used to characterise the electric field of the few THz pulses if the experiment is repeated with different relative delays by scanning the long-wavelenght pulse. Experimentally we have used as a probe our linearly polarised fundamental pulses with 150 fs time duration, or with a spatial length of 45 μm, which is about 3 times shorter than half the wavelength corresponding to 1 THz. This pulse is reflected by a retroreflector delay line consisting of two mirrors on an electronic translation stage, so that the delay between the pulses can be varied in a controlled manner. The signal and the probe pulse are collinearly arranged by means of a combiner made of an ITO semiconductor.The reflection of the beam centred at 1 THz and transmission centred at 800 nm is focused by a gold parabolic mirror with a focal length of 50 mm, giving a beam waist at the focal point of 2 mm for the THz radiation. By using an additional lens in the probe path the beam width can be adjusted to be 200 μm at the focusing position of the THz radiation. This correction was made to optimize a non-linear mixing of the beams in this position. A

ZnTe is placed at the focus of the THz beam at an angle θ optimised for the interaction between the NIR and the signal. The polarisation state of the NIR is then analysed to compare it in the presence and absence of THz radiation. To analyse the polarisation state, the beam is collimated by a lens with a focal length of 15 cm, which normally absorbs all THz radiation, and directed onto a quarter wave plate (QWP). The QWP is oriented in such a way that, in the absence of THz radiation interacting with the NIR pulse in the ZnTe, the latter becomes circularly polarised. The polarisation components of this beam are then separated by a Wollaston prism and finally directed onto two Si detectors connected to a circuit that extracts the difference of the detected signal. For an incoming circular polarisation, the detected signal should be zero and only electronic noise should be detected. However, if THz radiation is present in the interaction, the QWP will induce an elliptical polarisation which, when measured by the detectors, produce a significant difference proportional to the amplitude of the THz field interacting with the probe with a certain delay. To extract the difference directly, it is usual to modulate the THz signal at half the repetition rate of the probe and to have a lock-in amplifier operating at the repetition rate of the THz radiation. This setup is shown in fig 5.3. The optimisation of ZnTe for EOS is based on its symmetry properties due to its crystal structure. The (001) oriented zinc blende crystalline structure have only one tensor element relevant for the interaction between the pulse frequencies (r_{41}) [Pla+01]. Thus, the relative angle between the NIR polarisations $\theta_{NIR/THz}$ and the THz radiation, and the angle between the THz radiation and the crystal axis $\hat{x}$, defined as $\phi_{THz/\hat{x}}$, are the only degrees of freedom of the problem [Pla+01]. Thus, the difference of the signal of each polarisation component ΔI due to the presence of the THz radiation for a given delay between pulses τ, is given by

$$\Delta I(\theta_{THz/\hat{x}}, \phi_{NIR/THz}, \Delta\tau) = I_p \frac{\omega_{probe} n^3 E_{THz}(\Delta\tau) r_{41} L}{2c} \cdot \\ \left(cos(\theta_{THz/\hat{x})} sin[2(\phi_{NIR/THz} - \theta_{THz/\hat{x}})] + 2 sin(\theta_{THz/\hat{x}}) cos[2(\phi_{NIR/THz} - \theta_{THz/\hat{x}})] \right). \tag{5.9}$$

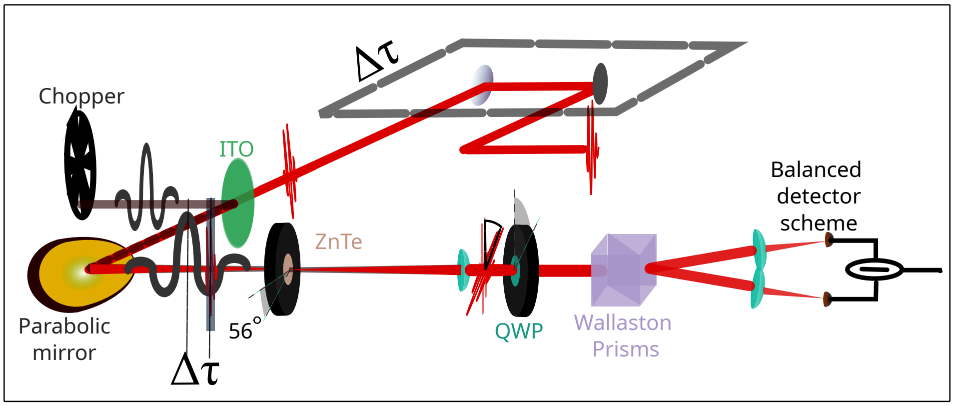

FIGURE 5.3: Experimental scheme for the characterisation of the few-THz centred pulses. This is a retro configuration on an electrical translation stage which allows precise control of the optical path length. This optic has implications on the temporal overlap between the few THz pulse and the 800 nm centred probe. The chopper indicates that the THz radiation must be modulated. ITO is a semiconductor that serves as a combiner. The parabolic mirror has a focal length of 10 cm.

with I_p the intensity of the probe pulse, n the refractive index of the medium for 800 nm, ω_{probe} the optical frequency of the pulse, E_{THz} the local amplitude of the THz field. This difference can be maximized if $\phi_{NIR/THz}$ is zero or $\pi/2$, the former case being the one we have used in our measurements, and where $\theta_{THz/\hat{x}}$ must be equal to $3\pi/2$. This difference is directly proportional to the difference measured by the lock in amplifier in the experiment, and therefore allows us to know the profile of the characterised pulse by varying $\Delta\tau$

As the few THz radiation can be in resonance with vibrational and rotational modes of molecules present in the air composition, certain actions are usually taken to maximise the signal to noise ratio. One of these actions is to minimise the distance between the generation of the THz radiation and its characterisation, and the other is to fill the space with molecules that are not in resonance with the few THz radiation. In particular, in our experiment the space was filled with nitrogen, which displaces molecules that can interact with the THz radiation as the pulse propagates. The differences in the characterisation of a pulse propagating in a nitrogen-filled and an air-filled space can be seen in the fig 5.4

where in a) is the measurement of the field using EOS in the time domain, and b) is the fourier transform intensity of the field characterised in a).In the temporal trace one of the most significant differences is that the absolute maximum of the nitrogen-transmitted signal is higher than the absolute maximum of the air-transmitted signal. This contrasts with the decrease in peaks comparing the nitrogen-transmitted signal with the air-transmitted signal for times longer than 2 ps. Spectrally the curves for the signal transmitted in nitrogen and air are consistent showing deeps and peaks at the same positions. The major difference is found in a lower spectral intensity at 1.2, 1.4, 1.6, 1.7 and the range between 2.3 and 2.5 THz for the air-transmitted signal. These deeps coincide perfectly with the absorption of water in these spectral ranges [CDZ14], being therefore attributable to the presence of water vapour in the air. Additionally, this suggests that although nitrogen has occupied part of the propagation space, the water molecules have not been completely removed.

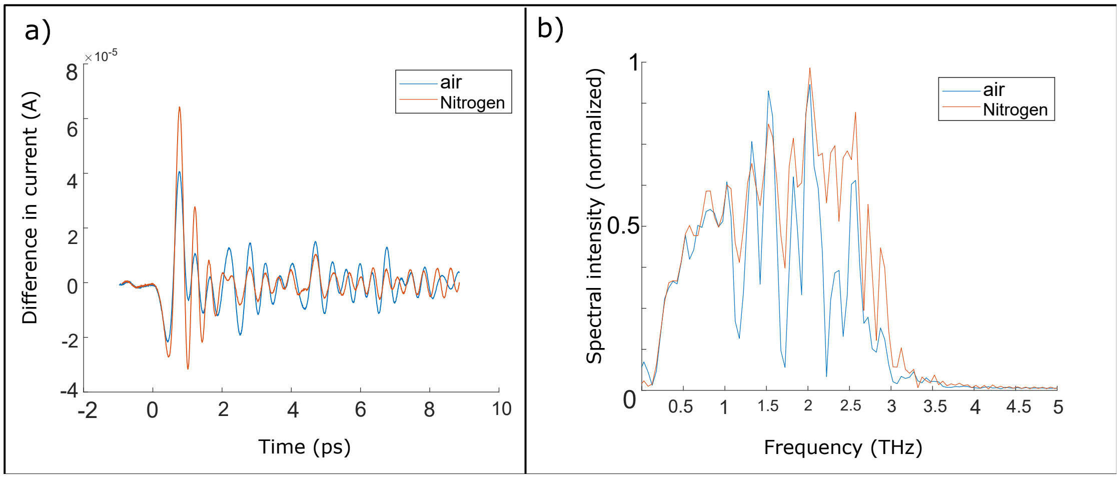

FIGURE 5.4: Characterization of a few THz pulse propagating in air (blue) and nitrogen (red). a) shows the current difference measured in a balanced detection scheme in an EOS as a function of the delay between the probe pulse and the THz pulse. b) shows the spectral intensity normalised to the global maximum of the curve shown in a).

5.5.2 Measuring conductivity

To measure the conductivity of a sample by using 5.8, the sample is excited by a pump pulse with a photon energy that allows electrons to be promoted from the valence band to the conduction band. Its state is then probed with a pulse of THz radiation which is subsequently characterised. To probe the sample, the THz radiation is focused on the sample position and then recollimated by a similar gold parabolic mirror with a focal length of 10 cm. To optimise collimation, the second parabolic mirror is mounted on a translation stage, which allows significant changes in the optical path of the beam to be compensated for when different samples are placed. To ensure optimum geometrical conditions for good beam focusing and collimation, the mirror is mounted on a magnetic base before the beam hits the first parabolic mirror, providing a long alignment line for the THz radiation and can also be used to align a visible auxiliary laser to verify the alignment of the parabolic mirrors. On the other hand, the pump is aligned on a mechanical translation stage, which makes it possible to control the relative delay time between the pump and the THz radiation. Since the pump wave energy is higher than the band gap energy of the material under study, it has a much shorter wavelength than the THz radiation, so it is necessary to avoid focusing on the sample point to ensure that the pump has a larger excited area than the area covered by the THz probe. To avoid the pump and THz radiation beams having the same focal point, the paths and focusing mechanisms were arranged independently, forming an angle of $\approx 10^\circ$ between the pump and THz radiation beams just before the sample. Possible scattering from the pump, which would contaminate the probe characterisation in the EOS, is minimised by the presence of the ITO combiner for the EOS input. The experimental setup requires a modulation in the THz pulse and in the pulse pumping system as shown in the Fig. 5.5.

In general, it is desirable in a pump-probe experiment that the pump has half the repetition rate of the probe. The latter implies that the pump has half the repetition rate of the THz radiation and the THz radiation has half the repetition rate of the EOS probe. A chopper is a wheel with regions of equal area that block or let through a beam of light. These regions are equidistant from each

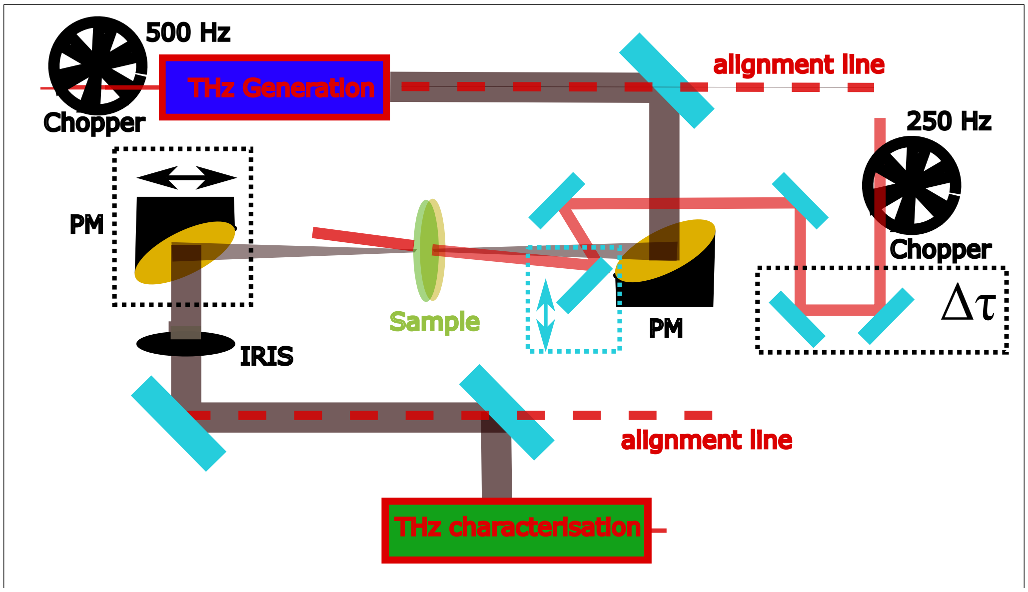

FIGURE 5.5: Experimental setup to measure the electronic mobility. The THz Generation and THz characterisation boxes refer to the experimental set-up shown above. In addition, the alignment lines are shown to ensure the correct functioning of the system. The Pump marked as a red line is centred at 800 nm and for its alignment a translation stage is used to reduce the angle of the pump and the probe to a minimum. The PMs are parabolic mirrors of 10 cm focal length. In addition, there are two choppers configured at different repetition rates.

other, so if this wheel rotates at a constant speed, it is not possible to generate a case of signal modulation at a quarter of the repetition rate of the laser. By using a chopper it is possible to modulate the pulse train so that two pulses are transmitted followed by two blocked pulses. It can be shown that for the EOS measurement after the pump probe, the modulation of the pump using a chopper as described above is equivalent to the modulation of the pump pulse at a quarter of the repetition rate. This statement is supported by the fact that the EOS measures on the THz pulse, which has half the repetition rate of the probe, so that what happens when the THz radiation is blocked has no effect on the measurement. The last has the consequence that the green squares in Fig. 5.6 a) are the only relevant cases, and where it is clear that the cases described above are identical. To obtain this effect of two locked pulses followed by two unlocked pulses, the diameter of the beam cross-sectional area at the chopper position must be half the blocked area of each helix, and the angular velocity (ω) at which the chopper rotation is set must be one-quarter of the repetition rate. Therefore if the chopper phasing is adjusted as shown in Fig. 5.6 b) the desired situation is achieved.

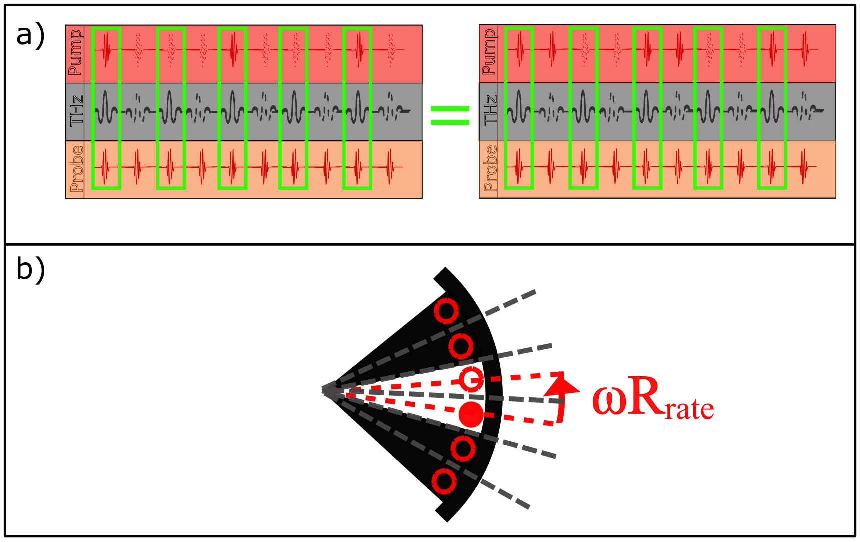

FIGURE 5.6: a) Left, scheme of pulse modulation at a repetition rate of 1 kHz for the probe, 500 kHz for the THz pulse and 250 kHz for the Pump pulse, where the pulse with dotted lines indicates blocking and the solid line indicates its participation in the experiment. Right, pulse modulation scheme using a chopper with a repetition rate of 500 kHz for the THz pulse and 250 kHz for the Pump pulse. Since the only relevant situations are when the THz pulse is involved, we compare these situations indicated by a green square. Comparing these green squares shows that the situations are equivalent. b) the chopper helices are divided into halves by dotted grey lines. Rotating chopper over time produces a new intersection point for each pulse with the chopper indicated by an offset of ωR_{rate}, where ω is the angular velocity of the chopper and R_{rate} is the repetition rate of the pulses. The meeting points are marked with red circles. If the cross-sectional area circle is completely contained in the middle of the chopper, the situation shown in (a) on the right is achieved.

From a technical point of view, if the photovoltaic cell is deposited on a semiconductor substrate, the substrate must have a higher bandgap than the cell. This condition makes it possible to choose a pump wavelength that promotes excitations in the cell but not in the substrate, thus avoiding responses that could lead to errors in interpretation. In the case of our sample, a CIGS sample with a bandgap of 1.08 eV was deposited on GaAs with a bandgap of 1.42 eV, fulfilling the previously established condition. This makes the NIR OPA pulses centred at 1 μm presented in section 2.3.3 good candidates for sample excitation. In addition, the fluence used for a pump in this context should be such that the excited charge density does not exceed the doping level, as previously discussed.

5.5.3 Measuring Excited Carrier Mobility

The mobility is directly related to the conductivity via the excited charge carrier density and the fundamental charge of the electron according to 5.8. Both the excited charge carrier density and the mobility are physical parameters that evolve in time after charge excitation. Therefore, the determination of the mobility from the measurement of the conductivity dynamics must also take into account the dynamics of the charge carrier density. For the measurement of charge carrier dynamics a Pump-Probe scheme is implemented using as pump the NIR OPA pulses centred at 1 μm presented in section 2.3.3 and the probe is white light generated in a YAG crystal supporting photons in the range of 1.15 μm, where approximately the Band Gap of the samples is expected. The configuration of this Pump-Probe scheme is measured in reflection due to strong scattering in the transmitted beam, possibly due to problems in the polishing of the substrate. The probe signal is measured on a Fast Cam system from Princeton Instruments which spectrally resolves the signal by using a diffraction grating and detects it on a CCD array. This camera, due to its detectors and the diffraction grating used, has a sensitivity range of 800-1300 nm. The alignment of the camera was done by measuring the spectrum of the white light, while by means of two band pass filters at 900 and 1200 nm, we made sure that the spectral lines are placed in the corresponding positions. The camera has an acquisition rate that is guided by the repetition rate of the laser. Additionally, this camera has the possibility to subtract the differential reflection by connecting to a trigger at the Pump repetition frequency. To verify the stability of the measurements, a measurement on the same sample was carried out during a whole night, showing to be stable if the sample has a previous illumination of about 40 minutes, which can be attributed to the thermal stabilisation of the system under study. The transient reflection response of the Pump-Probe is given by fig. 5.7, which is an average of 3 repeated measurements, reducing systematic errors, for each sample and in each measurement each line at different times is an average of 150 measurements without moving the delay between the Pump and the Probe. Both the number of repeat measurements and the total number of measurements without moving the delay was optimised by analysing the noise and trying to reduce the measurement time. Each sample is measured for a time of 3 hours, and a measurement using a photodetector at a particular wavelength is performed before and after the 3-hour measurement. If these two photodetector measurements are consistent with each other the measurement is considered reliable, otherwise the measurement is discarded.

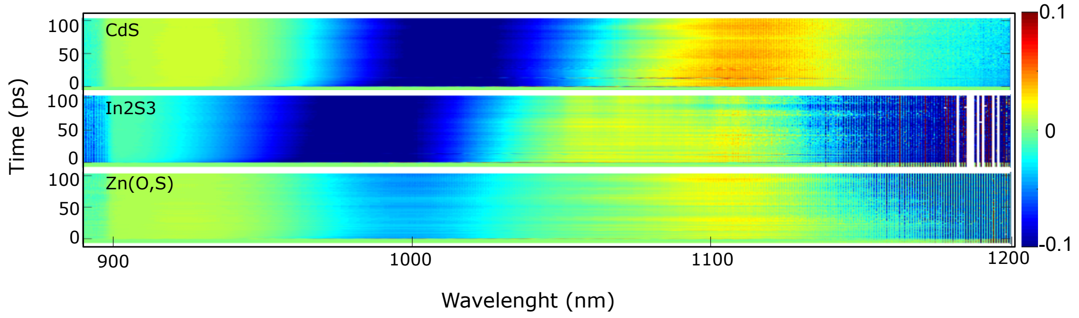

FIGURE 5.7: Spectrally resolved transient reflection response in the first 100 ps of a CIGS sample with different buffer layers. The sample was excited with the NIR OPA centred at 1020 nm with a fluence of 330 $\mu J/cm^2$ and the change was detected by a white light pulse probe generated in YAG. The colour scale is on the right side of the figure.

In addition to the possible injection of charge carriers from the absorber into the buffer, the contact between them can additionally affect the dielectric response of the material, due to charge accumulation at the contact. This effect on the dielectric response can slightly change the band gap of the CIGS and thus the refractive index for different wavelengths in the medium. This helps to explain why the transient reflection profiles, although similar, do not have their peaks and dips in exactly the same position. In general, the spectral profiles of the transient reflection with the CIGS in contact with the different buffers show a region with a decrease in reflection between two zones with higher reflection due to the pump. Because of the normal width of the CIGS absorbers of a few hundred nanometres, an appropriate optical description for the system is expected to be that of a Fabri Perot interferometer with high absorption. So as the CIGS is excited its refractive index changes and the optical impedance between materials may favour a higher finesse factor, consistent with that observed in 5.7.

The transient response of the CIGS reflectance with the different buffer layers shows an almost constant response during the first 100 ps. This response is consistent with pump probe experiments on the transient transmission of pulses in the few THz range in CIGS samples with different concentrations of In and Ga in contact with CdS. In these experiments it was shown that in a CIGS/CdS system, where the CIGS has a lower Ga concentration than the In, charge recombination has time constants in the order of nanoseconds, showing a surface passivation effect [Bal+20]. The surface passivation effect is the result of an efficient injection of excited charges from the absorber surface into the buffer layer and a consequent slow recombination. In the same context, if the surface had remained active, the surface states would have induced a first dynamical response with a time constant of about 100 ps [Bal+20]. The absence of dynamic effects with times shorter than 100 ps in our measurements suggests that all buffer layers used in CIGS with at least a Ga concentration of 0.3 versus an indium concentration of 0.7 achieve surface passivation. This absence of fast dynamic effects in the measured traces, even at the higher resolution offered by the white light probe, which in the worst case for our experiment can be estimated to be hundreds of femtoseconds, shows that ultrafast phenomena that could affect the band gap at lifetimes lower than the resolution of the THz pulse experiment do not take place. Had traces of other ultrafast effects, such as exciton formation, been found at energies below the band gap, these experiments would have provided clues for design strategies to optimise the efficiency of the solar cell.

Chapter 6

Summary

Charge injection at junctions of semiconductor with other materials is already widely used in electronics, but also has a high potential in emerging optical applications. The potential in optics for using charge injection or extraction in semiconductors is based on the fact that the probability of recombination and interaction between excited charges is affected by a higher concentration of one carrier relative to another, changing the dielectric response of the medium over time. In general, the difference in the dielectric response of a medium over time after excitation is mediated in the first picoseconds by Coulomb-type interactions between excited charges, while for longer times until the excited charges decay, interactions between quasiparticles or collective excitations involving interactions with the lattice are dominant. Some collective excitations, such as excitons, which are fundamentally generated by the attractive force between particles or quasiparticles of opposite charge, are highly susceptible in their formation to charge extraction or injection. This susceptibility can be understood because the injection or extraction of charges involves a higher concentration of one type of charge than the other, implying a higher probability of scattering between the majority charges compared to the scattering between charges of different types necessary for the formation of e.g. excitons. This sensitivity in the formation of excitons or other bound state collective behaviour may ultimately imply a change in the probability of their formation, affecting, for example, the time-dependent effective mass of the excited charges, causing a change in their lifetime at the depletion region of a junction of two materials. A study of the effect of charge injection in semiconductors should include a study of its effect on the formation of collective excitations, as well as studies at long times that allow us to quantify its effects on the dynamics of the excited charges;

Regarding the first point, the effect of charge injection on the dynamics of exciton formation in a WS_2 bulk was studied using a pump-push-probe experiment in which the excitation or injection of charges was promoted independently. The experiment showed that when the ratio of injected charges to excited charges is higher, the signal reflection curve with the wavelength associated with the exciton has a higher decay rate in the first picosecond, and then remains constant. This shows that our hypothesis that the dynamics of collective exciton formation is influenced by charge injection is correct. While the dynamics of exciton formation was affected in our case, how this can change the probability of exciton formation is not entirely clear, and further experiments are needed to quantify this effect.

Regarding the second point, a system of experiments, still under development, was presented that allows to extract the time-dependent mobility of the excited charges in a comprehensive way, distinguishing parameters such as the lifetime of the excited charges from other dynamical parameters such as the effective mass, by analysing two different experiments in a complementary way. The two experiments proposed are pump-probe experiments, where in one case the probe is a pulse centred on frequencies of a few THz and in the other case the probe is a pulse of white light. The first experiment makes it possible to measure the dynamics of the transient conductivity of the sample, while the second measures the time evolution of the dielectric response of the material at wavelengths above the bandgap. The distinction between the evolution of these two parameters provides a robust setup for analysing, for example, the effect of the extraction of charges from the semiconductor absorbed by a buffer layer due to the intrinsic electric field between them. In this context, this experiment not only allows us to study the effects of charge extraction on the long-term dynamics of excited charges, but also provides clues that can help in the design of more efficient photovoltaic cells.

In line with the above-mentioned experiments in ultrafast optics, different experimental setups for the generation of ultrashort pulses in different spectral ranges have been presented. These experimental set-ups cover the generation of intense pulses in the visible, near-infrared, mid-infrared and a few THz range, as well as an original proposal for the generation of stable and less intense white light pulses in liquid media such as water.

Bibliography

[AA20] Md Ali Ashraf and Intekhab Alam. “Numerical simulation of CIGS, CISSe and CZTS-based solar cells with In2S3 as buffer layer and Au as back contact using SCAPS 1D”. In: *Engineering Research Express* 2.3 (2020). ISSN: 26318695. DOI: 10.1088/2631-8695/abade6.

[AEA22] Athil S. Al-Ezzi and Mohamed Nainar M. Ansari. “Photovoltaic Solar Cells: A Review”. In: *Applied System Innovation* 5.4 (2022), pp. 1–17. ISSN: 25715577. DOI: 10.3390/asi5040067.

[ATB91] Lucio Claudio Andreani, Francesco Tassone, and Franco Bassani. “Radiative lifetime of free excitons in quantum wells”. In: *Solid State Communications* 77.9 (1991), pp. 641–645. ISSN: 00381098. DOI: 10.1016/0038-1098(91)90761-J.

[Ava+11] Sushobhan Avasthi et al. “Role of Majority and Minority Carrier Barriers Silicon/Organic Hybrid Heterojunction Solar Cells”. In: *Advanced Materials* 23.48 (Nov. 2011), pp. 5762–5766. DOI: 10.1002/adma.201102712. URL: https://doi.org/10.1002/adma.201102712.

[Bal+20] Marco Ballabio et al. “Composition-Dependent Passivation Efficiency at the CdS/CuIn1-xGaxSe2 Interface”. In: *Advanced Materials* 32.9 (2020), pp. 1–6. ISSN: 15214095. DOI: 10.1002/adma.201907763.

[Bat89] Inder P. Batra, ed. *Metallization and Metal-Semiconductor Interfaces*. Springer US, 1989. DOI: 10.1007/978-1-4613-0795-2. URL: https://doi.org/10.1007/978-1-4613-0795-2.

[BBR09] M. Bradler, P. Baum, and E. Riedle. “Femtosecond continuum generation in bulk laser host materials with sub-μJ pump pulses”. In:

Applied Physics B: Lasers and Optics 97.3 (2009), pp. 561–574. ISSN: 09462171. DOI: 10.1007/s00340-009-3699-1.

[Bec14] Friedhelm Bechstedt. "Beyond Static Screening". In: *Springer Series in Solid-State Sciences*. Springer Berlin Heidelberg, Dec. 2014, pp. 539–572. DOI: 10.1007/978-3-662-44593-8_22. URL: https://doi.org/10.1007/978-3-662-44593-8_22.

[Ben93] T. M. Benson. "Book Review: Optical Fiber Communications.—principles and practice 2nd Ed". In: *The International Journal of Electrical Engineering &amp Education* 30.2 (Apr. 1993), pp. 187–188. DOI: 10.1177/002072099303000222. URL: https://doi.org/10.1177/002072099303000222.

[Bor+99] Max Born et al. *Principles of Optics*. Cambridge University Press, Oct. 1999. DOI: 10.1017/cbo9781139644181. URL: https://doi.org/10.1017/cbo9781139644181.

[Boy03] Robert Boyd. *Nonlinear Optics*. Elsevier, 2003. DOI: 10.1016/b978-0-12-121682-5.x5000-7. URL: https://doi.org/10.1016/b978-0-12-121682-5.x5000-7.

[Cal+16] Philip Calado et al. "Evidence for ion migration in hybrid perovskite solar cells with minimal hysteresis". In: *Nature Communications* 7 (2016), pp. 1–10. ISSN: 20411723. DOI: 10.1038/ncomms13831. arXiv: 1606.00818.

[Can+00] B. Canava et al. "Wet treatment based interface engineering for high efficiency Cu(In,Ga)Se2 solar cells". In: *Thin Solid Films* 361 (2000), pp. 187–192. ISSN: 00406090. DOI: 10.1016/S0040-6090(99)00861-5.

[Cao+02] J C Cao et al. "Interband impact ionization in THz-driven InAs/AlSb heterostructures". In: *Semiconductor Science and Technology* 17.3 (Feb. 2002), pp. 215–218. DOI: 10.1088/0268-1242/17/3/306. URL: https://doi.org/10.1088/0268-1242/17/3/306.

[CDZ14] Benjamin Clough, Jianming Dai, and X. Zhang. "Laser Air Photonics: Covering the "Terahertz Gap" and Beyond". In: *Chinese Journal of Physics- Taipei-* 52 (Feb. 2014), pp. 416–430. DOI: `10.6122/CJP.52.416`.

[Che+01] Q. Chen et al. "Electro-optic transceivers for terahertz-wave applications". In: *Journal of the Optical Society of America B* 18.6 (June 2001), p. 823. DOI: `10.1364/josab.18.000823`. URL: `https://doi.org/10.1364/josab.18.000823`.

[Che+14] Alexey Chernikov et al. "Exciton binding energy and nonhydrogenic Rydberg series in monolayer WS2". In: *Physical Review Letters* 113.7 (2014), pp. 1–5. ISSN: 10797114. DOI: `10.1103/PhysRevLett.113.076802`. arXiv: `1403.4270`.

[Che+15] Alexey Chernikov et al. "Population inversion and giant bandgap renormalization in atomically thin WS 2 layers". In: *Nature Photonics* 9.7 (2015), pp. 466–470. ISSN: 17494893. DOI: `10.1038/nphoton.2015.104`.

[Chu+21] Van Ben Chu et al. "Waste- And Cd-Free Inkjet-Printed Zn(O,S) Buffer for Cu(In,Ga)(S,Se)2Thin-Film Solar Cells". In: *ACS Applied Materials and Interfaces* 13.11 (2021), pp. 13009–13021. ISSN: 19448252. DOI: `10.1021/acsami.0c16860`.

[CLZ15] Manish Chhowalla, Zhongfan Liu, and Hua Zhang. "Two-dimensional transition metal dichalcogenide (TMD) nanosheets". In: *Chemical Society Reviews* 44.9 (2015), pp. 2584–2586. DOI: `10.1039/c5cs90037a`. URL: `https://doi.org/10.1039/c5cs90037a`.

[Col+18] Alejandra L. Collopy et al. "3D Magneto-Optical Trap of Yttrium Monoxide". In: *Physical Review Letters* 121.21 (Nov. 2018). DOI: `10.1103/physrevlett.121.213201`. URL: `https://doi.org/10.1103/physrevlett.121.213201`.

[DC19] Audrius Dubietis and Arnaud Couairon. “Governing Physical Effects”. In: *SpringerBriefs in Physics*. Springer International Publishing, 2019, pp. 9–26. DOI: 10.1007/978-3-030-14995-6_2. URL: https://doi.org/10.1007/978-3-030-14995-6_2.

[DC50] D. W. Davidson and R. H. Cole. “Dielectric relaxation in glycerine [11]”. In: *The Journal of Chemical Physics* 18.10 (1950), p. 1417. ISSN: 00219606. DOI: 10.1063/1.1747496.

[Deb+22] Alice Debot et al. “Inkjet-printed indium sulfide buffer layer for Cu(In,Ga)(S,Se)2 thin film solar cells”. In: *Thin Solid Films* 745.June 2021 (2022). ISSN: 00406090. DOI: 10.1016/j.tsf.2022.139096.

[Dex17] Susan L. Dexheimer, ed. *Terahertz Spectroscopy*. CRC Press, Dec. 2017. DOI: 10.1201/9781420007701. URL: https://doi.org/10.1201/9781420007701.

[DM07] Masahiko Daimon and Akira Masumura. “Measurement of the refractive index of distilled water from the near-infrared region to the ultraviolet region”. In: *Applied Optics* 46.18 (2007), pp. 3811–3820. ISSN: 15394522. DOI: 10.1364/AO.46.003811.

[DR19] Mukulika Dinara and Chandra Sekhar Rout. *Two Dimensional Transition Metal Dichalcogenides*. Springer Singapore, 2019, pp. 29–68. ISBN: 9789811390456. DOI: 10.1007/978-981-13-9045-6. URL: http://dx.doi.org/10.1007/978-981-13-9045-6_2.

[DR55] G. C. Dacey and I. M. Ross. “The Field Effect Transistor”. In: *Bell System Technical Journal* 34.6 (Nov. 1955), pp. 1149–1189. DOI: 10.1002/j.1538-7305.1955.tb03794.x. URL: https://doi.org/10.1002/j.1538-7305.1955.tb03794.x.

[Dur+18] José Ramón Durán Retamal et al. “Charge carrier injection and transport engineering in two-dimensional transition metal dichalcogenides”. In: *Chemical Science* 9.40 (2018), pp. 7727–7745. ISSN: 20416539. DOI: 10.1039/c8sc02609b.

[Dus23] Saul Dushman. “Electron Emission from Metals as a Function of Temperature”. In: *Physical Review* 21.6 (June 1923), pp. 623–636. DOI: `10.1103/physrev.21.623`. URL: `https://doi.org/10.1103/physrev.21.623`.

[Dut+05] Gregory Dutton et al. “Exciton dynamics at molecule-metal interfaces: C60 Au(111)”. In: *Physical Review B - Condensed Matter and Materials Physics* 72.4 (2005), pp. 1–11. ISSN: 10980121. DOI: `10.1103/PhysRevB.72.045441`.

[EA21] Özüm Emre Aşırım. “Far-IR to deep-UV adaptive supercontinuum generation using semiconductor nano-antennas via carrier injection rate modulation”. In: *Applied Nanoscience* 12.1 (Nov. 2021), pp. 1–16. DOI: `10.1007/s13204-021-02147-1`. URL: `https://doi.org/10.1007/s13204-021-02147-1`.

[Evs22] Mykhaylo Evstigneev. “Generation–Recombination Processes”. In: *Introduction to Semiconductor Physics and Devices*. Springer International Publishing, 2022, pp. 171–196. DOI: `10.1007/978-3-031-08458-4_7`. URL: `https://doi.org/10.1007/978-3-031-08458-4_7`.

[Fan+15] Changming Fang et al. “The accurate calculation of the band gap of liquid water by means of GW corrections applied to plane-wave density functional theory molecular dynamics simulations”. In: *Physical Chemistry Chemical Physics* 17.1 (2015), pp. 365–375. ISSN: 14639076. DOI: `10.1039/c4cp04202f`.

[Fuj+16] Nobuyuki Fujimura et al. “Evaluation of valence band top and electron affinity of SiO2 and Si-based semiconductors using X-ray photoelectron spectroscopy”. In: *Japanese Journal of Applied Physics* 55.8S2 (2016), pp. 4–9. ISSN: 13474065. DOI: `10.7567/JJAP.55.08PC06`.

[GP00] Guiseppe Grosse and Giuseppe Pastori Parravicini. “Optical and transport properties in metals”. In: *Solid State Physics*. Elsevier, 2000, pp. 389–424. DOI: `10.1016/b978-012304460-0/50011-6`. URL: `https://doi.org/10.1016/b978-012304460-0/50011-6`.

[GP14] Giuseppe Grosso and Giuseppe Pastori Parravicini. “Transport in Intrinsic and Homogeneously Doped Semiconductors”. In: *Solid State Physics*. Elsevier, 2014, pp. 577–608. DOI: 10.1016/b978-0-12-385030-0.00013-x. URL: https://doi.org/10.1016/b978-0-12-385030-0.00013-x.

[Gra05] Jeffery L. Gray. “The Physics of the Solar Cell”. In: *Handbook of Photovoltaic Science and Engineering*. John Wiley & Sons, Ltd, Jan. 2005, pp. 61–112. DOI: 10.1002/0470014008.ch3. URL: https://doi.org/10.1002/0470014008.ch3.

[Hin+13] N. Hinkley et al. “An Atomic Clock with 10 sup–18/sup Instability”. In: *Science* 341.6151 (Sept. 2013), pp. 1215–1218. DOI: 10.1126/science.1240420. URL: https://doi.org/10.1126/science.1240420.

[JG97] Tae In Jeon and D. Grischkowsky. “Nature of conduction in doped silicon”. In: *Physical Review Letters* 78.6 (1997), pp. 1106–1109. ISSN: 10797114. DOI: 10.1103/PhysRevLett.78.1106.

[Kat+19] Takuya Kato et al. “Record Efficiency for Thin-Film Polycrystalline Solar Cells Up to 22.9% Achieved by Cs-Treated Cu(In,Ga)(Se,S)2”. In: *IEEE Journal of Photovoltaics* 9.1 (2019), pp. 325–330. ISSN: 21563381. DOI: 10.1109/JPHOTOV.2018.2882206.

[Kho14] Daniel I. Khomskii. *Transition Metal Compounds*. Cambridge University Press, Oct. 2014. DOI: 10.1017/cbo9781139096782. URL: https://doi.org/10.1017/cbo9781139096782.

[KI21] A. Kudlis and I. Iorsh. “Modeling excitonic Mott transitions in two-dimensional semiconductors”. In: *Physical Review B* 103.11 (2021), pp. 1–28. ISSN: 24699969. DOI: 10.1103/PhysRevB.103.115307. arXiv: 2011.12741.

[KK06] M. Kira and S. W. Koch. “Many-body correlations and excitonic effects in semiconductor spectroscopy”. In: *Progress in Quantum Electronics* 30.5 (2006), pp. 155–296. ISSN: 00796727. DOI: 10.1016/j.pquantelec.2006.12.002.

[KN21] Adam M. Kaufman and Kang-Kuen Ni. “Quantum science with optical tweezer arrays of ultracold atoms and molecules”. In: *Nature Physics* 17.12 (Nov. 2021), pp. 1324–1333. DOI: `10.1038/s41567-021-01357-2`. URL: `https://doi.org/10.1038/s41567-021-01357-2`.

[LCF87] Jeffrey R. Lince, David J. Carré, and Paul D. Fleischauer. “Schottky-barrier formation on a covalent semiconductor without Fermi-level pinning: The metal-MoS2(0001) interface”. In: *Physical Review B* 36.3 (1987), pp. 1647–1656. ISSN: 01631829. DOI: `10.1103/PhysRevB.36.1647`.

[Liu+02] W. Liu et al. “Intensity clamping of a femtosecond laser pulse in condensed matter”. In: *Optics Communications* 202.1-3 (Feb. 2002), pp. 189–197. DOI: `10.1016/s0030-4018(01)01698-4`. URL: `https://doi.org/10.1016/s0030-4018(01)01698-4`.

[Liu+16] Fengjiang Liu et al. “Laser filamentation induced bubbles and their motion in water”. In: *Optics Express* 24.12 (June 2016), p. 13258. DOI: `10.1364/oe.24.013258`. URL: `https://doi.org/10.1364/oe.24.013258`.

[Mak+10] Kin Fai Mak et al. “Atomically thin MoS2: A new direct-gap semiconductor”. In: *Physical Review Letters* 105.13 (2010), pp. 2–5. ISSN: 00319007. DOI: `10.1103/PhysRevLett.105.136805`. arXiv: `1004.0546`.

[MC16] C Manzoni and G Cerullo. “Design criteria for ultrafast optical parametric amplifiers”. In: *Journal of Optics* 18.10 (Aug. 2016), p. 103501. DOI: `10.1088/2040-8978/18/10/103501`. URL: `https://doi.org/10.1088/2040-8978/18/10/103501`.

[Met+03] W. K. Metzger et al. “Time-resolved photoluminescence studies of CdTe solar cells”. In: *Journal of Applied Physics* 94.5 (2003), pp. 3549–3555. ISSN: 00218979. DOI: `10.1063/1.1597974`.

[Mid+02] Katsumi Midorikawa et al. “Polarization properties of ultrafast white-light continuum generated in condensed media”. In: *Applied Physics Letters* 80.6 (Feb. 2002), pp. 923–925. DOI: `10.1063/1.1448146`. URL: `https://doi.org/10.1063/1.1448146`.

[Min+01] Takashi Minemoto et al. “Theoretical analysis of the effect of conduction band offset of window/CIS layers on performance of CIS solar cells using device simulation”. In: *Solar Energy Materials and Solar Cells* 67.1-4 (2001), pp. 83–88. ISSN: 09270248. DOI: `10.1016/S0927-0248(00)00266-X`.

[Mon90] W Monch. “On the physics of metal-semiconductor interfaces”. In: *Reports on Progress in Physics* 53.3 (Mar. 1990), pp. 221–278. DOI: `10.1088/0034-4885/53/3/001`. URL: `https://doi.org/10.1088/0034-4885/53/3/001`.

[MOT68] N. F. MOTT. “Metal-Insulator Transition”. In: *Reviews of Modern Physics* 40.4 (Oct. 1968), pp. 677–683. DOI: `10.1103/revmodphys.40.677`. URL: `https://doi.org/10.1103/revmodphys.40.677`.

[NBV95] Alex Niemegeers, Marc Burgelman, and Alexis De Vos. “On the CdS/CuInSe2 conduction band discontinuity”. In: *Applied Physics Letters* 67.6 (Aug. 1995), pp. 843–845. DOI: `10.1063/1.115523`. URL: `https://doi.org/10.1063/1.115523`.

[NC12] Michael A. Nielsen and Isaac L. Chuang. *Quantum Computation and Quantum Information*. Cambridge University Press, June 2012. DOI: `10.1017/cbo9780511976667`. URL: `https://doi.org/10.1017/cbo9780511976667`.

[NK99] T. Nakada and A. Kunioka. “Direct evidence of Cd diffusion into Cu(In,Ga)Se2 thin films during chemical-bath deposition process of CdS films”. In: *Applied Physics Letters* 74.17 (1999), pp. 2444–2446. ISSN: 00036951. DOI: `10.1063/1.123875`.

[NWH96] Ajay Nahata, Aniruddha S. Weling, and Tony F. Heinz. "A wideband coherent terahertz spectroscopy system using optical rectification and electro-optic sampling". In: *Applied Physics Letters* 69.16 (1996), pp. 2321–2323. ISSN: 00036951. DOI: 10.1063/1.117511.

[OA17] Sampson Oladapo Oyedele and Boko Aka. "Numerical Simulation of Varied Buffer Layer of Solar Cells Based on Cigs". In: *Modeling and Numerical Simulation of Material Science* 07.03 (2017), pp. 33–45. ISSN: 2164-5345. DOI: 10.4236/mnsms.2017.73003.

[Par+18] Soohyung Park et al. "Direct determination of monolayer MoSsub2/suband WSesub2/subexciton binding energies on insulating and metallic substrates". In: *2D Materials* 5.2 (Jan. 2018), p. 025003. DOI: 10.1088/2053-1583/aaa4ca. URL: https://doi.org/10.1088/2053-1583/aaa4ca.

[PB+06] C. Platzer-Björkman et al. "Zn(O, S) buffer layers by atomic layer deposition in Cu(In, Ga)Se 2 based thin film solar cells: Band alignment and sulfur gradient". In: *Journal of Applied Physics* 100.4 (2006). ISSN: 00218979. DOI: 10.1063/1.2222067.

[Pla+01] Paul C. M. Planken et al. "Measurement and calculation of the orientation dependence of terahertz pulse detection in ZnTe". In: *Journal of the Optical Society of America B* 18.3 (Mar. 2001), p. 313. DOI: 10.1364/josab.18.000313. URL: https://doi.org/10.1364/josab.18.000313.

[Pod+21] Darjan Podbevšek et al. "Experimental evaluation of methodologies for single transient cavitation bubble generation in liquids". In: *Experiments in Fluids* 62.8 (July 2021). DOI: 10.1007/s00348-021-03260-1. URL: https://doi.org/10.1007/s00348-021-03260-1.

[Pol+09] Pavel Polynkin et al. "Curved Plasma Channel Generation Using Ultraintense Airy Beams". In: *Science* 324.5924 (Apr. 2009), pp. 229–232. DOI: 10.1126/science.1169544. URL: https://doi.org/10.1126/science.1169544.

[Pol+10] D. Polli et al. “Effective temporal resolution in pump-probe spectroscopy with strongly chirped pulses”. In: *Physical Review A - Atomic, Molecular, and Optical Physics* 82.5 (2010), pp. 1–8. ISSN: 10502947. DOI: `10.1103/PhysRevA.82.053809`.

[PS09] K. E. Peiponen and J. J. Saarinen. “Generalized Kramers-Kronig relations in nonlinear optical- and THz-spectroscopy”. In: *Reports on Progress in Physics* 72.5 (2009). ISSN: 00344885. DOI: `10.1088/0034-4885/72/5/056401`.

[Pup17] Michele Puppin. “Time- and angle-resolved photoemission spectroscopy on bidimensional semiconductors with a 500 kHz extreme ultraviolet light source”. PhD thesis. Berlin, GE: Freie Universitat Berlin, 2017.

[RA+23] Kilian Richard Keller Ricardo Rojas-Aedo et al. “High stability white light generation in water at multi-kilohertz repetition rates”. In: *Optics Express* 31.23 (Oct. 2023), p. 38400. DOI: `10.1364/oe.503172`. URL: `https://doi.org/10.1364/oe.503172`.

[Ram+22] Omar Ramírez et al. “How much gallium do we need for a p-type Cu(In,Ga)Se2?” In: *APL Materials* 10.6 (2022). ISSN: 2166532X. DOI: `10.1063/5.0091676`. URL: `https://doi.org/10.1063/5.0091676`.

[Ro/+97] Cecilie Ro/nne et al. “Investigation of the temperature dependence of dielectric relaxation in liquid water by THz reflection spectroscopy and molecular dynamics simulation”. In: *The Journal of Chemical Physics* 107.14 (Oct. 1997), pp. 5319–5331. DOI: `10.1063/1.474242`. URL: `https://doi.org/10.1063/1.474242`.

[Rob+16] C. Robert et al. “Exciton radiative lifetime in transition metal dichalcogenide monolayers”. In: *Physical Review B* 93.20 (2016), pp. 1–10. ISSN: 24699969. DOI: `10.1103/PhysRevB.93.205423`. arXiv: `1603.00277`.

[Roc08] Angus Rockett. “Semiconductor Alloys”. In: *The Materials Science of Semiconductors*. Springer US, 2008, pp. 237–287. DOI: 10.1007/978-0-387-68650-9_6. URL: https://doi.org/10.1007/978-0-387-68650-9_6.

[Roc+94] A. Rockett et al. “Structure and chemistry of CuInSe2 for solar cell technology: current understanding and recommendations”. In: *Thin Solid Films* 237.1-2 (Jan. 1994), pp. 1–11. DOI: 10.1016/0040-6090(94)90228-3. URL: https://doi.org/10.1016/0040-6090(94)90228-3.

[RRA+22] Kilian R. Keller Ricardo Rojas-Aedo et al. “Ultrafast Thermionic Electron Injection Effects on Exciton Formation Dynamics at a van der Waals Semiconductor/Metal Interface”. In: *ACS Photonics* 9.8 (July 2022), pp. 2683–2690. DOI: 10.1021/acsphotonics.2c00394. URL: https://doi.org/10.1021/acsphotonics.2c00394.

[Sar20] Ibrahim Sarpkaya. *Optical properties of semiconducting transition metal dichalcogenide materials*. INC, 2020, pp. 57–75. ISBN: 9780128184752. DOI: 10.1016/B978-0-12-818475-2.00004-0. URL: http://dx.doi.org/10.1016/B978-0-12-818475-2.00004-0.

[Sch+16] John R. Schaibley et al. “Valleytronics in 2D materials”. In: *Nature Reviews Materials* 1.11 (2016), pp. 1–15. ISSN: 20588437. DOI: 10.1038/natrevmats.2016.55. URL: http://dx.doi.org/10.1038/natrevmats.2016.55.

[SE84] Boris I. Shklovskii and Alex L. Efros. *Electronic Properties of Doped Semiconductors*. Springer Berlin Heidelberg, 1984. DOI: 10.1007/978-3-662-02403-4. URL: https://doi.org/10.1007/978-3-662-02403-4.

[Sie04] Susanne Siebentritt. “Alternative buffers for chalcopyrite solar cells”. In: *Solar Energy* 77.6 (2004), pp. 767–775. ISSN: 0038092X. DOI: 10.1016/j.solener.2004.06.018.

[SK19] Aidan Schiff-Kearn. “Experimental and Numerical Investigations into Terahertz Time-Domain Spectroscopy”. Master thesis. Ottawa, CA: University of Ottawa, 2019.

[SN10] Zhenming Song and Takashi Nakajima. “Formation of filament and plasma channel by the Bessel incident beam in Ar gas: role of the outer part of the beam”. In: *Optics Express* 18.12 (2010), p. 12923. ISSN: 10944087. DOI: `10.1364/oe.18.012923`.

[SR52] W. Shockley and W. T. Read. “Statistics of the recombinations of holes and electrons”. In: *Physical Review* 87.5 (1952), pp. 835–842. ISSN: 0031899X. DOI: `10.1103/PhysRev.87.835`.

[Tam+18] Gintaras Tamošauskas et al. “Transmittance and phase matching of BBO crystal in the 35 μm range and its application for the characterization of mid-infrared laser pulses”. In: *Optical Materials Express* 8.6 (2018), p. 1410. ISSN: 21593930. DOI: `10.1364/ome.8.001410`.

[TFB03] Pancho Tzankov, Torsten Fiebig, and Ivan Buchvarov. “Tunable femtosecond pulses in the near-ultraviolet from ultrabroadband parametric amplification”. In: *Applied Physics Letters* 82.4 (Jan. 2003), pp. 517–519. DOI: `10.1063/1.1539555`. URL: `https://doi.org/10.1063/1.1539555`.

[TKD21] Sonam Tripathi, Brijesh Kumar, and D. K. Dwivedi. “Numerical simulation of non-toxic In2S3/SnS2 buffer layer to enhance CZTS solar cells efficiency by optimizing device parameters”. In: *Optik* 227 (2021), p. 166087. ISSN: 00304026. DOI: `10.1016/j.ijleo.2020.166087`. URL: `https://doi.org/10.1016/j.ijleo.2020.166087`.

[TLR12] Wolfgang Tress, Karl Leo, and Moritz Riede. “Optimum mobility, contact properties, and open-circuit voltage of organic solar cells: A drift-diffusion simulation study”. In: *Physical Review B - Condensed Matter and Materials Physics* 85.15 (2012), pp. 1–11. ISSN: 10980121. DOI: `10.1103/PhysRevB.85.155201`.

[Tom+20] John A. Tomko et al. “Long-lived modulation of plasmonic absorption by ballistic thermal injection”. In: *Nature Nanotechnology* 16.1 (Nov. 2020), pp. 47–51. DOI: `10.1038/s41565-020-00794-z`. URL: `https://doi.org/10.1038/s41565-020-00794-z`.

[Van+09] J. J.M. Van Der Holst et al. “Electron-hole recombination in disordered organic semiconductors: Validity of the Langevin formula”. In: *Physical Review B - Condensed Matter and Materials Physics* 80.23 (2009), pp. 1–8. ISSN: 10980121. DOI: 10.1103/PhysRevB.80.235202.

[Vid+13] S. Vidal et al. “Optimized terahertz generation in ZnTe crystals”. In: *International Conference on Infrared, Millimeter, and Terahertz Waves, IRMMW-THz* 31.1 (2013), pp. 149–153. ISSN: 21622027. DOI: 10.1109/IRMMW-THz.2013.6665926.

[VMH14] Carlo Vicario, Balazs Monoszlai, and Christoph P. Hauri. “mml:math xmlns:mml="http://www.w3.org/1998/Math/MathML" display="inline"mml:mrowm
mathvariant="normal"m/mml:mi/mml:mrow/mml:mathSingle-Cycle Terahertz Fields from a Laser-Driven Large-Size Partitioned Organic Crystal”. In: *Physical Review Letters* 112.21 (May 2014). DOI: 10.1103/physrevlett.112.213901. URL: https://doi.org/10.1103/physrevlett.112.213901.

[WCW15] Uli Wurfel, Andres Cuevas, and Peter Wurfel. “Charge carrier separation in solar cells”. In: *IEEE Journal of Photovoltaics* 5.1 (2015), pp. 461–469. ISSN: 21563381. DOI: 10.1109/JPHOTOV.2014.2363550.

[Wei+16] Chengrong Wei et al. “Bound exciton and free exciton states in GaSe thin slab”. In: *Scientific Reports* 6.September (2016), pp. 1–6. ISSN: 20452322. DOI: 10.1038/srep33890. URL: http://dx.doi.org/10.1038/srep33890.

[Xia+21] Chuanxiao Xiao et al. “Long-Term Degradation of Passivated Emitter and Rear Contact Silicon Solar Cell under Light and Heat”. In: *Solar RRL* 6.1 (Nov. 2021), p. 2100727. DOI: 10.1002/solr.202100727. URL: https://doi.org/10.1002/solr.202100727.

[YM07] Jianjun Yang and Guoguang Mu. “Multi-dimensional observation of white-light filaments generated by femtosecond laser pulses in condensed medium”. In: *Optics Express* 15.8 (2007), p. 4943. ISSN: 10944087. DOI: 10.1364/oe.15.004943.

[Yı22] Hasan Yıldırım. “Excitons in nonpolar ZnO/BeZnO quantum wells: Their binding energy and its dependence on the dimensions of the structures”. In: *Physica B: Condensed Matter* 639.April (2022), p. 413974. ISSN: 09214526. DOI: `10.1016/j.physb.2022.413974`. URL: `https://doi.org/10.1016/j.physb.2022.413974`.

[Zha+20] Huiqin Zhang et al. “Hybrid exciton-plasmon-polaritons in van der Waals semiconductor gratings”. In: *Nature Communications* 11.1 (2020), pp. 1–9. ISSN: 20411723. DOI: `10.1038/s41467-020-17313-2`. arXiv: `1912.13442`. URL: `http://dx.doi.org/10.1038/s41467-020-17313-2`.